Structural Sizing Method for Propulsive Empennage System

Weight Estimation of Ducted Propeller Systems that Provide Longitudinal and Lateral Stability

Martina N. Stavreva

Technische Universiteit Delft

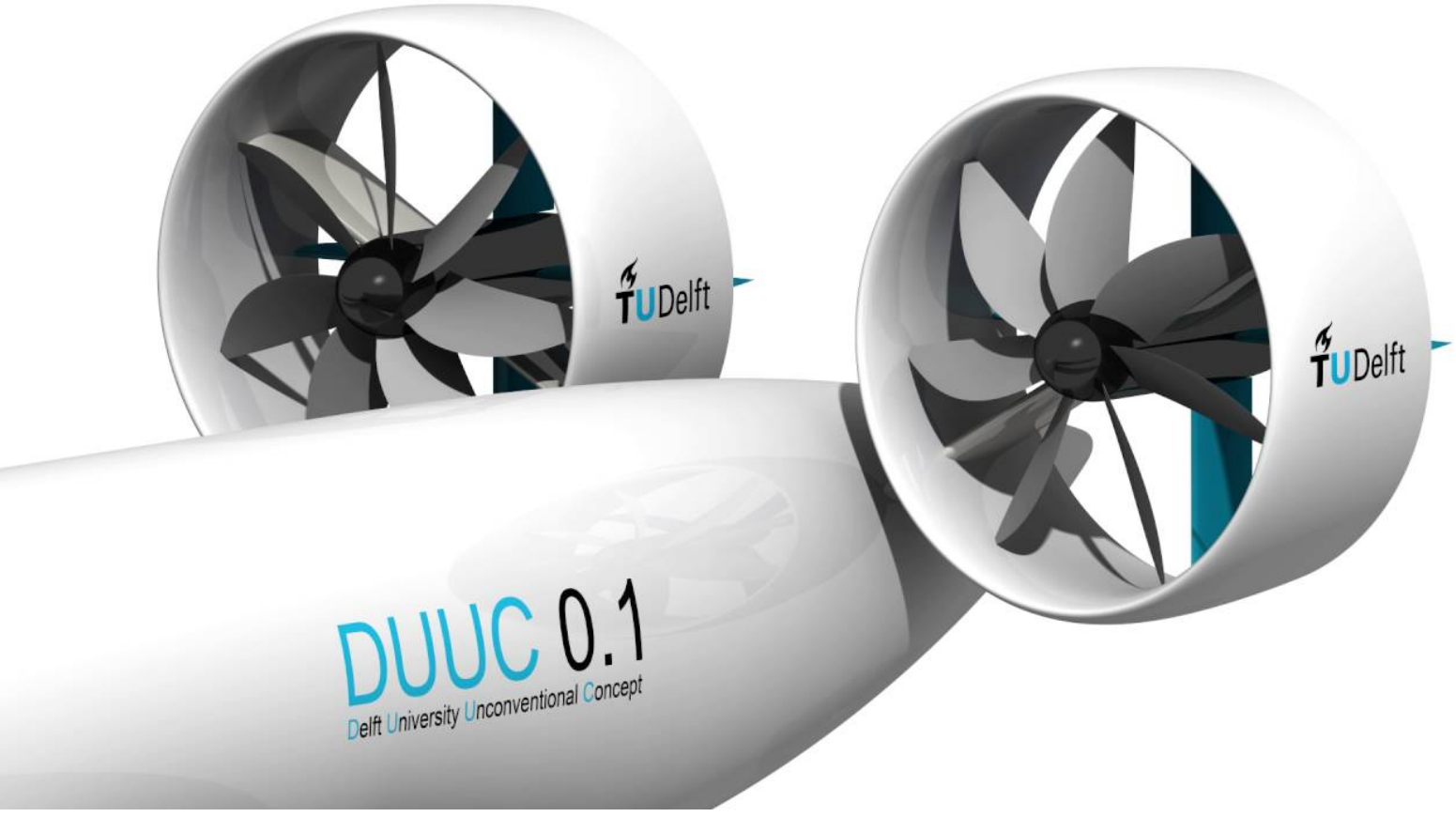

TU Delft Delft University of Technology

Challenge the future

Structural Sizing Method for Propulsive Empennage System

Weight Estimation of Ducted Propeller Systems that Provide Longitudinal and Lateral Stability

by

Martina N. Stavreva

In partial fulfilment of the requirements for the degree of

Master of Science

in Aerospace Engineering

at the Delft University of Technology,

to be defended publicly on Monday August 27, 2020 at 09:00 AM.

Supervisor:	Dr. ir. M.F.M. Hoogreef	
Thesis committee:	Prof. dr. ir. L.L.M. Veldhuis,	TU Delft
	Dr. ir. M.F.M. Hoogreef,	TU Delft
	Ir. J. Sinke,	TU Delft

An electronic version of this thesis is available at http://repository.tudelft.nl/.

TU Delft Delft University of Technology

PREFACE

I would first like to thank my supervisor Dr.ir.M.F.M.Hoogreef as well as Ir.Reno Elmendorp and Dr.ir.Tomas Sinnige for always being available for discussions and giving me valuable guidance during this research. Furthermore, I would like to express my deepest gratitude to Professor dr. ir. L.L.M. Velhuis and Ir.J.Sinke for reading and grading this research. The latter I would also like to thank for the amazing opportunity he and the rest of the AML coordinators gave me by making me the team lead of Team 3, this was one remarkable experience!

I have spent enough time in Delft to be able to fill a whole page with thanking people whom I have met and influenced me in one way or another to become the person who I am today. Some honourable mentions are: my friends with whom we battled the bachelor Flavie, Essi, Alex, Val, Momchil, Stani, Evgeni and the rest of the Bulgarian gang, Gergely, Abhranil, Stevan and really many more; Christel who taught me my first Dutch words back in the days of our freshmen weekend and with whom we then rocked the masters and taught the PhDs one or two things; Zoe, Marta, Hannah for the nice workouts, cosy dinners and always offering a friendly shoulder; to all the people from the FPP master rooms, it was a great pleasure to work with you (while we were allowed to be there that is) and so many more.

To my dear flatmates, I thank you for being so amazingly supportive and understanding. I truly love you and will always keep those six years living with you as a fond memory!

In addition to this, I would like to thank the VSV and AWEP for giving me a wide range of extra-curricular activities to develop in other than technical aspects and to meet great people and companies!

I would also like to thank my colleagues and friends I met during my internships at both Lufthansa Technik and Airbus. Special thanks to my supervisor James Hardy for giving me so much knowledge, support and development opportunities over the year in Filton as well as for all the banter and showing me the true beauty and fun of full-time fire fighting!

But most of all, I would like to thank my parents for always supporting me and believing in me! It was not easy for either you letting go of your only child nor for me to leave everything I knew, but you always got my back! Also, a big "Thank you!" to my Dutch parents who were always here to support me, give me great advice and remind me that I can! I love you all!

"The most effective way to do it is to do it!"
Amelia Earhart

M.N.Stavreva
Delft, August 2020

P.S. A big "thank you" to Corona pandemic for making my life "so much better" and "not" destroying my dreams.

SUMMARY

Flight Performance and Propulsion department of Aerospace Engineering, Delft University of Technology has proposed an effective and sustainable solution to the main challenges aviation is currently facing, namely the raising concerns regarding the environmental and health impact of the industry. Delft University Unconventional Concept (DUUC) has a conventional fuselage coupled with clean wing that is expected to facilitate laminar flow. Furthermore, two ducted propellers are positioned aft on the tail cone installed via pylons. The ducts are designed such that they perform multiple functions: they provide sufficient longitudinal and directional stability, resulting in no tail-configuration and possible weight reduction, improve propulsive performance by increasing static thrust, assure higher safety in blade-loss and reduce cabin and community noise.

Studies on the DUUC have been carried out in the Aerospace Engineering Faculty at TU Delft. One of the main challenges has proven to be the aft centre of gravity, caused by placing the heavy propulsion group on the tail cone, that shifts forward in flight, naturally resulting in higher trim drag. Together with expected reinforcements of the fuselage, due to the presence of heavy empennage, those result in higher operational empty weight and shorter range with the same payload when compared to conventional configuration. It should be noted that those studies size the ducts and pylons using empirical weight estimation relations that are derived for components with similar but not exactly the same functions. Being main contributors to the concept's weight and thus performance, a more detail physics-based and design-sensitive weight estimation method for the ducts and the pylons, which allows for more accurate performance prediction, is required.

From here the main research question follows and it is defined as: *"How to estimate the weight of a ducted propeller propulsive empennage at conceptual design phase?"*. The research goal defines the way to answer this question: *"Define and implement a physics-based design sensitive structural sizing method to determine Delft University Unconventional Concept's propulsive empennage weight by identifying the critical sizing load cases and relevant analysis methods as well as ensuring to be capable of applying the correct aerodynamic and structural loads and showing flexibility for possible design changes."*

Class 2.5 weight estimation method that implements a simplified Finite Element Method (FEM) was used for the analysis when considering static loading. Three critical design conditions were identified for the duct: take-off, when the engine is at full power; cruise, which is typical nacelle design condition; and dive, when highest speed and therefore dynamic pressure is experienced by the structure and uncompromised stability forces are needed. The structure is represented by a number of beams, with their cross sectional areas and moments of inertia. The shear flow and normal stresses on the cross-section was determined, based on which the skin thicknesses were obtained. If CFRP is used a duct mass reduction of more than 70% is observed. Last but not least, a protective kevlar layer is designed such that any pieces of blade in case of failure is contained.

The critical static cases identified for pylon sizing are take-off with full engine thrust, dive, when highest dynamic pressure is present and crash landing to ensure ground clearance. The method identified that, if the material is kept to aluminium, the pylon is heavier, which is contributed to the high loading coming from the engine thrust. A reduction to less than half the original weight can be achieved if CFRP is chosen.

Already in the initial literature review it is identified that the critical loading on engine mount systems is blade loss conditions, when the imbalance of the engine propeller system causes severe vibrations on the pylon. As this analysis is seen too detailed for the conceptual design phase, the proposed method does not implement a dynamic FEM model. However, a vibrations analysis is carried out and it was concluded that, when more engine operations information is available, more detailed dynamic analysis needs to be carried out.

This method was also integrated in the overall analysis, which allowed to observe if the more accurate weight estimation has beneficial effect on the performance of the concept. As expected, a reduction in operational empty weight, which naturally lead to lower maximum take-off weight, was achieved. Highest improvements were seen with a CFRP empennage reducing the mass by 1 tonne. Unfortunately, no major mission performance improvements were observed. If the maximum take-off weights are compared, better wing position and shorter centre of gravity excursion are feasible. In case the MTOM is kept constant, the weight freed by the lower structural weight can be used for more fuel and therefore, with the same engine characteristics, higher range capabilities with the same payload or higher payload can be carried over the same distance.

CONTENTS

List of Figures

LIST OF TABLES

List of Symbols & Abbreviations

List of Symbols

Symbol	Description	*SI* Unit
A	Area	$[m^2]$
AF	Activity Factor	$[-]$
AR	Aspect Ratio	$[-]$
b	Span	$[m]$
B_n	Area of n^{th} Boom	$[m^2]$
c	Airfoil Chord	$[m]$
c	Damping	$[\sqrt{N}]$
C	Damping Constant	$[-]$
c_d	Airfoil Drag Coefficient	$[-]$
C_D	Wing Drag Coefficient	$[-]$
c_{d_i}	Airfoil Induced Drag Coefficient	$[-]$
C_{D_i}	Wing Induced Drag Coefficient	$[-]$
C_f	Skin Friction Coefficient	$[-]$
c_l	Airfoil Lift Coefficient	$[-]$
C_L	Wing Lift Coefficient	$[-]$
C_{L_α}	Wing Lift Curve Slope	$[-]$
c_{c_α}	Airfoil Lift Curve Slope	$[-]$
C_P	Power Coefficient	$[-]$
C_T	Thrust Coefficient	$[-]$
D	Diameter	$[m]$
D	Drag Force	$[N]$
E	Young's Modulus	$[Pa]$
E	Energy	$[J]$
e	Oswald Factor	$[-]$
F	Force	$[N]$
FW	Fuel Weight	$[N]$
G	Shear Modulus	$[Pa]$
h	Height/Depth	$[m]$
I	Moment of Inertia	$[m^4]$
J	Advance Ratio	$[-]$
k	Spring Stiffness	$[N/m]$
K	Stiffness Constant	$[-]$
K_h	linear Stiffness	$[N/m]$
K_θ	Rotational Stiffness	$[N/rad]$
L	Lift Force	$[N]$
l	Length/Distance	$[m]$
L/D	Aerodynamic Efficiency	$[-]$
M	Mach Number	$[-]$
M	Moment	$[Nm]$
m	Mass	$[kg]$
$\dot{m}$	Mass Flow	$[kg/s]$
MFM	Minimum Fuel Mass	$[kg]$
$MTOM$	Maximum Take-Off Mass	$[kg]$
$MTOW$	Maximum Take-Off Weight	$[N]$

Symbol	Description	*SI* Unit
n	Number of Revolutions	$[-]$
OEM	Operational Empty Mass	$[kg]$
P	Power	$[W]$
p	Distance to Shear Flow Axis	$[m]$
p	Pressure	$[Pa]$
PLW	Payload Weight	$[N]$
q	Dynamic Pressure	$[Pa]$
q_s	Shear Flow	$[N/m]$
r	Radius	$[m]$
R_e	Reynolds Number	$[-]$
s	Length	$[m]$
S	Area	$[m^2]$
S	Shear Force	$[N]$
S_θ	Rotational Moment of Inertia	$[rad^4]$
t	Thickness	$[m]$
T	Period	$[s]$
T	Thrust	$[N]$
T	Torque	$[Nm]$
T_c	Thrust Coefficient	$[-]$
t/c	Thickness Ratio	$[-]$
u	Velocity	$[m/s]$
V	Velocity	$[m/s]$
W	Weight	$[N]$
w	Width	$[m]$
x	Coordinate	$[m]$
y	Coordinate	$[m]$
z	Coordinate	$[m]$
α	Angle of Attack	$[^o]$
η	Efficiency	$[-]$
η_0	Vertical Distance from Shear Force x-Axis to Element Centroid	$[m]$
θ	Displacement Angle	$[rad]$
θ	Pitch Angle	$[^o]$
θ	Radial velocity	$[rad/s]$
λ	Sweep Angle	$[^o]$
ξ	Damping Ratio	$[-]$
ξ_0	Horizontal Distance from Shear Force y-Axis to Element Centroid	$[m]$
π	3.1416	$[-]$
ρ	Density	$[kg/m]$
σ	Normal Stress	$[Pa]$
τ	Shear Stress	$[Pa]$
ω	Angular Velocity	$[rad/s]$
ω_n	Natural Frequency	$[Hz]$

LIST OF ABBREVIATIONS & SUBSCRIPTS

Abbreviation or Subscript	Description	Abbreviation or Subscript	Description
AC	Aerodynamic Centre	L	Landing
Al	Aluminium	LG	Landing Gear
b	Basic	lim	Limit
bl	Blade	MAC	Mean Aerodynamic Centre
c	Centripetal	max	Maximum
C	Cruise	min	Minimum
cb	Centre Body	n	Nacelle
CFD	Computational Fluid Dynamics	NASA	The National Aeronautics and Space Administration
CG	Centre of Gravity		
con	Containment	O	Outer
$\bar{c}/4$	Quarter Chord	on	Power On
D	Dive	oop	Normal Operations
des	Design	PL	Pylon
DUUC	Delft University Unconventional Configuration	press	Pressure
		prop	Propeller
EA	Elastic Axis	ps	Power System
EAS	Equivalent airspeed	ref	Reference
EASA	European Union Aviation Safety Agency	RPM	Revolutions per Minute
		sc	Surface Control
en/eng	Engine	TAS	True airspeed
ext	External	TMP	Tail-Mounted Propellers
FAA	Federal Aviation Administration	TO	Take-Off
Fedrot	Fedrotschenko	tot	Total
FEM	Finite Elements Method	TU Delft	Technical University of Delft
FMDP	Fuselage-Mounted Ducted Propellers	ult	Ultimum
		VTP	Vertical Tail Plane
Goldsm	Goldsmith	w	Wing
HTP	Horizontal Tail Plane	wet	Wetted
int	Internal	WMP	Wing-Mounted Propellers
interf	Interference	y	Yield
Kev	Kevlar	0	Constant
kin	Kinetic	0	Sea Level
KPI	Key Performance Indicators	∞	Free Stream

1

INTRODUCTION

Concerns regarding aviation's impact on the environment and public health have been exponentially rising over the recent few years and it has become even more crucial that the industry proposes effective sustainable solutions with respect to fuel per passenger and noise per flight[1]. An innovative aircraft configuration with propulsive empennage that integrates two large ducted fans with the horizontal and vertical stabilisers was proposed by the Flight Performance and Propulsion department of TU Delft Aerospace Engineering faculty.

The configuration aims to decrease aircraft environmental footprint by improving propulsion performance, which results in lower fuel consumption, as well as decrease in noise emission. Furthermore, weight reduction compared to similar configurations with tail-mounted propellers achieved by removing the horizontal and vertical stabilising surfaces, as they become redundant in the ring-wings' presence, is expected[2]. More information on the performance and challenges of the concept are discussed in Section 1.1. The research objective will then be presented in Section 1.2 with this study's scope following in Section 1.3. Lastly, the outline of this thesis is given in Section 1.4.

1.1. DELFT UNIVERSITY UNCONVENTIONAL CONCEPT

In order to achieve supreme wing aerodynamic wing performance, the DUUC features clean wing that promotes laminar flow, which is combined with a conventional fuselage. Two pylons attach the unconventional empennage furthest aft on the aicraft's tail-cone. Figure 1.1 presents the configuration's subscale prototype. Figure 1.2 then offers a closed look of the ducted propellers. The control surfaces are also visible as blue surfaces positioned at the ducts' aft edges.

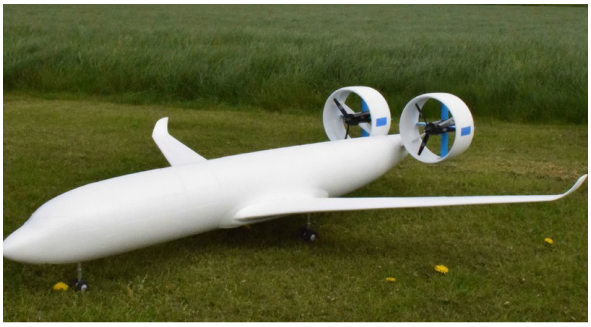

Figure 1.1: Delft University Unconventional Configuration[3].

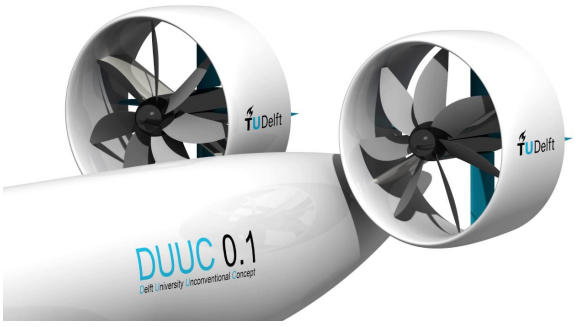

Figure 1.2: Duct design of the DUUC[4].

The empennage's position is firstly dictated by the requirement that the ducts provide sufficient horizontal and vertical stability, which is proportional to the distance with respect to aircraft's centre of gravity. At the same time, the heavy propulsion system's position affects the CG drastically and thus leads to lower stability efficiency of the ducts. Furthermore, the feasible wing installation locations are very limited and in order to decrease the trim drag penalty, most forward location is chosen.

Those choices naturally effect the configuration's performance, which is discussed by Vos and Hoogreef[2]. When compared to a conventional layout with engines mounted on the wing or with tail-mounted propulsion system, the DUUC has been observed to underperform when the maximum take-off mass, operational empty mass and mission fuel are considered. Even though in design conditions the DUUC seemed to perform almost identically to the other two concepts, it shows lowest off-design range capabilities.

The propulsive empennage size is identified as the main contributor for this lower performance. It should be, however, mentioned that previous research estimates the ducts' and pylons' weight using empirically derived expressions that have been verified for structures with similar functions, but due to the lack of experience, not identical. More specifically, the pylon is sized using Torenbeek's horizontal tail mass estimation that depends on pylon's area, the dive speed and a number of factors. The duct is estimated using Raymer's nacelle sizing that depends on amount of engines and their weight, the nacelle wetted area and again a set of factors that have been derived statistically. Therefore, it has been concluded that in order to represent and evaluate the concept as well as to compare it with other configurations, a more accurate weight estimation is required, which is also the focus of this research.

1.2. RESEARCH OBJECTIVE

It has been thus concluded that in order to represent and evaluate the concept as well as to compare it with other configurations, a more accurate weight estimation is required, which is also the focus of this research.

The main Research Question is defined as follows:

> *"How to estimate the weight of a ducted propeller propulsive empennage, such as the one of the Delft University Unconventional Concept's, at conceptual design phase?"*

There exist number of possible ways to answer the main research question. Thus, a more specific goal is defined by the Main Research Objective:

> *"Define and implement a physics-based design sensitive structural sizing method to determine Delft University Unconventional Concept's propulsive empennage weight by identifying the critical sizing load cases and relevant analysis methods as well as ensuring to be capable of applying the correct aerodynamic and structural loads and showing flexibility for possible design changes."*

The required intermediate steps are listed below in a set of sub-objectives:

- Determine the flight and loading conditions that size the ducts and the pylon of the propulsive empennage.
  - Define the most severe loading scenarios for the ducts and pylon respectively;
  - Define the corresponding loading distributions on the components.
- Define a complete physics-based and design sensitive structural analysis method to size the propulsive empennage system's components.
  - Define and implement structural analysis methods that are relevant to the duct's sizing;
  - Define and implement structural analysis methods that are relevant to the pylon's sizing;
  - Define an analytical model to represent loading of the ducts in blade-out failure and determine required thickness to contain the fractured element;
  - Carry out a vibration analysis to assess structural performance in blade-out case.

1.3. RESEARCH SCOPE

In order to define mission profile and top-level requirements as well as to have a basis for comparison and make conclusions on the performance of the unconventional concept, a reference already existing aircraft should be defined. Having been determined that the DUUC will be sized as a medium-range turboprop aircraft, two options are present: Fokker-50[5] and ATR72-600[6]. N.H.M. van den Dungen, who is one of the first master students to carry out a thorough investigation of the DUUC performance, chose ATR72-600 for a reference due to the wide range of information available. Thus, mission criteria and similar sizing rules have been used[7].

This research is focussing on developing a structural sizing method suitable for conceptual design. One of the main requirements is that the structure is capable of providing and sustaining sufficient aerodynamic loading to ensure aircraft's stability. In order to obtain a reasonable estimate, the method derived and verified by V. N. Harinarain[8] that estimates the lift and drag of the duct and pylon will be followed. This will be presented and discussed in Section 3.3.3. It should be noted that, even though more elaboration will be given, it is not of prime interest in the current study and the model has its limitations, which will also be presented for future reference.

Furthermore, the pylon length and incidence angle as well as duct aspect ratio and tip clearance to propeller blades are considered out of this research's scope. The reasoning behind is the fact that both of them affect propeller and control surface's performance severely. However, neither of them have been assessed and designed yet. Thus, the goal of this research is to define a sizing method that can accommodate for changes in those parameters and give valid weight estimation in different scenarios but not to determine those values. Note that additional damping systems required for the engine attachment are also not discussed in this research as this is considered part of detailed design phase.

The analysis should be integrated in the aicraft generation tool used for the DUUC's design definition, namely the Aircraft Initiator[9]. It is a Matlab-based script that generates feasible aircraft designs based on a set of inputs and requirements. Figure 1.3 gives a simplified schematic overview of the Initiator's organisation and it can be seen how sizing, aerodynamic and performance evaluation modules, which provide inputs to each other, are integrated[2].

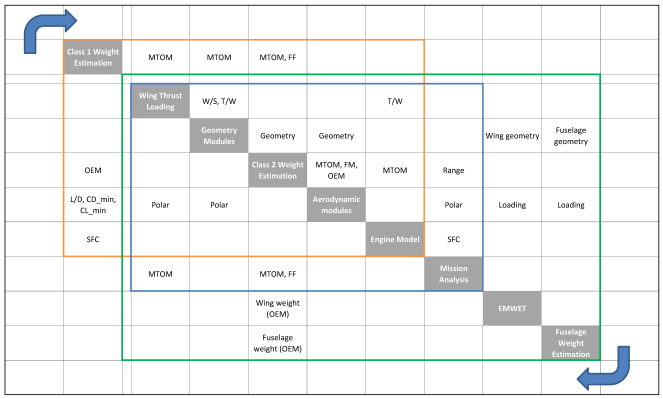

Figure 1.3: Aircraft Initiator N2 chart[2].

Three main loops, corresponding to higher level of detail and accuracy, are defined. The first one represents Class 1 Weight Estimation, which uses statistical data on currently existing conventional aircraft of the same range/weight group. Following is the more detailed Class 2 Weight Estimation that is component based and uses semi-empirical weight and geometrical estimation methods. With the structure being defined, the aerodynamic and performance analysis of the aircraft are carried out. Consequently, the wing and fuselage structures, as the ones that form the bigger part of the OEW and contribute severely to aircraft's performance, are then further analysed in the quasi-analytical Class 2.5 Weight Estimation. More information on the different sizing methods is given later in Section 2.3.

1.4. THESIS OUTLINE

The research will be presented in six chapters. Chapter 1 already introduced you to the concept and defined the reseach objective. Chapter 2 gives some background information on the technology of interest and relevant structural analysis methods. This is followed by Chapter 3, where the specific methodology to achieve the research goal and thus answer the research question is presented. The results and method analysis, consisting of duct model verification and design sensitivity study, are discussed in Chapter 4. Following is Chapter 5 which elaborates on how the proposed method and thus weight estimation effects the DUUC performance. Lastly, Chapter 6 gives the overall conclusions and recommendations for future work.

2

BACKGROUND

In order to understand the benefits offered by the selected technology as well as the challenges it poses, this chapter first gives some background information on ducted propellers in Section 2.1. This is followed by Section 2.2 providing an overview of the main concept's design choices, systems weight estimation and performance study. Section 2.3 then elaborates on typical conceptual design structural sizing methods as well as structural analysis methods used for designing a safe nacelle group capable of carrying the loads in the most critical engine condition, namely blade loss failure.

2.1. DUCTED PROPELLERS

The current section introduced the ducted propellers concept. Firstly the benefits and limitation of propellers are discussed in Section 2.1.1. Section 2.1.2 follows then with a discussion on ring wings, which are used for the ducts. Combining those to achieve superior propulsive and aerodynamic performance leads to ducted propeller discussed in Section 2.1.3.

2.1.1. PROPELLERS

As discussed by Q.Wald[10], first propeller theory development have taken place even before the famous Wright brothers' first heavier than air flight in December 1903, when research has been focused on marine propulsion. Later on, theoretical methods to estimate the efficiency have become available and have shown that propellers can deliver high propulsive efficiency at low Mach numbers. Through studies and model testing on high speed ($M = 0.65 - 0.85$) highly-loaded turboprops it has been concluded that fuel saving of 15%-30% compared to advanced turbofans, and 50%-60% compared to general turbofan technology is feasible, see Figure 2.1.

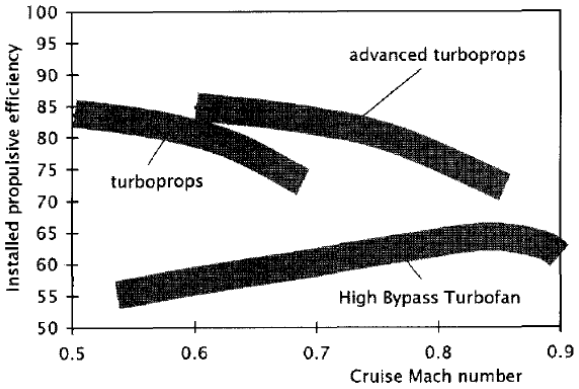

Figure 2.1: Comparison between installed propulsive efficiency for different Mach numbers of turbofans and turboprops[11].

This efficiency is achieved by the fact that a small change in velocity produces the required thrust. To define propeller's performance with respect to thrust and efficiency, two main theories are used: the actuator disk theory that gives an estimation of the momentum and kinetic energy change to the flow passing through the

propeller, and the blade element theory which defines the thrust created by the propeller. Discussing those in detail is out of scope of the current report, but two main parameters will be presented. The propeller advance ratio is defined by Equation 2.1. From the propeller efficiency definition given in Equation 2.2, it can be seen that propeller performance is strongly dependent on the advance ratio. This is also illustrated in Figure 2.2, which shows that maximum efficiency is reached at certain advance ratio, corresponding to a specific speed, after which it drops rapidly.

$$J = \frac{V}{nD_p} = \frac{V}{2nR_p} \tag{2.1}$$

$$\eta_p = \frac{P_{av}}{P_{br}} = \frac{TV}{P_{br}} = \frac{C_T}{C_P} J \tag{2.2}$$

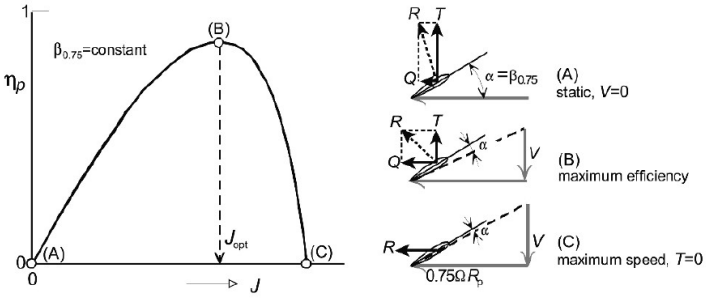

Figure 2.2: Propeller efficiency with respect to advance ratios and pitch angles[12].

However, low operational speeds as well as structural and acoustic challenges have made this concept unattractive for many year and only recently have engineers gone back to examining the advantages of the technology. This has been stimulated by the increased focus on efficiency as well as improved analysis tools and larger computational power, allowing for improvements in aerodynamic, structural and acoustic design[13].

2.1.2. RING WINGS

The benefits of non-planar wings have been studied and analytical models have already been defined in the 30s by L.Prandtl and O.G.Tietjens[14] who have looked into the concept of bi-planes and have proved that the total induced drag of biplane with the same span and total lift is always smaller than the monoplane one. However, it has been realised that a small increase of span to the monoplane leads to the same drag as the biplane one.

As discussed by Maqsood[15], one of the first analytical definitions of the ring wing's lift characteristics is given by Ribner in his work "The Ring Airfoil in Nonaxial Flow" who concludes that they have twice the lift-curve slope of the flat-plate wings with elliptical distribution. The higher wing efficiency can be explained by the larger volume of air captured to generate higher lift but at the absence of trailing edge vortices on the wing plane[16].

C.Cone[17] further elaborates on the topic by carrying out an investigation to define basic theoretical concepts and methods to estimate the induced lift and minimum induced drag of an arbitrary nonplanar lifting system. He has proven that the system's efficiency can be expressed using an effective aspect ratio and can be related to the one of a comparable planar wing. It has also been observed that significant reduction in induced drag can be achieved as nonplanar wings can have up to 50% higher effective aspect ratio. However, caution should be taken with respect to the higher wetted surface area and therefore possible structural issues and increased surface drag, which also have severe effect on the efficiency.

The higher wing efficiency can be explained by the larger volume of air captured to generate higher lift but at the absence of trailing edge vortices on the wing plane[16]. Trying to define a theoretical expression and prediction of the efficiency limit, A.Maqsood[15] has attempted to approximate experimental results with suction-based model, which have reached excellent agreement. It has been observed that indeed the lift coefficient increases, but at the cost of higher drag approximated by $C_D = C_{D_0} + KC_L^2$ where $K = a(AR)^b$ with $a = 0.15$ and $b = -1.237$. Even though increasing the aspect ratio in this relation reduces the drag, the contribution of the higher lift is significant and therefore the total drag is increased. Furthermore, stall is experienced at lower angles of attack compared to ring wings with lower aspect ratio.

Throughout the years a number of studies have attempted to define methods, which are able to predict the

aerodynamic performance of the annular wings. Naturally, they all have their limitations and/or show number of inconsistencies. The most accurate and complete one is observed to be proposed by J.Weissinger[18] who has improved the method of Ribner by applying a more complex lifting-surface approach. W.B. Morgan and E.B.Caster[19] later have revised this method and carried out wind tunnel tests with two ducts to validate the analytical method, used as input for a FORTRAN-based numerical model. With the higher computational power available at this time they manage to provide lift curve solutions for chord-diameter ratios (or $1/AR$) of 0.1 to 10.0. It is concluded that the duct's lift is accurately represented by the theory even in the presence of separation during the experiment, and C_{L_α} decreases with higher chord to diameter ratios. Naturally, the latter aligns with an increase of lift-curve slope with higher AR discussed before.

An experimental investigation of continuous and split ring wings with Eppler and NACA 0012 at low Reynolds numbers and with aspect ratios of 1 and 2 has been carried out by L.Traub[16]. It has been observed that the higher aspect ratio ring wing has higher lift coefficient but stalls at lower angles of attack compared to the ring wing with $AR = 1$. This can be explained by the fact that the latter causes a larger stream tube deflection, resulting in lower wing loading on the bottom part of the ring and therefore delayed stall. At the same time, the higher aspect ratio wing shows better aerodynamic performance with respect to lift induced drag that can be caused by the higher efficiency (also called Oswald) factor. Yet, neither of the wings reaches the theoretical $e = 2$ for the inviscid conditions, mainly affected by the higher sectional pressure drag.

L.Traub[16] also looks at the longitudinal stability of the ring wings and observes that both stall with a destabilising pitch-up tendency, which is attributed to stall occurring on the upper ring section prior the lower. The resulting high drag differential leads to nose-up break point. The different stall behaviour of the top and bottom parts can be explained by the uneven loading observed already before loss of lift. The study concludes that, even though the benefits in wing efficiency have been greatly reduced by the excessive increase in profile drag, their advantages can be utilised in carefully selected flight regimes.

Recent researches, such as the one carried out by A.Kanoria and M.Damodaran[20], have been mainly focused on the ring wings benefits with respect to unmanned aircraft vehicles, which have been finding various applications nowadays. The aim of the above mentioned has been to compare configurations with various airfoils as well as aspect ratios of $1/2, 1$ and 2. The ring wing with highest aspect ratio has shown highest lift curve slope, reached highest maximum lift coefficient and, even though at high angles of attack the generated drag is larger than the other two configurations, attains highest aerodynamic efficiency (L/D). Furthermore, the vorticity contours of the three configurations are illustrated in Figure 2.3, where it can be seen that the maximum magnitude is the same, but the affected area and separation region of $AR = 2$ is much smaller compared to $AR = 1/2$. Next to this, the observed lower pressure on the suction side of the ring wing with $AR = 1/2$ is seen as responsible for the lower lift coefficient discussed above.

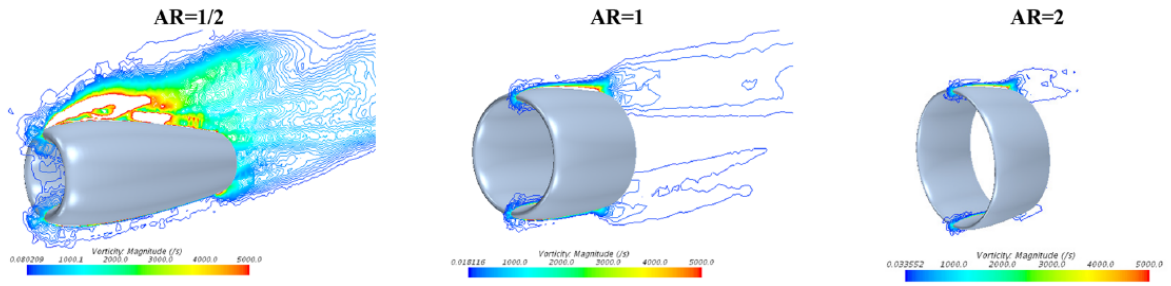

Figure 2.3: Vorticity contours at mid-plane of ring wings with Aspect Ratios of $1/2, 1$ and 2 from left to right[20].

M.Werle[21] aimed to provide a reliable method for predicting the aerodynamic performance of a ring-wing by carrying out a thorough review of the research carried out in the past. He has concluded that indeed Weissinger's[18] method is simple, reliable and accurate in expressing the aerodynamic forces and moments, while still the computational costs are kept in reasonable borders.

2.1.3. DUCTED PROPELLERS

The duct of the propeller in this discussion will have the sole purpose of increasing (static) system thrust, which is opposed to the one of a compressor that aims to increase the pressure over the propeller. Furthermore, a short discussion on the potential of decreasing propeller noise will also be presented.

Evidence of research on this concept date back to the early 30s when an Italian engineer has invented the Stipa-Caproni unconventional aircraft design that features a propeller ducted within a hollow fuselage, see Figures 2.4 and 2.5.

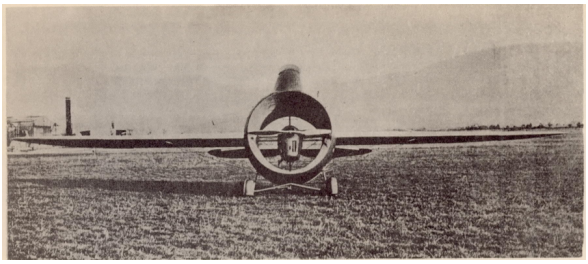

Figure 2.4: Stipa monoplane with venturi fuselage - front view[22].

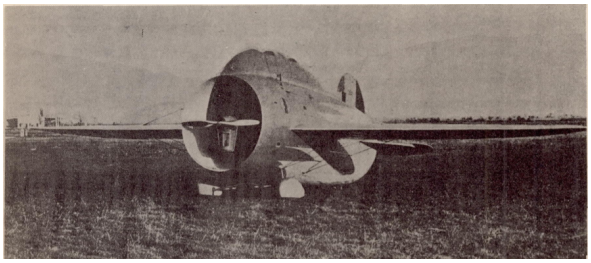

Figure 2.5: Stipa monoplane with venturi fuselage[22].

Stipa is also the first to carry out systematic wind tunnel tests with models having various tubular fuselage, which concludes that an aerodynamic efficiency of 3.4 is feasible with only one tube[22]. Other researches in those years by German and Russian scientists have also been identified. Motivation for further investigations has been the hover and possibly vertical take-off and landing improvements[23].

D.M. Black, H.S.Wainaiski and C.Rohrbach[24] give a clear explanation on the principles through which the ducts contribute to better efficiency. It has been observed that ducted propellers promote improved static thrust performance compared to an open air propeller with the same diameter and power loading. In theory this is due to the highly decreased slipstream contraction, consequently increasing the mass flow passing through the propeller disk, as illustrated in Figure 2.6. Having higher mass flow on the upstream surface results in suction pressure field and thus forward thrust on the duct. Even though the ducted propeller generally produces lower thrust than the open-air one, the total thrust, including the additional thrust created on the duct, result in much higher value, as represented in Figure 2.7.

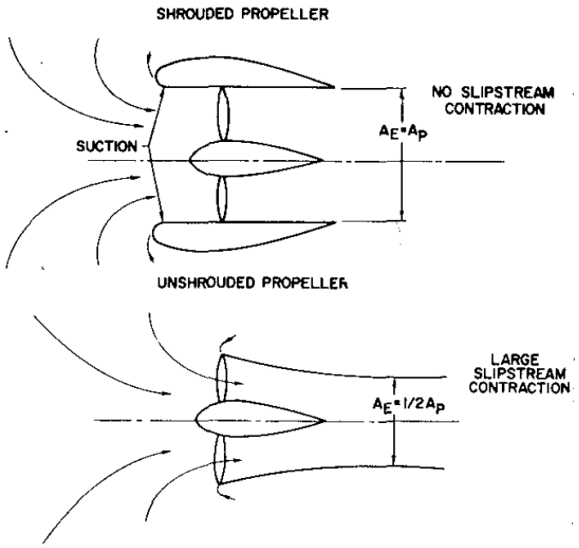

Figure 2.6: Momentum flow field comparison of ducted and conventional propellers at static conditions[24].

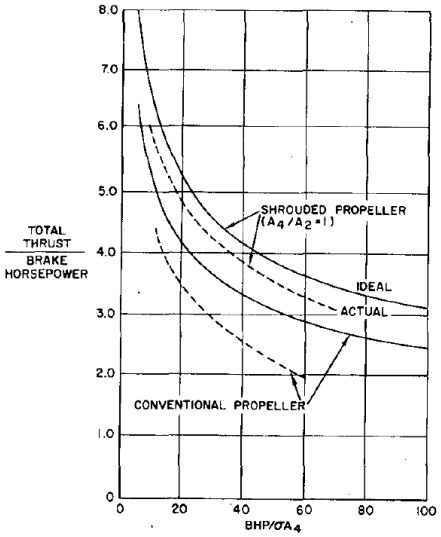

Figure 2.7: Static thrust per horse power of ducted and conventional propellers[24].

However, due to the slipstream contraction that is high at static conditions but decreases with high initial momentum, the gain in static thrust decreases rapidly with increasing the flight velocity. When considering viscous effects, those benefits are even lost and open propellers perform better in higher air speeds. This observation can also be made when comparing Figures 2.8 and 2.9 where the thrust and horsepower of the ducted propeller system at $M = 0.05$ and $M = 0.5$ respectively are shown. For lower Mach number the duct contributes to higher net thrust whereas at higher M, the contribution is detrimental due to the increased duct drag when operating at its critical or close to critical Mach number.

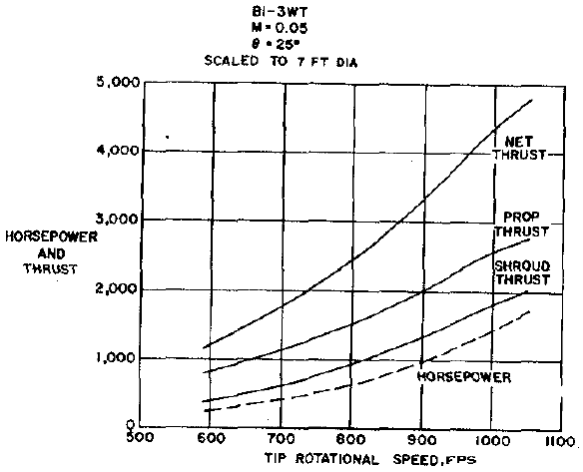

Figure 2.8: Horsepower and thrust for a ducted propeller system at Mach number of 0.05[24].

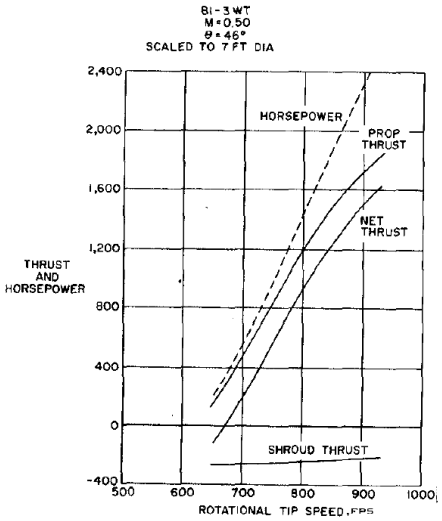

Figure 2.9: Horsepower and thrust for a ducted propeller system at Mach number of 0.5[24].

As discussed above, propellers show higher efficiency than jet and turbofan engines in certain conditions, which has also been recognised by NASA already in the 80s with their "Turboprop Project"[25]. However, the high noise generated by the propeller that can deteriorate the passengers' comfort has been of concern and lead to a research on possible noise shielding on the fuselage by installation of a short duct[26]. It has been concluded that attenuation of 7dB to 16.75dB propeller caused by the blades passing noise can be achieved. Even higher reduction is expected for the higher harmonics. It has been realised that if noise absorbing materials are applied, those benefits can be even bigger.

Reducing propeller noise has again become of interest in recent years due to higher efficiency requirements due to environmental concerns, constant thrive for passenger comfort of airlines as well as the increasing UAVs usage in variation of fields. In the late 90s Oleson and Patrick[27] carried out an experimental research, where the noise of an open propeller with the noise created by the shrouded propeller with and without silencers has been compared. It is concluded that the ducted configuration is louder than the open air one, which is explained by the strong rotor-stator interactions.

Recently, a study on the noise radiation of an unmanned aerial vehicle's ducted propeller has been carried out in TU Delft[28]. Both the omni-directional source and propeller contributions have been investigated, which shows that in the absence of incoming flow it is not straight-forward to evaluate the duct effect to the noise radiation. If free-stream velocity is non-zero the ducted and unducted systems have shown similar noise performance. No change in aerodynamic performance of the propeller with the duct being installed is seen as a prerequisite to be able to compare the noise radiation in the presence of the shroud to the open-air one. However, due to the sole purpose of introducing a duct to the system, this is highly challenging and thus the unducted configuration can be taken as representative for the ducted one as well.

2.2. DUUC DEFINITION

This section is dedicated to giving more information on the design choices and sizing of the DUUC staring with a discussion on the duct shape given in Section 2.2.1. This is followed by a systems sizing definition in Section 2.2.2. Section 2.2.3 will then elaborate on the concept's performance.

2.2.1. SHAPE OF THE PROPELLER'S DUCT

H. F. Mourão Bento[29] carried out his thesis research on investigating the aerodynamic interaction effects present in an unconventional ducted propeller design by running CFD simulations on circular, squared and open propeller systems, in order to understand their performance. Furthermore, by combining them he observed how their interactions affect the system's efficiency.

It has been shown that the isolated squared duct produces more drag than the circular one, which is mainly attributed to the higher wetted area as well as the higher boundary layer thickness at the inner corner and

consequently tendency of flow separation on the squared duct. Furthermore, the axial flow velocity inside the squared duct is found to vary for different azimuth angles, with higher velocity observed at locations far from the corner and lower ones at $\approx 45^o$. This has not affected the flow in the circular duct.

The study of the installed configurations concludes that the thrust produced by the propeller in circular duct is always significantly greater than the one in the squared. This can be explained by the fact that the slipstream contraction effect of the squared duct is decreasing towards the corners, therefore reducing the increase in angle of attack responsible for the thrust production of the duct. Furthermore, as discussed above, boundary layer separation is present at the corners of the duct that also decreases the geometry effectiveness. Last but not least, two counter rotating vortices at the corners have been observed to develop, which decrease the kinetic energy and thus momentum of the axial flow.

As a conclusion, the highest propulsive efficiency is observed in the propeller with circular duct, followed by the isolated propeller. 4.5% less efficient is the square duct system compared to the circular one. Thus, it can be deducted that circular shape is the most optimum in the case of the DUUC. However, it should be noted that square ducts could be found beneficial in alternative propulsion layouts, such as distributed propulsion, in future concepts.

2.2.2. WEIGHT DEFINITION

The work of van den Dungen[7] is one of the first analysis on the DUUC and, amongst other, discusses the methods implemented in the Aircraft Design Initiator for the weight definition of the DUUC's components. Those will be presented in the current section.

STRUCTURAL WEIGHT ESTIMATION

For the majority of the structural components, the Class 2 Weight Estimation method proposed by E.Torenbeek[30] has been applied.

The **Total Structural Weight** is calculated using Equation 2.3.

$$W_{structure} = W_{wing} + W_{fuselage} + W_{HTP} + W_{VTP} + W_{engine} + W_{LG} \tag{2.3}$$

The structure of the **Wing Group** is calculated using Equation 2.4 taken from Torenbeek for transport category aircraft with Take-Off mass of 5760kg or higher.

$$W_{wing} = W_{MZF} k_w b_s^{0.75} \left\{ 1 + \sqrt{\frac{b_{ref}}{b_s}} \right\} n_{ult}^{0.55} \left(\frac{b_s / t_r}{W_{MZF} / S} \right)^{0.30} \tag{2.4}$$

Where:
b = *Wing Span* $[ft]$
$b_s = b/cos\Lambda_{0.5c}$
$k_w = 1.70x10^{-3}$ $[-]$
n_{ult} = *Ultimate load factor*$[-]$
S = *Wing area*$[ft^2]$
W_{MZF} = *Zero Fuel Weight*$[lb]$
Λ = *Sweep angle at 50% chord* $[^o]$

It should be noted that the equation:

- Is valid for a retractable wing-mounted undercarriage configuration with non-wing-mounted engines;
- Accounts for high-lift devices and ailerons;
- Does not include spoiler and speed brakes weights.

As a primary structure, the wing weight is further analysed by higher Class 2.5 methods, discussed in more details in Section 2.3.2. They offer a balance between ability to estimate the weight with higher accuracy at the expense of higher, but not excessive, computational effort, typical for Class 3 and higher methods.

The **Body Group** has strong contribution to the overall structural weight and is calculated by Equation 2.5.

$$W_{fuselage} = k_{wf}\sqrt{V_D \frac{l_t}{b_f + h_f}} S_G^{1.2} \tag{2.5}$$

Where:
b_f = *Fuselage max width* $[ft]$
h_f = *Fuselage max depth* $[ft]$
k_{wf} = 0.021 $[-]$
l_t = *Distance between 1/4c points of wing root & HT root* $[ft]$
S_G = *Gross shell area*$[ft^2]$
V_D = *Dive speed defined by Equation 2.6*$[kts]$

$$\begin{aligned} V_D &\geq 1.25 V_C \\ M_D &\geq 1.25 M_C \\ EAS &= TAS\sqrt{\frac{\rho}{\rho_0}} \end{aligned} \tag{2.6}$$

Where:
EAS = *Equivalent airspeed* $[kts]$
M_C = *Cruise Mach number* $[-]$
M_D = *Dive Mach number* $[-]$
V_C = *Cruise speed* $[kts]$
V_D = *Dive speed* $[kts]$
TAS = *True airspeed* $[kts]$
ρ = *Air density at cruise altitude* $[kg/m^3]$
ρ_0 = *Air density at sea level* $[kg/m^3]$

Due to the high contribution to the weight of the aircraft, the fuselage weight is also further analysed by Class 2.5 methods.

The **Gear Group** weight is calculated using Equation 2.7 that is valid for conventional undercarriage only.

$$W_{LG} = k_{LG}\left\{A + BW_{TO}{}^{3/4} + CW_{TO} + DW_{TO}{}^{3/2}\right\} \tag{2.7}$$

Where:
A, B, C, D = *Coefficients, see Figure 2.10*
k_{LG} = *1.0 (low-wing) or 1.08 (high-wing)*
W_{TO} = *Take-Off weight* $[lb]$

Airplane Type	Gear Type	Gear Comp.	A_g	B_g	C_g	D_g
Jet Trainers and Business Jets	Retr.	Main	33.0	0.04	0.021	0.0
		Nose	12.0	0.06	0.0	0.0
Other civil airplanes	Fixed	Main	20.0	0.10	0.019	0.0
		Nose	25.0	0.0	0.0024	0.0
		Tail	9	0.0	0.0024	0.0
	Retr.	Main	40.0	0.16	0.019	$1.5\text{x}10^{-5}$
		Nose	20.0	0.10	0.0	$2.0\text{x}10^{-6}$
		Tail	5.0	0.0	0.0031	0.0

Figure 2.10: Coefficients used to landing gear weight determination[30].

Note: It is assumed that the coefficients for "Other civil aircraft" are valid for turpropeller aircraft as well.

The **Surface Controls** group's weight is calculated using Equation 2.8.

$$W_{sc} = k_{sc} W_{TO}{}^{2/3} \tag{2.8}$$

Where:
k_{sc} = 0.64 *Transport aircraft featuring powered controls and TE HL devices*
W_{TO} = *Take-Off weight* $[lb]$

PROPULSION WEIGHT ESTIMATION

The fact that the DUUC's propulsion system is a mix of conventional turbofan and turboprops asked for more elaborate propulsion weight estimation method that be representative. Naturally, the masses of the dry engine, propeller and nacelle, represented by the duct and pylon, need to be determined.

Turboprop

After investigating the turboprop weight estimation methods proposed by D. Raymer[31] and J. Roskam[32] and comparing their results for 16 typical turboprobs, van den Dungen observes that the Roskam's method is more accurate and updates this module in the Aircraft Design Initiator. He derives the relation given in Equation 2.9 from Figure 2.11.

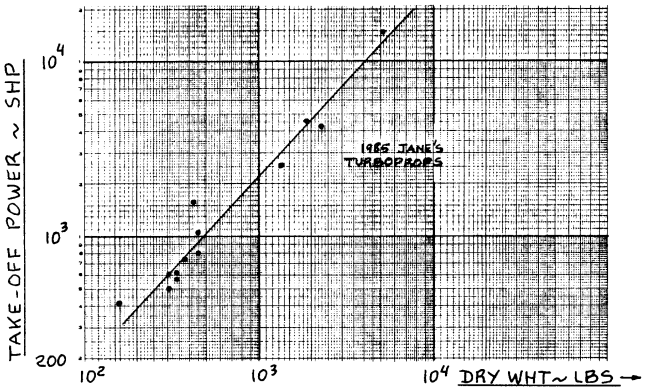

Figure 2.11: Turboprops: take-off horse power to dry weight[32].

$$W_{eng} = 500\left(P_{TO}10^{-3}\right)^{\frac{log(4000/500}{log(10^4/10^3)}} \tag{2.9}$$

Where:
P_{TO} = *Take-off break horse power*$[hp]$

Furthermore, for the engine's installation, Raymer adds 30%, which is implemented by Equation 2.10.

$$W_{cb} = 0.30 W_{eng} \tag{2.10}$$

However, having compared the estimated engine mass to the real ATR PW127M[33], those estimated were still over-predicting the real engine weight and it has been assumed that in the total dry engine mass also includes the centre body, which represents the aerodynamic shape of the engine. Thus, the estimate in Equation 2.10 is omitted and it is recommended that when the propeller is sized and an engine design has been established, more accurate weight should be given.

Propeller

Two methods for estimating the propeller mass have also been compared by van den Dungen, namely the one proposed by E.Torenbeek[30] and Hamilton Standard NASA[34], who compares nine actual propeller masses with their estimation. It is observed that the Hamilton Standard NASA method is more accurate and also is able to include the activity factor (AF), thus this is chosen for W_{fan} estimation, see Equation 2.11.

$$W_{prop} = K_w \left[\left(\frac{D_{prop}}{10}\right)^2 \left(\frac{N_{bl}}{4}\right)^{0.7} \left(\frac{AF}{100}\right)^{0.75} \left(\frac{RPM \cdot D_{prop}}{20000}\right)^{0.5} \left(\frac{P_{TO}}{10 {D_{prop}}^2}\right)^{0.12} \left(M_{des} + 1.0\right)^{0.5}\right] + C_W \tag{2.11}$$

Where:
AF = *Activity factor [-]*
C_W = *Counterweight, see Equation 2.12 [lb]*
D_{prop} =*Propeller diameter [ft]*
K_w = *210 Factor [-]*
M_{des} = *Design Mach number [-]*
N_{bl} = *Number of blades [-]*
P_{TO} = *Shaft power [hp]*

The following relation gives the counterweight for fibre glass bladed, constant speed, full feathered propeller:

$$C_W = 2.5\left[\left(\frac{P_{TO}}{RPM}\right)\left(\frac{M_{des}}{D_{prop}}\right) \cdot AF \cdot N_{bl}\right] \tag{2.12}$$

Duct

The duct is one of the heaviest components of the DUUC's propulsion system due to its size and at the same time, due to its the unconventional placement, has strong impact on the control and stability of the aircraft. Therefore, it affects strongly to the overall weight and performance of the aircraft. This as well as the fact that the duct is one of the main design features of the DUUC motivated van den Dungen to search for a weight estimation method that is dependent on the geometry rather than based on statistical analysis of conventional nacelles.

The Cranfield University Component-Based Method suggested by P.Lolis[35], which "is based on an internal pressure vessel theory with additional reinforcements for blade-containment" is then seen the most appropriate to be used. Two components contribute to the total thickness: the skin thickness required to meet the internal pressure and the one responsible for containing the blade in case of a blade release.

However, after this research was finalised, it was realised that van den Dungen used a method developed for pressurised vessels, which is not a valid assumption in the case of DUUC's ducts. Therefore, the duct's mass was estimated by nacelle weight estimation proposed by D. Raymer, see Equation 2.13[31],[2].

$$m_{duct} = 0.40 \frac{{l_{duct}}^{0.1} {w_{duct}}^{0.294} {n_{lim}}^{0.119} {m_{ps}}^{0.611} {N_{en}}^{0.984} S_{duct}}{N_{en}} \tag{2.13}$$

Where:
l_{duct} = *Duct length* $[ft]$
m_{ps} = *Power system mass* $[lb]$
N_{en} = *Number of engines* $[ft]$
n_{lim} = *Ultimate load factor* $[ft]$
S_{duct} = *Duct outer surface area* $[ft^2]$
w_{duct} = *Duct width* $[ft]$

This estimation is still based on statistical data on structural components that perform similar but not exact function as the ducts of the DUUC. Due to the high contribution on the aircraft performance and even though this was seen as a quick estimation, Class 2.5 weight estimation method is seen necessary.

Pylon

Pylon mass will increase in case the engine mass increases due to the higher stiffness required. However, due to time constraints, no physics-based method to determine the pylon mass has been developed yet. Therefore an assumption that it will be 30% of the total engine mass was made, see Equation 2.14[7].

$$W_{pylon} = 0.3(W_{eng} + W_{cb} + W_{fan} + W_{duct}) \tag{2.14}$$

As this was a rough estimation, this approach was revised later on. Due to the specific placement of the propellers and the ducts' dual function, there is strong resemblance between the pylon functionality and the one of a horizontal tail lead to using E.Torenbeek's[30] estimation for horizontal tail planes, with the assumption that they are fixed and not swept, see Equation 2.15[2]. It can be seen that the mass depends on the pylon area and the dive speed. The latter is observed to be dominant for light and relatively low-speed transport and business jet aircraft, where the manoeuvring loads are typically sizing.

$$m_{pylon} = k_{ugt} k_{comp} S_{pylon} \left(3.81 S_{pylon}^{0.2} V_D - 0.287\right) \tag{2.15}$$

Where:
k_{ugt} = *Factor used to if all moving tailes are present* $[-]$
k_{comp} = *Composite correction factor* $[-]$
S_{pylon} = *Pylon planform area* $[ft^2]$
V_D = *Dive speed* $[kts]$

Analogous to the duct mass estimation, this is still statistically-based estimation that uses data on conventional horizontal stabilisers. Even though the flow around the pylon might have similar characteristics to the one of the horizontal tail, stability is not its primary function and therefore more detailed analysis is required.

2.2.3. PERFORMANCE

An article by R. Vos and M. Hoogreef[2] summarises the basic features of the DUUC and compares the performance of three aircraft configurations as listed and illustrated below, see Figure 2.12.

1. High-wing T-tailed aircraft with wing-mounted propellers (WMP);
2. Low-wing aircraft with conventional tail and propellers mounted on the horizontal stabiliser's tips (TMP);
3. Low-wing aircraft with fuselage-mounted ducted propellers (FMDP).

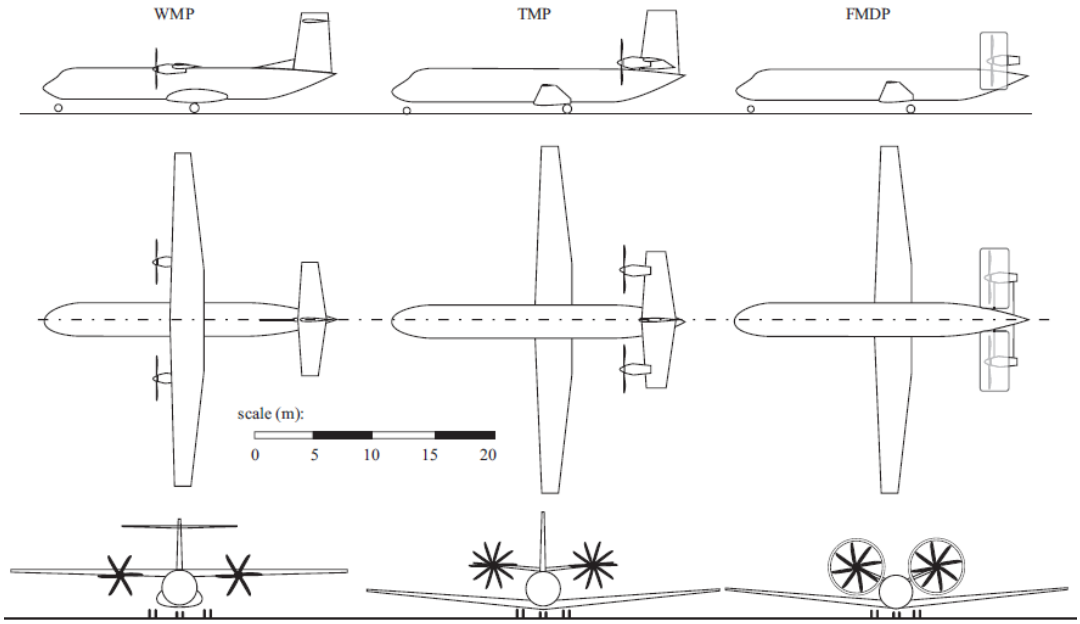

Figure 2.12: WMP, TMP and FMDP aircraft configurations[2].

Firstly, it should be noted that the sizing process chooses the configuration with highest wing and power loading. The three aircraft's performance is shown in Figure 2.13, where it can be seen that active constraints are take-off and landing distances as well as one engine inoperative climb gradient in landing configuration. Due to the differences in untrimmed drag polars, the cruise constraint is different for each aircraft.

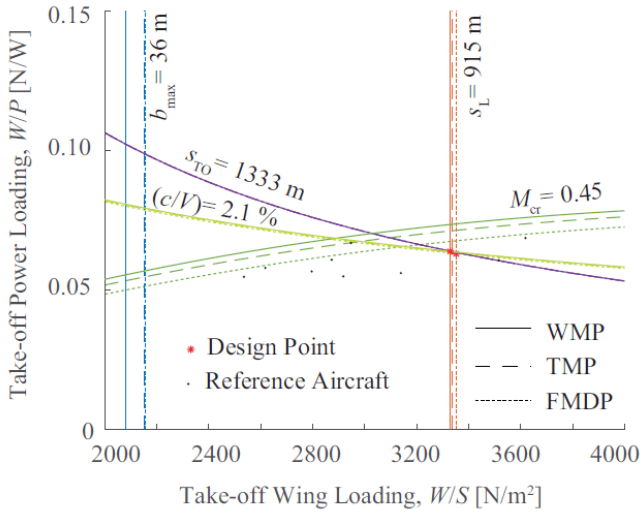

Figure 2.13: Wing versus power loading for WMP, TMP and FMDP aircraft configurations[2].

From the wing and power loading of each configuration it can be concluded that wing-mounted propeller has highest and the fuselage-mounted ducted propeller has the lowest cruise excess power.

The weight and balance analysis of the three configurations showed that engine weight for the tail-mounted and fuselage-mounted concepts is the same. Installing the duct on the latter adds 200kg to the weight, but this is lower than the combined weight of the horizontal and vertical tails. Furthermore, the weight of the duct is still an estimation.

The loading diagrams for the three configurations are presented in Figure 2.14. It can be seen that the centre of gravity shift of the wing-mounted is only 30%MAC, whereas it is 40% and 41% for the tail and fuselage-mounted configurations respectively. In addition to this, the CG location of the conventional aircraft is kept around 25%, which is expected to result in lower trim drag in comparison to the other concepts that have their centre of gravity positioned much further aft at 54%MAC and 47%MAC tail-mounted engine and DUUC configurations respectively.

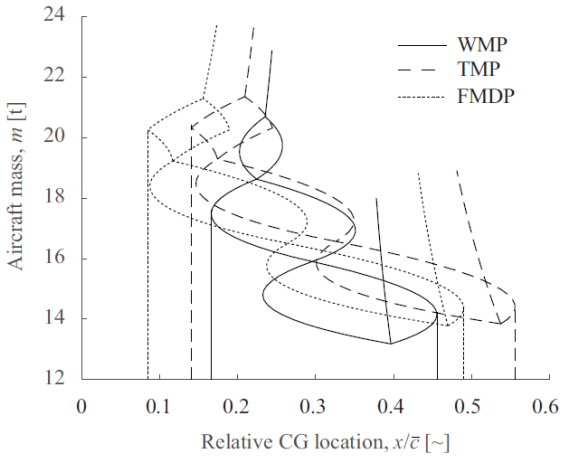

Figure 2.14: Loading diagrams for the WMP, TMP and FMDP aircraft[2].

The configurations' key performance indicators (KPI) are presented in Table 2.1, that gives a clear overview of the differences between them. The conventional aircraft shows lowest MTOM and there is an equal increase for the other two. The difference between OEM for tail and fuselage-mounted configurations is due to the increase of fuselage and tail mass for the first one and the integration of ducts with empennage on the DUUC.

Parameter	Unit	WMP	TMP	FMDP
$MTOM$	t	22.9	23.7	23.7
OEM	t	13.2	13.8	13.7
$Mission\ Fuel$	t	2.2	2.3	2.5
$Power\ Loading$	N/kW	63.7	63.5	63.0
$Wing\ Loading$	N/m^2	3330	3340	3350
$X_{\bar{c}/4}/L_{fus}$	–	0.47	0.49	0.52

Table 2.1: KPI for the WMP, TMP and FMDP configurations[2].

Consequently, comparison of the mission profiles can be made, see Figure 2.15. Apart from the climb performance that is related to the excess power available, the performance of the three configurations is shown to be very similar. This is however not true when looking into the payload to range diagrams given in Figure 2.16 where it can be seen that the conventional configuration performs better due to the optimised operational empty weight and lower friction drag.

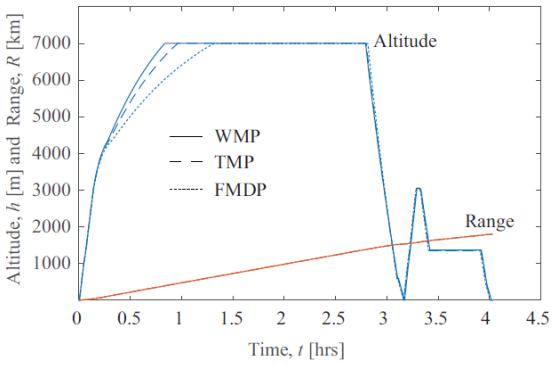

Figure 2.15: Mission profiles of the WMP, TMP and FMDP aircraft[2].

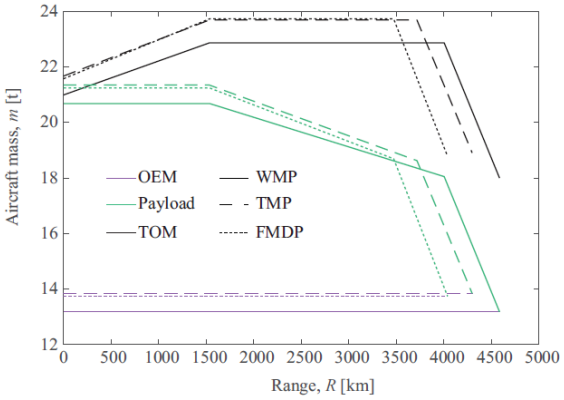

Figure 2.16: Payload-range diagrams of the WMP, TMP and FMDP aircraft[2].

2.3. STRUCTURAL SIZING METHODS

The variation in types and level of details of the information available at the different stages increases the challenge of predicting the component and therefore overall aircraft weight[36]. This can be detrimental to the design in number of ways, the two main ones being: if underestimation of the structural weight is present, the designer can potentially over-commit in front of the stakeholders and later on not be able to deliver on the specified requirements, which in the worst case scenario can even lead to cancellation of the project; on the other hand, if the structural weight is overestimated, potential improvements might be missed and, if not beneficial enough, the project can again be terminated.

This section first elaborates on three types of weight estimations, which are heavily applied in conceptual design. Class 1 and 2 Weight Estimation will be introduced in Section 2.3.1, which is followed by Section 2.3.2 discussing Class 2.5 Weight Estimation methods. Section 2.3.3 then presents methods used to analyse the engine nacelle structure in blade loss conditions.

2.3.1. CLASS 1 AND 2 WEIGHT ESTIMATION

Class 1 are statistical methods used for the initial determination of Maximum Take-Off Weight (MTOW), which is then divided in Operational Empty Weight (OEW), Payload Weight (PLW) and Fuel Weight (FW). Their inputs are the top level requirements such as range and cruise speed, from which reference aircraft are selected. Using empirical relations the operational empty weight can be estimated. Breguet's range and endurance relations, which depend on the lift to drag ratio, fuel consumption, cruise velocity and weight fractions, also statistically determined, are used for the initial performance estimation of the aircraft. Even though those methods give a very rough first aircraft weight estimation, they are essential for initiating a design. Such have been proposed by for example J.Roskam[37], D.Raymer[31] and E.Torenbeek[30].

Class 2 weight estimation methods are based on statistics and are applied after the initial MTOW, FW and OEW have been determined in Class 1 and the baseline geometry has been fixed. They use semi-empirical relations based on defined load factors and geometrical parameters to estimate the main components' weight. Even though they offer more detailed estimation than Class 1 methods and are able to illustrate the effect of the design choices at system level, they do not provide information on the detail design of the components. Higher classes are typically physics-based and implement Finite Element Methods(FEM) to size the primary structure and compute its weight. However, the higher resulting accuracy comes at the cost of higher preparation and computational time. Therefore, those are not typically used in the early design phases[36]. Examples of Class 2 methods are the ones of estimating the system weights defined by E.Torenbeek[30] and D.Raymer[31].

2.3.2. CLASS 2.5 WEIGHT ESTIMATION

Class 2.5 are quasi-analytical methods typically used in the conceptual design of primary structures that affect aircraft performance severely, such as the wing and fuselage. They offer the balance of having more accurate weight estimation without the excessive increase in computational effort as well as prior information on the geometry Class 3 and higher methods require.

The need of a methods to estimate the box wing weight as early as possible with high accuracy but limited computational time has been seen already in the 50s, which is also the motivation M.Burt[38] to suggest a method applicable to four types of box constructions. The procedures include design and stress calculations, mostly derived theoretically and supported with information on already existing aircraft and/or test specimen, but some also are purely derived from existing structures at the time. Additionally, the weight for joints and untapered sheets has been added as a function of the wing span and manufacturing methods.

In 1992 E.Torenbeek[39] realises that, even though Burt's method offers a design-sensitive estimation and considers the change in loading at different wing locations, the high amount of detailed information on the geometry required does not make it applicable for preliminary design. This consequently poses further challenges when attempting to evaluate the different design solutions' effect on the overall aircraft design. Thus, Torenbeek proposes a method in which the wing structure is divided into primary and secondary. For the primary structure, which he further splits into optimum weight one that depends on the bending, torsion, shear forces and includes the ribs, and the non-optimal weight that takes into account the non-taper, skin, cut-outs, joints, fairings and others, he gives analytical weight estimation methods. The secondary structure consists of high lift devices and control surfaces, whose weight is estimated by empirical relations.

More recently, A.Elham, la Rocca and M.J.L. van Tooren[36] have developed a Class 2.5 wing weight estimation method that, in analogy to the previously discussed ones, uses elementary box sizing methods to determine the required material for carrying the load combined with empirical relations to account for the components weight contributions. The method implements a new definition of the parameter called "airfoil effective distance", which contributes to a higher accuracy and design sensitivity by relating the wingbox weight to the geometry of the wing sections. Furthermore, it facilitates relating the outer aerodynamic shape to the wight estimation of the wing upper and lower panels independently, thus offering the possibility to optimise their design for their specific critical load case. At the same time computational time is highly reduced when compared to running a finite-element analysis.

The Aerospace Engineering department at Delft University of Technology then proposed another wing weight estimation method, defined by R.Elmendorp et al.[40], the main driver of which is to define a universal method that can analyse non-conventional wing shapes, such as the box wing. It represents the wing as a number of connected beams with length, skin and spar thicknesses, which leads to their own moment of inertia and stiffness matrices. A FEM model following the method of R.D.Cook et al.[41] solves for the beams' deformations and stresses. Furthermore, boom idealisation as proposed by Megson[42] represents the wingbox by upper and lower booms and connecting skins. The required areas are then calculated such that it is sufficient to meet the load in the corresponding beam. An iteration is carried out where the skin and spar thicknesses or boom areas are increased until all reserve factors, defined as the ratio $\sigma_{allowed}/\sigma_{applied}$), are higher than 1. Having the material density, the structural weight is consequently calculated.

2.3.3. BLADE LOSS STRUCTURAL IMPACT

Blade separation can occur due to many reasons such as fatigue, the probability of which is increased due to the high dynamic loading on the blades, bird strike or other foreign object damage[43]. As it could potentially not only impact the engine but also cause damage to the surrounding structure, this failure has been recognised as one of he prime concerns in modern commercial aviation propulsion. Thus, it is naturally regulated through requirements on the engine performance in such occurrence posed by the responsible authorities such as EASA[44] and FAA[45] and others. Due to the high cost and risks of such campaign, strong efforts have been put in predicting the structural behaviour in this highly dynamic and complex event with the view that in future no need of actual test but numerical simulation will be sufficient to show evidence for compliance with the regulations.

The severity of such a failure and the potential consequences can be illustrated by an example, such as the accident with Embraer-120RT in August 1995. Due to in-flight fatigue fracture and consequent separation, one of the propeller blades impacted the engine's nacelle, which resulted in loss of wing lift, excessive drag and low directional control of the aircraft. The accident caused captain's and four passengers' death. Due to their injuries four more passengers passed away in the following three moths. The flight attendant, first officer and eleven other passengers suffered serious injuries[46].

More recently, in October 2013 an incident with Fokker F-27 Friendship 500F featuring two Rolls-Royce Dart 532-7 engines occurred. During climbing the flight crew heard sound of explosion coming from the cargo hold that was also accompanied by visual and sound alarms signalling for an issue with Engine No.1 po-

sitioned on the left hand side. After the unsuccessful captain's attempt to activate the corresponding fire extinguisher the pilot performed visual inspection and saw no fire but part of the engine was missing. The airplane remained controllable and the crew managed to return and land successfully at Paris-Charles de Gaulle Airport. Shortly after it was realised that the propeller blades sliced through the fuselage and exited on the other side. Thankfully, as there were no passengers and all members of the flight crew were in the cockpit, no fatalities took place[47].

CASE DESIGN

In case of blade separation the casing needs to contain all parts that might come off. Most recent design methods use advanced FEM tools, which require high computational power and thus are not suitable for conceptual design analysis. A few analytical methods have been identified, reviewed and improved by S.Bretschneider et al.[48]. They typically relate the required casing thickness to the kinetic energy of the blade fragment, which depends on the compressor shaft rotational speed, the flow velocity, pressure ratio at the corresponding stage and interaction of the separated blade with the remaining ones and components downstream. Simplified expression of the kinetic energy is given in Equation 2.16, where the axial velocity, rotation around the segment's centre of gravity and the interaction with other components are neglected.

$$E_{kin} = \frac{m_s \cdot R_s^2 \cdot \omega^2}{2} \tag{2.16}$$

Where:
m_s = *Mass of blade segment [kg]*
R_s = *Radius of blade segment [m]*
ω = *Rotational speed [rpm/s]*

Two methods of determining the required casing thickness in blade loss have been compared. The solution proposed by Goldsmith and Hibbler, further calibrated by the empirically determined factor S_1, is given in Equation 2.17.

$$t_{case_{Goldsm}} = \frac{E_{kin} \cdot E}{\sigma_{max}^2 \cdot t_{bl} \cdot c_{bl}} \cdot S_1 \tag{2.17}$$

Where:
E = *Case Young's modulus [Pa]*
c_{bl} = *Chord of the separated blade [m]*
S_1 = *Correction factor = 0.4 [-]*
t_{bl} = *Thickness of the separated blade [m]*
σ_{max} = *Case maximum yield stress [Pa]*

S.Bretchneider also studies the estimation suggested by Fedrotschenko, where the thickness is expressed by Equation 2.18 with the empirical factors S_1, κ, ν and ψ.

$$t_{case_{Fedrot}} = \sqrt{\frac{E_{kin}}{0.65 \cdot \xi \cdot \sigma_B \left(\nu + \psi + \frac{\kappa}{2}\right) \cdot (2c_{bl} + 2t_{bl})}} \cdot S_1 \tag{2.18}$$

Where:
c_{bl} = *Chord of the separated blade [m]*
t_{bl} = *Thickness of the separated blade [m]*
S_1 = *Correction factor = 2 [-]*
ξ = *Consolidation coefficient = 1.3 [-]*
κ = *Coefficient describing the shear portion of overall deformation = 2.5 [-]*
ν = *Coefficient describing the ductile portion of overall deformation = 0.7 [-]*
σ_B = *Case maximum bending stress [Pa]*
ψ = *Coefficient describing the elastic portion of overall deformation = 0.05 [-]*

Figure 2.17 gives an overview of the thickness estimations with the different methods discussed. S.Bretscheider[48] has concluded that Goldsmith offers good approximation of the compressor wall thickness for lower stages and the method proposed by Fedortschenko gives good estimate for higher stages.

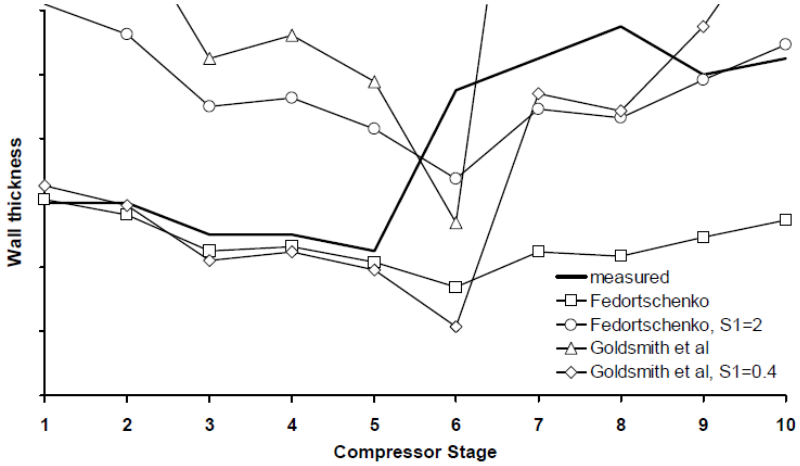

Figure 2.17: Case wall thickness approximation with different methods for 10 compressor stages[48].

ENGINE MOUNT SYSTEM

Apart from the extreme impact loads on the casing due to blade loss, it also leads to high imbalance in the propeller system, which causes powerful engine vibrations. The mechanics behind this propeller imbalance are simply explained by looking at the hub and all the blades as a system. In order to rotate, the engine exerts torque that is transmitted to the blades through the hub. Those in return generate lift and drag and the resultant force from all the components on all blades forms the thrust. However, if one (or more) of the blades separates, the forces that were compensating each other prior the failure are no longer in equilibrium. This is experienced by the pilot as a severe engine damage or complete loss and stabilisation of the aircraft is challenging. Furthermore, if not absorbed by the engine mounting system, transmission of the vibrations can be detrimental to the structural and possibly aerodynamic performance of the surrounding structure[49].

This was thoroughly studied by I.Armendáriz et al. by building a detailed FEM model, which is documented in [50],[49],[51]. The model includes the engine, which is defined by limited mass and stiffness matrices, as well as the mounting system, represented by additional mass and non-linear stiffness matrices, and the pylon to wing attachments, which allows for the analysis of impact to the wing structure. Figures 2.18 and 2.19 illustrate the model set-up.

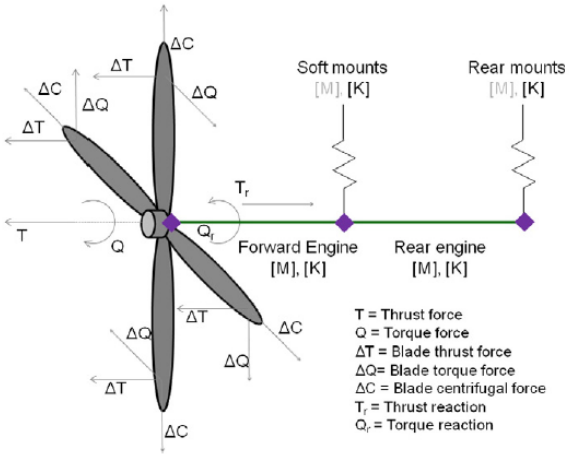

Figure 2.18: Model of aerodynamic forces over the blades and engine scheme[49].

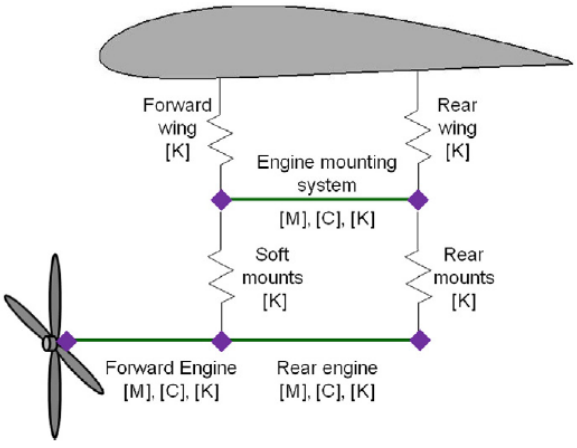

Figure 2.19: Model of blades, engine and wing interaction[49].

Furthermore, structural damping has also been introduced. The problem is therefore defined by Equation 2.19. The non-linear behaviour of the elastomeric attachments have been included in each axis.

$$My'' + Cy' + Ky = F \longrightarrow My(t)'' + Cy(t)' + Ky(t) = F_{nonlinear}(y,t) \tag{2.19}$$

The forces that occur in case of blade separation are converted to kinetic and some elastic energy by representing them as displacements. Those then affect the wing through the mounting system due to the force boundary conditions. If no structural damping is introduced, the engine and mounting system are observed to vibrate violently and with constant energy. Damping typically is expressing the decrease in oscillation magnitude and is introduced by the parameter C in Equation 2.20. The loss factor represents the energy dissipation per radian and is calculated using Equation 2.20.

$$C = \frac{2\beta}{\Delta t} M \qquad With:\ \beta = \eta\omega\Delta t \tag{2.20}$$

Where:
β = *Structural damping parameter*
η = *Structural damping coefficient*
Δt = *Time step[s]*
ω = *Propeller frequency [rad/s]*

Separation of the blade introduces forces and moments on the hub due to the imbalance caused by the moment and force not being compensated. Those are given in Equation 2.21, where F_c is the blade centripetal force, M_{oop} - moment introduced by the hub on a blade in normal operations, X corresponds to the longitudinal axis, Y is aligned with the wing span and Z is opposite to the gravity.

$$\begin{aligned} F_y &= -F_c cos(\omega t) \qquad F_z = -F_c sin(\omega t) \\ M_y &= M_{oop} sin(\omega t) \quad M_z = -M_{oop} cos(\omega t) \end{aligned} \tag{2.21}$$

Number of load cases and parameters effects on the structural response have been analysed, such as blade loss angular position, RPM sensitivity, blade loss size, structural damping and elastomer attachments' strength and stiffness. The study compares the results obtained for the engine only and when the mounting system is added and has concluded that, naturally, the pylon presence has strong impact on the structural performance by increasing the time until complete system failure. Focussing on the results of engine with mounting system, the separated blade's size is recognised as the parameter affecting the analysis most severely, followed by the angle of separation and damping. Combination of parameters have shown that blade size together with structural damping are the most influential.

3

METHODOLOGY

This chapter presents the chosen methodology to solve the problem at hand, namely define a design-sensitive and robust weight estimation method for the propulsive empennage. Section 3.1 firsts elaborates on overall modelling and top-level assumptions taken throughout the analysis. Duct sizing method is then presented in Section 3.3, followed by pylon analysis method discussed in Section 3.4.

3.1. MODELLING, ASSUMPTIONS AND RESTRICTIONS

The basic purpose of aircraft's structures is to resists and transmit the experienced loads, to provide the aerodynamic shape, assure no deformations will result in decreased performance and to protect the passengers, payload, systems, etc. from the environmental conditions during flight. In most aircraft these requirements next to low weight aim are satisfied by thin shell structures that are typically reinforced by stiffening longitudinal and transverse components[42]. Due to the multifunction of both duct and pylon geometry, some additional requirements need to be mentioned.

Requirements on lifting surfaces have been summarised by D.Howe[52], where the wing is taken as reference structure, but the same discussion can be transferred to all lifting surfaces such as horizontal and vertical tails. The main design consideration is the need of being a span-wise and chord-wise beam that has sufficient stiffness to carry the torsional and bending loads.

In the current case, the duct is considered cylindrical shell structure with symmetrical airfoil cross-section, which provides aerodynamic force when put under an angle of attack, and an engine casing. The pylon is represented as straight wing with symmetrical airfoil and engine mounting system. Figure 3.1 illustrates the propulsive empennage representation. Figure 3.2 then shows the integration between centre body, pylon and duct with their respective dimensions.

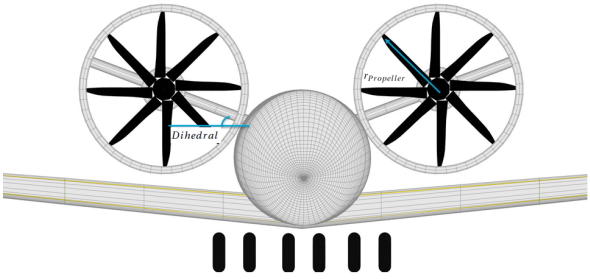

Figure 3.1: Concept modelling front view.

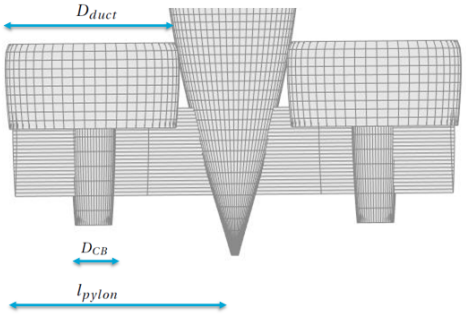

Figure 3.2: Concept modelling top view.

A few assumptions on the attachments will be made:

(1) The pylon is clamped to the fuselage: No displacement in directions parallel to the pylon span, flow stream or weight vector is allowed; No rotation at the pylon attachment is also allowed. Thus, three reaction forces and three reaction moments are present at the clamped end.

(2) The ducts are clamped to the pylons at two locations on the circumference. Thus, three reaction forces and three reaction moments are present at each clamped end.

3.2. TOP LEVEL LOADING

It is common knowledge that when sufficiently high load is applied on any structure, if it has some ductility, it will first deform in a elastic fashion and when the load is further increased, a plastic deformation will follow and ultimately the structure will break under static loads. If brittle materials are used, the structure will break when a sufficiently high load is applied without showing first signs of weakening, such as deformation. In order to avoid excessive deformations and failure of structures, their response under loading needs to be calculated prior production. In case the structure is not capable to carry the applied load, the material or geometry has to be changed. In most cases this, especially the latter option, results in higher component thickness and consequently weight. As the safety but also efficiency of aircraft structures are of prime importance, static stress analysis is of prime importance and there have been well-established methods available to design optimal and safe structures, such as for example the ones proposed by T.H.G.Megson[42].

Next to this vibrations experienced by the structure can also be detrimental to aircraft's structure. They are the part of dynamics analysis that represents the repetitive motion, excessive amount of which is typically unwanted in aircraft structures and systems as it leads to fatigue and potentially failure. Note that the analysis will be focussing on the mounting system's response to vibrations caused by the propeller rotation in the presence of imbalanced motion in blade-off conditions. However, the phenomenon will also be simulated in the static analysis to observe what static loading can the structure support in those conditions.

It should be noted that the control surfaces also cause loading on the structure. However, those have not been estimated and are thus not included in the analysis. Furthermore, in case of blade loss, it is very likely that those will be damaged. In later design stage it should be shown that the aircraft has sufficient stability and control to be able to continue safe operations until closest landing opportunity. This, however, has also been considered out of the scope of the current research.

3.3. DUCT SIZING

Figure 3.3 represents the Catia model of the duct with its cross section illustrated on the right. This section will cover the method used to size the duct starting with presenting the critical load cases in Section 3.3.1. Modelling representation will be discussed in Section 3.3.2. Section 3.3.3 will then elaborate on estimation of the aerodynamic forces, which will be translated to nodal loads in Section 3.3.4. Lastly, Section 3.3.5 will define the method to obtain the protective thickness needed in case of blade loss.

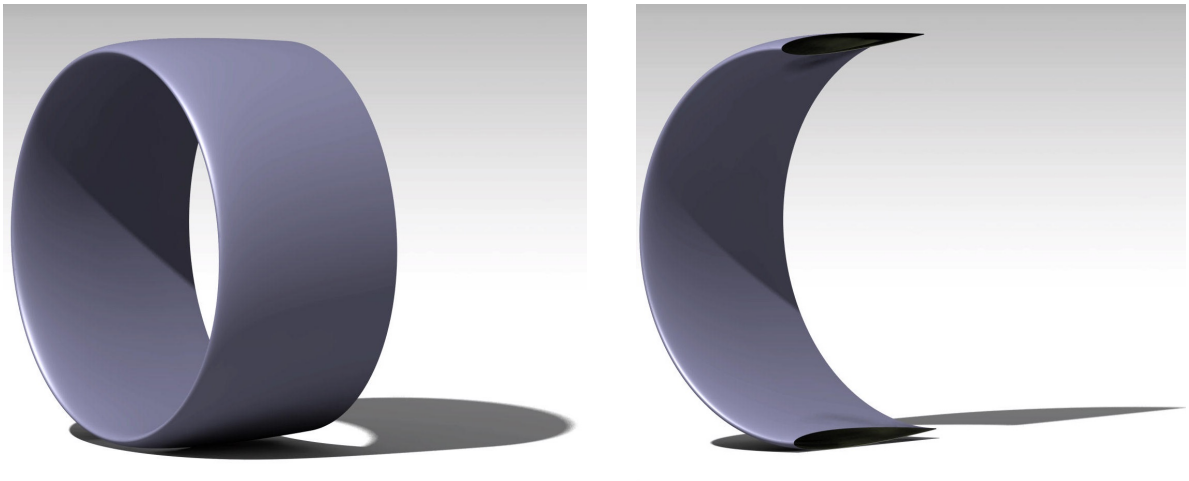

Figure 3.3: Duct Catia model.

Firstly a set of inputs, see Table 3.1, need to be defined.

Parameter	Defined by module	Dependent on
Diameter	Geometry definition	Propeller design*
Airfoil	Geometry definition	Design choice
Aspect Ratio	Design choice	Propeller design*
Pylon installation angle	Constant	Propeller design*
Number of beams	Variable	Pylon installation angle
Material		Design choice
Aerodynamic loads		Discussed in Section 3.3.3
Blade geometry	Geometry definition	Propeller design*

Table 3.1: Required method inputs.

* Please note that the engine and propeller design suitable for this concept have not been defined yet. As this design will affect severely the analysis, it is recommended that the corresponding parameters will be defined with more accuracy.

3.3.1. CRITICAL LOAD CASES

There are two prime functions of the ducts: to provide sufficient longitudinal and directional stability to the aircraft, which defines the duct's area, and improve the propulsive system by improving static thrust. Furthermore, the nacelle function is to reduce the noise experienced in the cabin and provide higher safety in case of blade loss failure. It should be noted that changing the duct's shape is out of scope from the current analysis as it is effects the propeller performance drastically. Thus, current shape defined by an aspect ratio of 2, chosen based on the researched discussed in Section 2.1.2, and allowing for small tip clearance is kept constant. It is recommended that future work on optimising those together with the propeller and control surfaces design is done.

Firstly, the duct is acting as a tail under the unusual load caused by th engine, thus one of the most critical conditions when maximum performance from both empennage and engine is required, namely the take-off, is going to be studied. Furthermore, in order to secure minimum drag during the longest segment of flight, engine cowling is typically designed for cruise conditions, which is going to be considered here as well. Next to this, as discussed by E.Torenbeek[30], the tail group of a transport category aircraft is typically sized in diving conditions, when the dynamic pressure is highest while at the same time stability of the aircraft is crucial. Last but not least, as the discussion in Section 3.3.5 proves, blade loss conditions are of prie interest when designing the nacelle structure and the corresponding loads are therefore going ot be considered in the following analysis.

Thus, to summarise this, the critical load cases that will be considered for the design are:

(1) Take-off with the engine at full thrust;
(2) Cruise;
(3) Diving conditions, when maximum speed and therefore dynamic pressure on the duct is expected;
(4) Propeller blade loss failure.

Load case (4) will be used for designing a blade containment layer to be placed on the duct's inner side.

3.3.2. MODELLING AND STRESS CALCULATION

Figure 3.4 represents the duct FEM, where it can be seen that the structure is represented by a number of beams and nodes. The number of beams are determined based on the pylon incidence angle in order to coincide with the duct's attachments as much as possible and still have beams with equal length. Essentially, the problem is transformed into a spring-force system as illustrated in Figure 3.5.

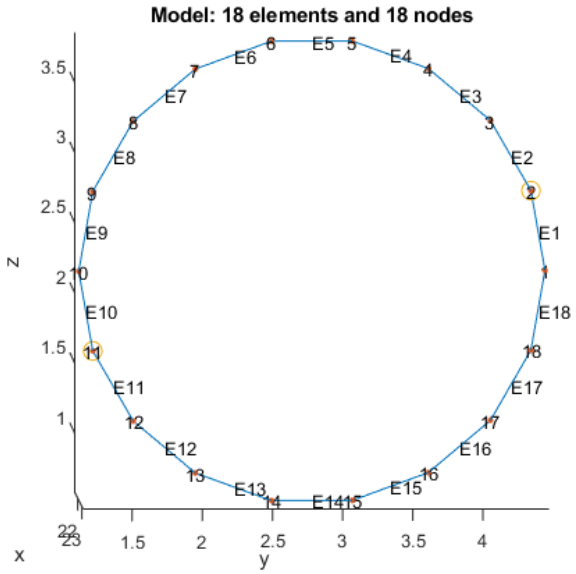

Figure 3.4: Duct FEM representation.

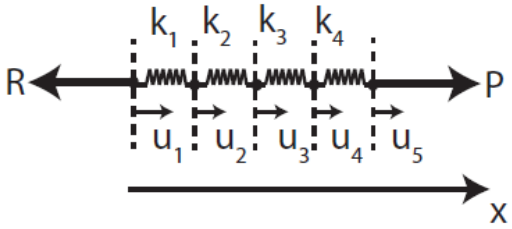

Figure 3.5: Spring-fore system representation[53].

Each beam has its cross section and moment of inertia, which depend on the skin thickness, and are used to define the 3 dimensional beam stiffness matrix as given by R.D.Cook et al.[41]. Having the loads applied to each node allows us to define the equilibrium equations, see Equation 3.1, and solve for the displacements. Using those and having the material Young's modulus E, the stresses are obtained using Equation 3.2. Consequently, having the beams stiffness matrix, the forces on the elements are defined.

$$\mathbf{F} = [K]\mathbf{u} \tag{3.1}$$

$$\xi = \frac{u_{i+1} - u_i}{l} \qquad \sigma = E\xi \tag{3.2}$$

The three dimensional beam stiffness matrix depends on the moment of inertia and cross sectional area. A definition is given below, where the corresponding factors are listed in Equations 3.3 - 3.8. Note that the value of k_y is set to 2, which is commonly used for think-walled tube[41].

$$[\mathbf{k}] = \begin{bmatrix}
X & 0 & 0 & 0 & 0 & 0 & -X & 0 & 0 & 0 & 0 & 0 \\
 & Y_1 & 0 & 0 & 0 & Y_2 & 0 & -Y_1 & 0 & 0 & 0 & Y_2 \\
 & & Z_1 & 0 & -Z_2 & 0 & 0 & 0 & -Z_1 & 0 & -Z_2 & 0 \\
 & & & S & 0 & 0 & 0 & 0 & 0 & -S & 0 & 0 \\
 & & & & Z_3 & 0 & 0 & 0 & Z_2 & 0 & Z_4 & 0 \\
 & & & & & Y_3 & 0 & -Y_2 & 0 & 0 & 0 & Y_4 \\
 & & & & & & X & 0 & 0 & 0 & 0 & 0 \\
 & & & & & & & Y_1 & 0 & 0 & 0 & -Y_2 \\
 & & & & & & & & Z_1 & 0 & Z_2 & 0 \\
 & & & & & & & & & S & 0 & 0 \\
 & & & & & & & & & & Z_3 & 0 \\
 & & & & & & & & & & & Y_3
\end{bmatrix}
\begin{matrix} u_1 \\ v_1 \\ w_1 \\ \theta_{x1} \\ \theta_{y1} \\ \theta_{z1} \\ u_2 \\ v_2 \\ w_2 \\ \theta_{x2} \\ \theta_{y2} \\ \theta_{z2} \end{matrix}$$

symmetric

$$X = \frac{AE}{L} \tag{3.3}$$

$$Y_1 = \frac{12EI_z}{(1+\phi_y)L^2} \tag{3.4}$$

$$Y_2 = \frac{6EI_z}{(1+\phi_y)L^2} \tag{3.5}$$

$$Y_3 = \frac{(4+\phi_y)EI_z}{(1+\phi_y)L} \tag{3.6}$$

$$Y_4 = \frac{(2-\phi_y)EI_z}{(1+\phi_y)L} \tag{3.7}$$

$$\phi_y = \frac{12EI_z k_y}{AGL^2} \tag{3.8}$$

In order to calculate the moment of inertia, the airfoil is represented by a trapezoid as illustrated in Figure 3.6. Equations 3.9 then give the corresponding moments of inertia with a, b and c defines as in Figure 3.6. Note that the cross moment of inertia I_{xy} is zero due to symmetry[42].

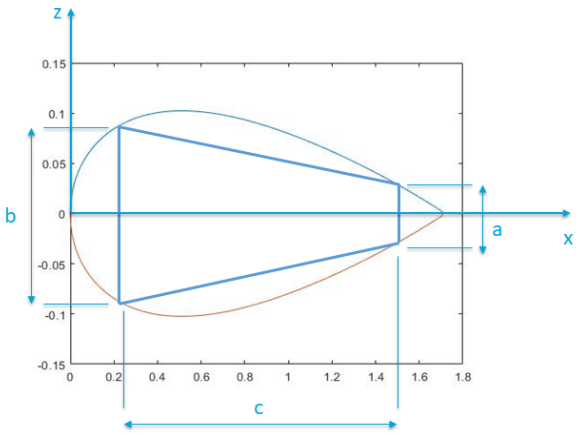

Figure 3.6: Duct cross-section representation.

$$I_x = \frac{1}{46} c(a+b)(a^2+b^2) \tag{3.9}$$

$$I_z = \frac{1}{36} c^3(b^2+4ab+a^2a+b)(a+b) \tag{3.10}$$

Having determined those as well as the beam loads from the FEM, we can then calculate the bending, axial and shear stress in each skin using the procedure outlined by T.H.G.Megson[42].

The geometry in Figure 3.7 is under bending stress as expressed in Equation 3.11. Furthermore, the axial stress is calculated using $\sigma = \frac{F}{A}$ with F being the beam axial load and A its cross section. Adding it to 3.7 gives the total normal skin stresses.

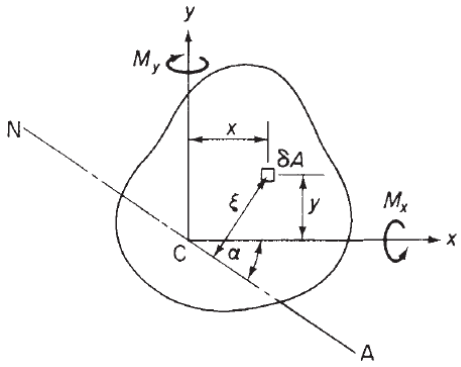

Figure 3.7: Geometry under bending stress[42].

$$\sigma_z = \frac{M_y I_{xx} - M_x I_{xy}}{I_{xx} I_{yy} - I_{xy}^2} x + \frac{M_x I_{yy} - M_y I_{xy}}{I_{xx} I_{yy} - I_{xy}^2} y \tag{3.11}$$

Where:
I_{xx} = *Second moment of inertia around the x-axis* $[m^4]$
I_{xy} = *Product second moment of inertia around the y-axis* $[m^4]$
I_{yy} = *Second moment of inertia around the y-axis* $[m^4]$
M_x = *Moment around the x-axis* $[Nm]$
M_y = *Moment around the y-axis* $[Nm]$
x = *Horizontal location of calculation point with respect to the neutral axis* $[m]$
y = *Vertical location of calculation point with respect to the neutral axis* $[m]$

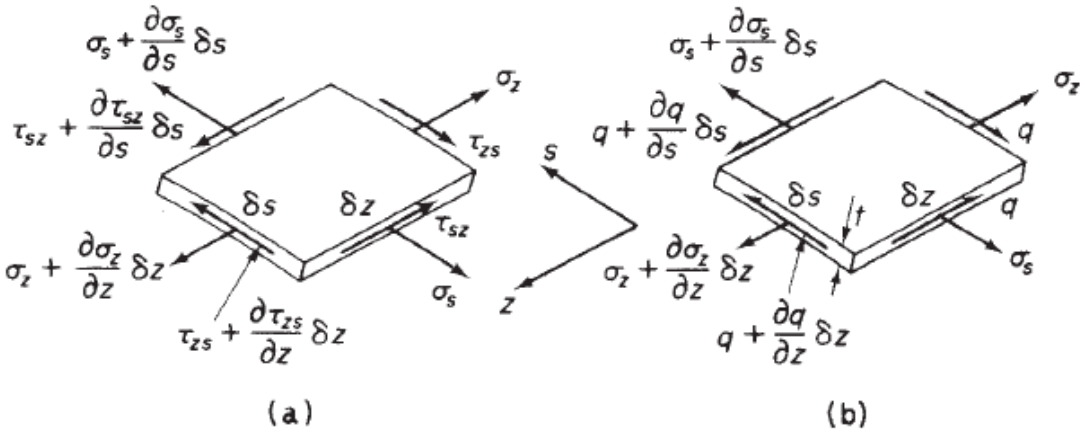

Figure 3.8: (a) General stress on element; (b) Direct stress and shear flow on element[42].

Figure 3.8 represents the general stress on an element to the left and the direct stresses and shear flow of an element on the right. Then the shear stress is given by Equation 3.12, where it can be seen to depend on the shear flow and the element thickness only. Following Equations 3.13 and 3.14, the shear flow depends on the shear force at the element, moments of inertia as well as the thickness and corresponding element the length.

$$\tau = \frac{q}{t} \tag{3.12}$$

Where:
t = *Element thickness* $[m]$
q = *Shear flow, see Equation 3.13* $[N/m]$

$$q_s = q_b + q_{s,0}$$

$$q_s = -\left(\frac{S_x I_{xx} - S_y I_{xy}}{I_{xx} I_{yy} - I_{xy}^2}\right) \int_o^s t x ds - \left(\frac{S_y I_{yy} - S_x I_{xy}}{I_{xx} I_{yy} - I_{xy}^2}\right) \int_o^s t y ds + q_{s,0} \tag{3.13}$$

Where:
q_b = *Basic shear flow* $[N/m]$
$q_{s,0}$ = *Constant shear flow, see Equation 3.14* $[N/m]$
S_x = *Shear force in x-direction* $[N]$
S_y = *Shear force in y-direction* $[N]$

$$S_x \eta_0 - S_y \xi_0 = \oint p q_b ds + q_{s,0} \oint p ds \tag{3.14}$$

Where:
p = *Distance to the axis of shear flow, see Figure 3.9* $[m]$
η_0 = *Vertical distance from shear force x-axis to element centroid, see Figure 3.9* $[m]$
ξ_0 = *Horizontal distance from shear force y-axis to element centroid, see Figure 3.9* $[m]$

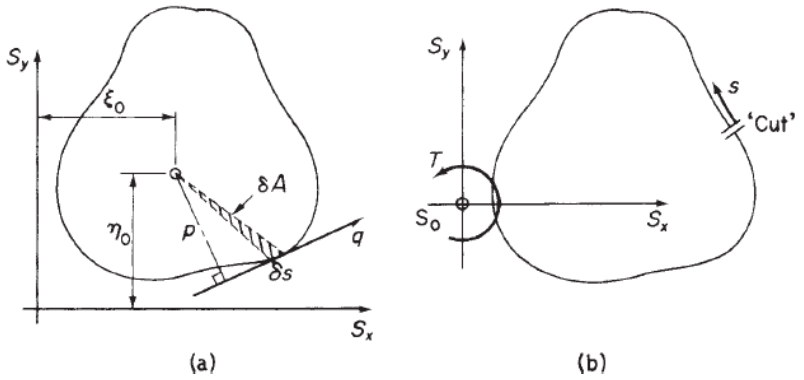

Figure 3.9: (a) Calculation of constant shear flow $q_{s,0}$; (b) Equivalent loading on the cut section[42].

If any of the skin stresses is found to be higher than the allowable one, the respective thickness is increased

by a factor corresponding to and the analysis is rerun. This is repeated until the whole structure is capable of carrying the corresponding loads.

3.3.3. AERODYNAMIC LOADS

As discussed in Section 2.1, ring wings have been studied since as early as the 30. A estimating the aerodynamic forces and defining a robust method to do so however has proven to be a challenging task. Aerodynamic analysis of the DUUC's ducts and definition of method to estimate those has been the focus of V.Harinarain Master's thesis[8], who has also verified his results against data obtained during testing of the prototype's propulsive empennage system in the low-speed wind-tunnel of Aerospace Engineering faculty at Delft University of Technology.

LIFT

Harinarain has concluded that Weissinger's method describes the lift curve slope, defined in Equation 3.15 of the duct accurately[18].

$$C_{L_\alpha,duct} = \frac{\pi}{2}\xi_W c_{l_\alpha} \tag{3.15}$$

$$\textit{Where: } \xi = \frac{1}{1+\lambda(\pi/2)+\lambda\ arctan(1.2\lambda)} \tag{3.16}$$

$$\lambda = \frac{1}{AR} \tag{3.17}$$

$$AR = \frac{D_{duct}}{c_{duct}} \tag{3.18}$$

Approximation of the power-off lift of the duct's linear curve part only is given in Equation 3.19, where α is the free stream angle of attack.

$$C_{L_{duct}} = C_{L_\alpha,duct} \cdot \alpha \tag{3.19}$$

In order to add the propeller effect in power-on conditions a factor k_{prop} is defined and its contribution to the lift is applied in the following way:

$$C_{L_\alpha,duct,on} = (1 + k_{prop}) C_{L_\alpha,duct} \cdot \alpha \tag{3.20}$$

Where:
$k_{prop} = 0.2\sqrt{T_{c_{propcb}}}$
$T_{c_{propcb}}$ = *Propeller and centre body thrust coefficient [-]*

Obtaining the $T_{c_{propcb}}$ has proven to be rather challenging and Harinarain first attempt is to extract i directly from DFDC, a MIT tool that has been based on another powerful tool of theirs, XROTOR[56], and aims to analyse axisymmetric ducted rotor[57]. However, the tool has not been completed nor verified and in the process of checking the credibility of the results, Harinarian observes that it does not accurately predict the propeller thrust. Therefore, he defines the following procedure of obtaining the lift coefficient:

1. Obtain the propeller thrust from XROTOR at the free stream velocity.
2. In order to simulate the presence of the duct, two options are given: inflow velocity profile velocity can be obtained by running DFDC with duct only and extracting the corresponding velocity profile or a correction to the velocity using the continuity equation should be applied. For simplicity and robustness, the second options is chosen in the current analysis;
3. Due to the presence of the duct, the thrust is needs to be corrected by applying the inverse Prandtl tip correction factor defined in Equation 3.21[58];
4. Using the obtained propeller thrust as an input to DFDC as well as the correct geometry,the propeller and centre body thrust is then extracted from DFDC and used to calculate k_{prop} from Equation 3.20.

$$F_P = \frac{2}{\pi} cos^{-1}\left[exp\left(-\frac{N(1-r)}{2rsin\phi}\right)\right] \tag{3.21}$$

Where:
r =The radius normalized by the blade tip radius [-]
ϕ = Inflow angle between the total and axial velocity of the blade [rad]

The result is the total duct lift coefficient, which is conveniently dependent on free stream angle of attack and thus allows for analysis in different flight conditions. However, it is also important that the distribution over the duct's circumference is obtained. At zero angle of attack this has been studied by H.Bento who compared the aerodynamic performance of a circular to square duct[29]. At it can be seen he compares the pressure coefficient in three different locations identified in Figure 3.10, and observes that the distribution is identical in both the outer and inner duct surfaces, see Figure 3.11. This however is valid for zero angle of attach, which does not correspond to the conditions to be analysed for sizing the duct as identified in Section 3.3.1.

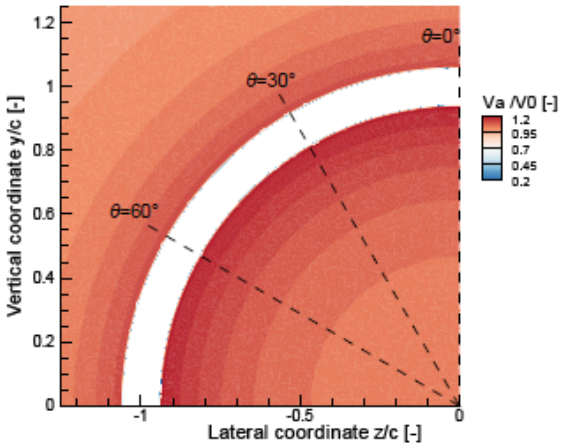

Figure 3.10: Circular duct analysed locations[29].

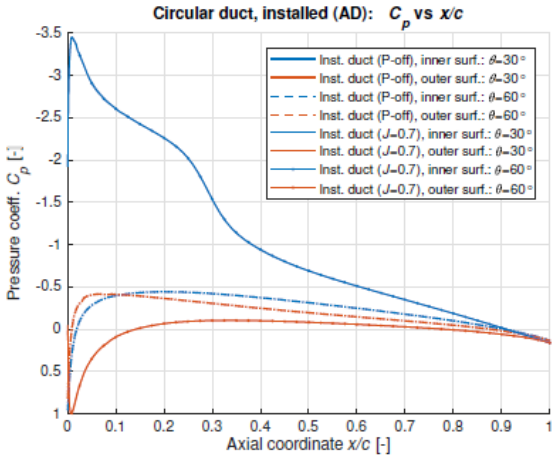

Figure 3.11: Pressure distributions at different locations[29].

For this the research carried out by T.Wan et al[59], which identifies the lift and drag distribution over the circumference in different angles of attack has been consulted. Figure 3.12 gives the lift distribution, which is used for modelling the one over the duct. Angle of attack $\alpha = 0.05rad \approx 2.9^o$ for cruise as this is considered typical and in order to obtain pressure distribution different than zero from Equation 3.19 is modelled. $\alpha = 0.15rad \approx 8.6^o$ for take-off and $\alpha = -0.15rad \approx -8.6^o$ for dive conditions have been taken as reference distributions. Those have been chosen as the closest values to the reference ATR take-off angle of attack and the corresponding negative value of it.

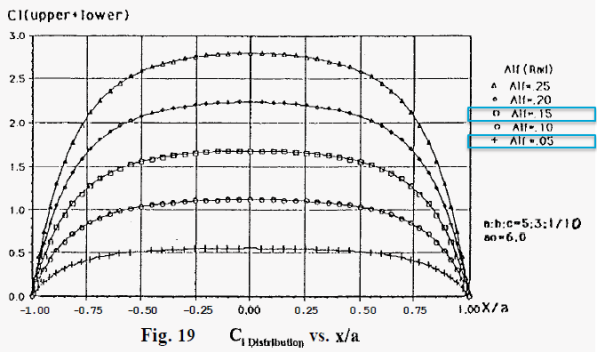

Figure 3.12: Lift distribution over the duct circumference for different angles of attack[59].

In order to make a conclusion on the upper and lower surfaces forces, a reference with biplanes has been

made, see Figures 3.13 and 3.14. It can be observed that different pressure distribution on the upper and lower surfaces is present with the lower wing generating lower pressure due to the upper one's interference. However, in order to determine those distributions for different angles of attack, a thorough research is seen necessary, which is out of scope of the current method definition. Thus, for an input distribution, it has been assumed that the upper and lower duct surfaces generate identical lift force.

Figure 3.13: Sopwith Camel in flight[60].

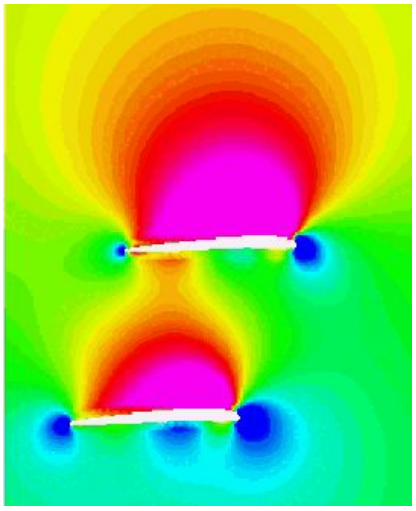

Figure 3.14: Sopwith Camel distribution[61].

However, the structural sizing method is capable of dealing with a more representative aerodynamic model and is not restricted by this assumption.

DRAG

The drag of the duct has a zero-lift and a lift-induced component. The zero-lift drag is determined using a conventional wing method proposed by Sadraey[62] and expressed by Equation 3.22.

$$C_{D_0} = C_f f_{tc} f_M \frac{S_{wet}}{S}\left(\frac{c_{d_{min}}}{0.04}\right)^{0.4} \tag{3.22}$$

Where:
$c_{d_{min}}$ = *Minimum airfol drag coefficient [-]*
C_f = *Skin friction coefficient for hydraulically flat plates, see Equation 3.23[-]*
f_M = *Mach correction, see Equation 3.25[-]*
f_{tc} = *Factor depending on airfoil thickness ratio, see Equation 3.26[-]*
S = *Total area* $[m^2]$
S_{wet} = *Wetted area* $[m^2]$

$$C_f = \begin{cases} \frac{0.455}{(log_{10}Re)^{2.58}} & \textit{for turbulent flow} \\ \frac{1.327}{\sqrt{Re}} & \textit{for laminar flow} \end{cases} \tag{3.23}$$

$$\textit{Where: } Re_{duct} = \frac{\rho V_{duct} c_{duct}}{\mu} \tag{3.24}$$

$$f_M = 1 - 0.08M^{1.45} \tag{3.25}$$

$$f_{tc} = 1.0 + 2.7\left(\frac{t}{c}\right)_{max} + 100\left(\frac{t}{c}\right)^4_{max} \tag{3.26}$$

The induced drag of the ring wing is given by Equation 3.27, where the Oswald factor $e = 2$.

$$C_{D_{i,duct}} = \frac{C_L^2}{\pi\, e\, AR} = \frac{C_L^2}{2\pi AR} \tag{3.27}$$

Summing Equation 3.22 and 3.27 gives the total duct drag. In order to determine the distribution over the circumference, the research carried out by T.Wan et al[59] was again consulted and following the same approach as the one of the lift coefficient discussed above, Figure 3.15 is used for modelling the gives the

distribution. The same angles of attack $\alpha = 0.05rad \approx 2.9^o$ for cruise, $\alpha = 0.15rad \approx 8.6^o$ for take-off and $\alpha = -0.15rad \approx -8.6^o$ for dive conditions have been taken as reference distributions.

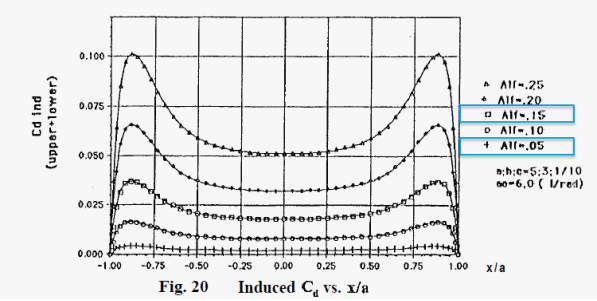

Figure 3.15: Drag distribution over the duct circumference for different angles of attack[59].

PITCHING MOMENT

Pitching moment has not been discussed by Harinarian[8], but an estimation of the centre of pressure location as presented by Werle[21]. By rearranging Equation 3.28, using the normal and tangential force definition, as given in Equation 3.29[63], to express it with respect to the lift and drag coefficients calculated above, and solving for Cm, the pitching moment coefficient is determined.

$$X_{cp} = \frac{1}{4} - \frac{C_m}{C_N} = \frac{1}{4}\left[1 - \frac{atan(1.8/AR)}{3A + atan(0.6/AR) + atan(1.2/AR) - atan(1.8/AR)}\right] \tag{3.28}$$

$$C_L = C_N cos\alpha - C_A sin\alpha$$
$$C_D = C_N sin\alpha - C_A cos\alpha \tag{3.29}$$

Where:
AR = *Aspect ratio [-]*
C_A = *Tangential force coefficient [-]*
C_N = *Normal force coefficient [-]*
α = *Angle of attack [rad]*

LIMITATIONS

A few limitations to this aerodynamic estimation should be pointed out:

1. The propeller design, depending on blade cross section, blade pitch as well as operational characteristics like take-off and cruise RPM, currently are based on reference with ATR72 and/or designed such that they produce reasonable results;
2. The aerodynamic distribution is modelled based on a reference duct. Changing the shape or the aspect ratio will influence this distribution. It is however believed that this distribution is representative to ring wings and can be used for an estimation. A more accurate distribution can be achieved from CFD analysis;
3. Aerodynamic contribution of upper and lower duct parts is expected not to be equal, with the lower part generating lower lift and therefore drag and pitching moment. If more accurate distributions for different angles of attack is required, it is recommended to obtain this from a CFD analysis.

3.3.4. NODES LOADING

Having determined the loading distribution, a way to represent this as node load in the FEM has to be defined. Figure 3.16 presents two was of representing distributed load over the beam length on the corresponding nodes as proposed by R.D.Cook[41]. It can be seen that the force on each node depends on the beam length and the distance of the force to the node. Consistent nodal loads also include moment due to moving the resultant force at the nodes whereas applying reduced nodal loads leads to no moment at the nodes.

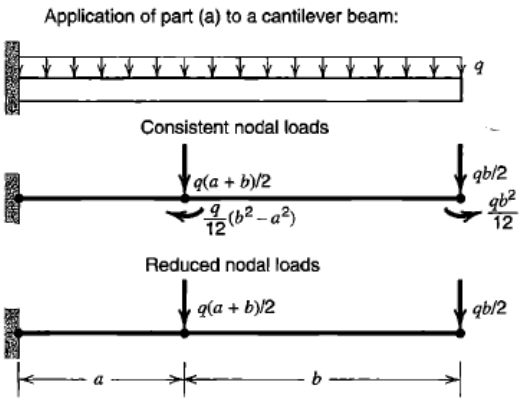

Figure 3.16: Distributed beam load to node loading[41].

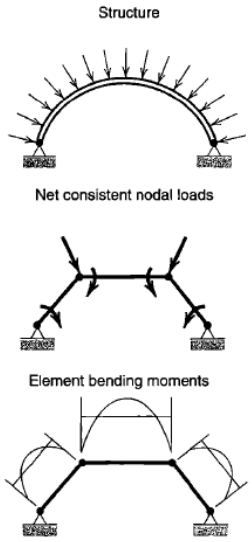

Figure 3.17: Distributed arch load to node loading[41].

Even though one would generally assume that consistent nodal load represents the structure better, Figure 3.17 proves that this is not always the case. The top nodes moments are not present in reality as the real arc's forces are cancelling out, but are still an acceptable representation. The bottom ones, however, are violating the reality more severely as no reaction moment can be present on a pin support.

Following this approach the aerodynamic load distribution is represented on the nodes in a similar way. Figure 3.18 shows that the resultant force F_r on the beam is calculated by taking the trapezoidal area. Each node influence depends on the distance to the resultant force application, with Y being the trapezoidal centroid from the base, or the bigger force. No nodes moment is applied.The same approach is taken for drag, pitch moment and beam structural load.

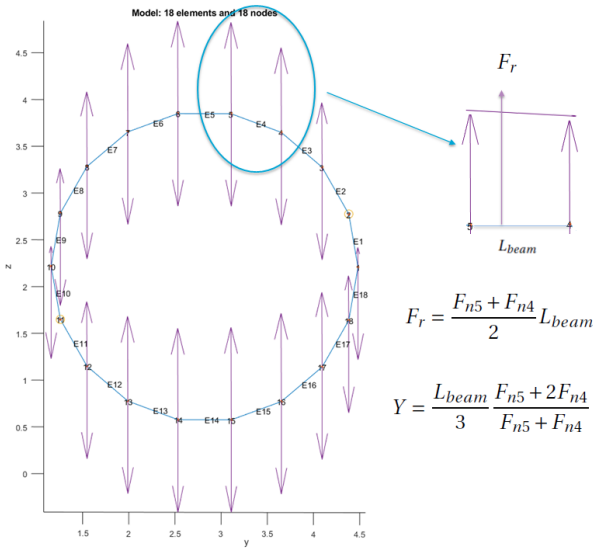

Figure 3.18: Aerodynamic loading representation on the duct FEM.

3.3.5. BLADE CONTAINMENT

Section 2.3.3 has presented the different analyses approaches to ensure a sufficient structural resilience to contain any blade segments in case of a blade loss. Keeping in mind that the DUUC has one stage compressor,

namely the propeller itself, it can be seen that it is best estimated by Goldsmith et al. with correction factor of 0.4 and by the original Fedortschenko method relations.

Due to the fact that the latter makes extensive use of empirically derived coefficient on which there is no information and thus possibility to tailor them, it is not seen suitable for sizing the innovative DUUC's ducts. Thus, it is concluded that Goldsmith offers a more robust and applicable solution to the problem at hand. Furthermore, as the correction factors suggested in this study have also been derived empirically, basing their information on conventional casing designs, it has been decided that those are not applicable to the analysis at hand and the original Goldsmith will be used.

3.4. PYLON SIZING

Figure 3.3 represents the pylon Catia model, where the airfoil shape and stringers can be seen. This section will cover the method used to size the pylon by first presenting on the critical load cases in Section 3.4.1. This will be followed by modelling representation in Section 3.4.2. Section 3.4.4 elaborates on the aerodynamic and discrete pylon loads. Lastly, Section 3.4.4 defines the method to analyse the structure in blade loss conditions.

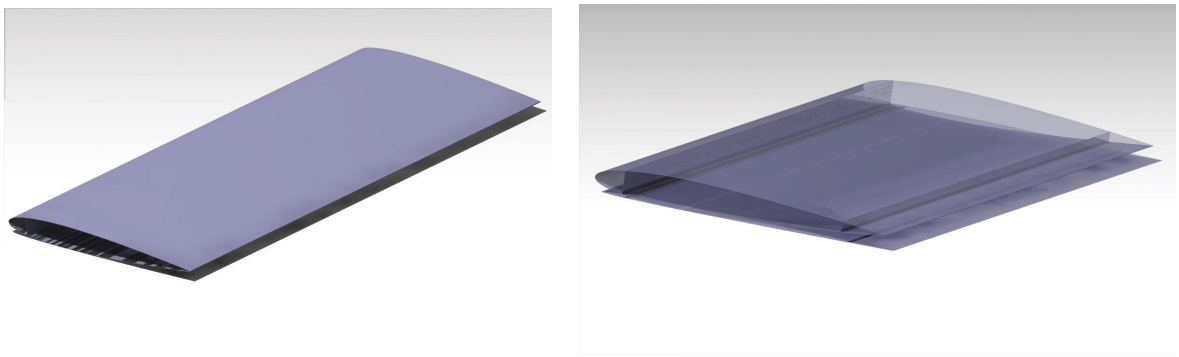

Figure 3.19: Pylon Catia model.

Table 3.2 lists the required inputs for the method at hand.

Parameter	Defined by module	Dependent on
Length	Design choice	Propeller design*
Airfoil	Geometry definition	Design choice
Pylon installation angle	Constant	Propeller design*
Number of beams	Variable	Design choice
Material		Design choice
Aerodynamic loads		Discussed in Section 3.4.4
Engine mass	Geometry definition	Many
Duct mass	Class 2.5 duct sizing method	Discussed in Section 3.3
Blade geometry	Geometry definition	Propeller design*

Table 3.2: Required method inputs.

* Please note that the engine and propeller design suitable for this concept have not been defined yet. As this design will affect severely the analysis, it is recommended that the corresponding parameters will be defined with more accuracy.

3.4.1. CRITICAL LOAD CASES

Largest loads on the pylons in normal operations are typically observed at take-off with the engine being in full thrust settings. Highest dynamic pressure on lifting surfaces is experienced at maximum speed, assumed to be dive speed. Next to this, crash landing is a condition which is expected to result in largest pylon root bending moment, due to the high duct and engine mass located at the tip, and therefore will be also studied. Last but not least, as discussed by I.Armendáriz et al.[49], the pylon needs ensure that excessive vibrations

will not be transmitted to surrounding structure as those could be detrimental. This is also a requirement defined by EASA, see Appendix A Section A.3.

Thus, the critical load cases that will be considered for the design are:

(1) Take-off with the engine at full thrust, as discussed in Appendix A, Section A.3, where also a safety factor of 1.6 applicable to turbo-propeller engines will be applied;

(2) Diving conditions, when maximum speed and therefore dynamic pressure on the pylon is expected next to alignment of the weight and component of the lift. The design dive speed will be calculated using guidance in Appendix A, Section A.1;

(3) Crash landing conditions with a safety factor of 1.33 as discussed in Appendix A, Section A.1;

(4) Propeller blade loss failure as discussed in Appendix A, Section A.3, where a conservative safety factor of 1.25 will be applied.

It can be seen that the listed load cases (1)-(3) are primary looking into static loading typically resulting in high bending stresses and shear loads. Torque is not expecting to be limiting load due to the short pylon external part and the remaining supported by the duct. Furthermore, focussing on static loading is based on the primary function of the pylons as attachment of the propulsion system that includes the engines and ducts. Those are located at the pylons' tips and have significant weight that is expected to contribute for high pylon loading.

3.4.2. MODELLING AND STATIC STRESS CALCULATION

Figure 3.20 represents the pylon model as defined for the Finite Elements Analysis. It can be seen that 21 nodes, thus 20 beams, have been defined. A range of numbers of beams have been run to see if that would affect the analysis. It was observed that no noticeable computational time increase nor change in structural mass was present.

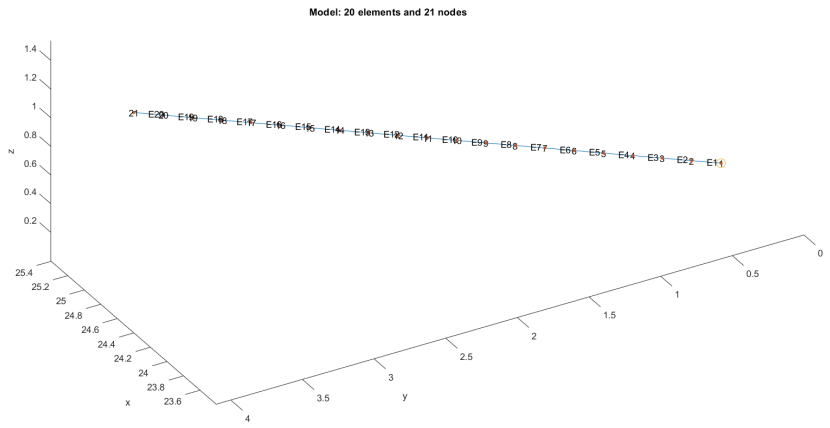

Figure 3.20: Pylon FEM model.

Following the same procedure as the one presented in the duct discussion, the equilibrium equations as defined in Equation 3.1 are set and solved to get the deformations. The beam loads are then obtained using Equations 3.2. The stiffness matrix is also defined using the three dimensional beam definition given by Cook[41] and discussed in Section 3.3.2.

One thing that is different from the duct is that the pylon structure is simplified using method proposed by T.H.G.Megson[42] who introduces the "boom idealization", that represents the structure as number of point masses. An example discretization of a typical wing section with skin, stringers and spars is illustrated in Figure 3.21.

Some assumptions in this simplifications are made, such as neglecting the variation of stress over the cross-section of a stringer due to shear, bending or torsion, as it is assumed to be small compared to overall variation of stress on the cross section. In addition to this, the distance between wing skin and stringer centroids is also neglected, which allows for replacing the actual geometries of stringers and spars by concentrated areas called booms. The stress over those is constant and their centroid is located along the skin. In typical

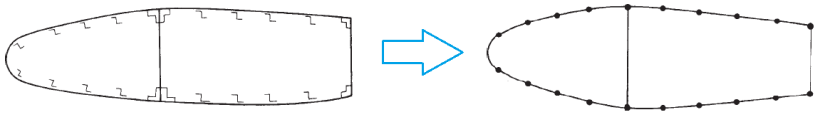

Figure 3.21: Discretization of typical wing section[42].

aircraft wing and fuselage sections the direct stresses are mainly carried by the stringers and spar flanges. Even though the skins typically support part of this load as well, they are often assumed to carry shear loads only. If all the direct stresses are contained in the booms, their areas can be sized accordingly to meet the applied load.

Figure 3.22 illustrates the idealization of panel with booms carrying all the direct stresses and the skin supporting shear only. The corresponding boom areas are calculated by Equation 3.30, which is also used for the moment of inertia expression as given in Equation 3.31 with x and y being the distance to the cross sectional centroid.

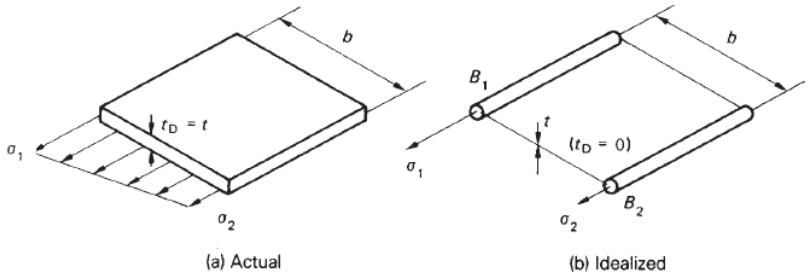

Figure 3.22: Panel idealization[42].

$$B_n = \frac{t_D b}{6}\left(2 + \frac{\sigma_{n+1}}{\sigma_n}\right) \tag{3.30}$$

$$\begin{aligned} I_{xx} &= B_n y^2 \\ I_{yy} &= B_n x^2 \\ I_{xy} &= B_n x \cdot y \end{aligned} \tag{3.31}$$

The neutral axis' location is calculated through the condition that any resulting load on the cross section is zero, see Equation 3.32.

$$\int_A \sigma_z dA = 0 \tag{3.32}$$

Idealizing the structure always has some effect on the analysis. As bending is assumed to be carried by the stringers, which coincide with the booms, it is not impacted.

Looking into the shear flow expressed in Equation 3.33, however, it is observed that the shear stress in the skin between booms is assumed constant and equals the average of shear flow parabolically distributed in the non-idealized section. Thus, the actual distribution is lost.

$$q_s = -\left(\frac{S_x I_{xx} - S_y I_{xy}}{I_{xx} I_{yy} - I_{xy}^2}\right)\left(\int_o^s t x ds + \sum_{r=1}^{n} B_r x_r\right) - \left(\frac{S_y I_{yy} - S_x I_{xy}}{I_{xx} I_{yy} - I_{xy}^2}\right)\left(\int_o^s t y ds + \sum_{r=1}^{n} B_r y_r\right) + q_{s,0} \tag{3.33}$$

Where:
B_r = *Boom area calculated using Equation 3.30* $[m^2]$
I_{xx} = *Second moment of inertia around the x-axis* $[m^4]$
I_{xy} = *Product second moment of inertia around the y-axis* $[m^4]$
I_{yy} = *Second moment of inertia around the y-axis* $[m^4]$
S_x = *Shear for in x-direction* $[N]$
S_y = *Shear for in y-direction* $[N]$
x = *Horizontal location of calculation point with respect to the neutral axis* $[m]$
y = *Vertical location of calculation point with respect to the neutral axis* $[m]$

If any of the skin, stringers or booms stresses is found to be higher than the allowable one, the respective thickness or area is increased by a factor corresponding to and the analysis is rerun. This is repeated until the whole structure is capable of carrying the corresponding loads.

3.4.3. VIBRATION ANALYSIS

The vibration loads in blade loss conditions and their impact on the engine mounting system have been thoroughly discussed in Section 2.3.3. It has however been realised that the approach proposed by I.Armendáriz et al. and documented in [50],[49],[51] is too detailed for a conceptual design stage. Therefore, it has been decided that the structure will be sized statically with the method discussed above and a check of the impact on the pylon structure will be done by running steady state analysis using Abaqus[66] with the structure as outputted from the static stress sizing.

In order to model it, the pylon Catia part, with the stringers attached, has been created and inputted in the FEM tool. Note that the analysis should include the booms, which are more a sizing tool than actual physical structure. In order to represent those, the stringers thickness has been defined such that the resulting area is the same as the boom one.

Please remember that the requirements on the enine mounting system also state that no excessive vibrations should reach the surrounding airframe so that the aircraft integrity is not sabotaged. In practice this is achieved by the installation of additional dampers system, see an example in Figures 3.23 and 3.24. However, this system is considered as part of detailed analysis and is therefore out of scope of the research at hand.

Figure 3.23: Reference dampers used on MD11 - fuselage part.

Figure 3.24: Reference dampers used on MD11 - engine part.

3.4.4. PYLON LOADING

This section elaborates on the loads present on the pylon, starting with aerodynamic loads estimation and then followed by sicrete loading representation.

AERODYNAMIC LOADS

The pylon is represented as a straight wing with $NACA0012$ airfoil being its cross section. As it is discussed by Harinarian[8], being clamped to the fuselage on the one end and the duct on the other, it can be represented as an infinite wing under an angle of attach equal to its dihedral. The aerodynamic load for the different critical cases are then obtained by AVL, another program developed by Massachusetts Institute of Technology[64]. The obtained aerodynamic distribution is applied to the pylon structure and the node loads are estimated following the procedure outlined by Cook[41] and discussed in Section 3.3.4.

DISCRETE LOADS

The discrete loads on the pylon are introduced by the engine and the duct. Engine's contribution to the load is added as point loads located at its attachment. In flow-direction load comes from its thrust and the mass is aligned with the gravity vector. Furthermore, at the ducts two point attachment its mass and aerodynamic loads are applied.

VIBRATION LOADS

The loads to be used for the vibrational analysis are defined using Equation 2.21, where the F_c is the blade centripetal force expressed by $m_{bladeEl} \cdot R\omega^2$. M_{oop} is the moment introduced on the structure due to the presence of this force. In order to represent the most critical condition, it has been assumed that a complete blade separation is experienced at take-off thrust conditions. Those cause extreme loading and therefore deformations on the pylon, which will be further discussed in Section 4.2.2.

4

Results and Method Analysis

This chapter presents the results obtained by the structural analysis method as presented in Chapter 3. Firstly the duct results will be discussed in Section 4.1. Section 4.2 then presents the pylon results. Please note that the this section will elaborate in the corresponding loadings and resulting deformations as well as some design choices made. The final components weight results will be summarised in Chapter 5 Table 5.1.

4.1. Duct

This section will present and discuss the results obtained with the duct sizing method as defined in Section 3.3. Firstly, the static stress sizing results will be shown in Section 4.1.1. This is followed by the model verification in Section 4.1.2. Section 4.1.3 then studies if the model is sensitive to design changes, such as an increase in load.

4.1.1. Static Sizing Results

This section presents the results for the three critical duct load cases identified in Section 3.3.1. In order to represent the corresponding loading in those conditions, the main inputs are the velocity and revolutions per minute of the engine, which serve as inputs to the XROTOR as discussed in Section 3.3.3. Table 4.1 lists the corresponding conditions and settings as well as the resulting advance ratios. The cruise altitude is a requirement following ATR performance and the engine take-off operating capabilities give the take-off RPM. 82% of this is taken during cruise[65]. The resulting advance ratios, given in column J, are calculated after the velocities have been corrected using the continuity equation, following the procedure in Section 3.3.3.

Load Case	Altitude [m]	Speed [m/s]	RPM	J [-]
Take-off	0	56.2	1500	0.79
Cruise	7000	140.5	1230	2.15
Dive	7000	193.2	1230	2.30

Table 4.1: Operational conditions at each load case.

Load Case	CT	CP	$T_{c_{PropCb}}$	k
Take-off	0.1211	0.1222	0.5662	0.1505
Cruise	0.0275	0.1881	0.0180	0.0268
Dive	-0.0726	-0.1133	0.1807	0.0850

Table 4.2: XROTOR and DFDC outputs.

Table 4.2 then gives the relevant intermediate XROTOR and DFDC results are given. It can be seen that in take-off the propeller provides highest thrust coefficient and in cruise - highest power coefficient. Due to the extreme conditions in dive however, there is negative contribution to thrust and power. Please note that those are just used for inputs to obtain reasonable aerodynamic loads and are in no means to be taken for propeller performance estimation. The latter is still not been determined and depends severely on blade design (such as shape and blade pitch) and real operating settings. Just for reference, the blade airfoil used in this case is

$NACA6412$ and blade pitch for the three different cases are 45^o, 25^o, 45^o, which were chosen by such that they provide reasonable loading at the redefined conditions.

Using the DFDC and following the procedure listed in Section 3.3.3, the corresponding aerodynamic coefficients are obtained, see Table 4.3. It is clearly visible that in power on the lift polar C_{L_α} is significantly increased, which naturally leads to higher lift coefficient and thus drag. The given pitch moment is the one obtained at power off conditions abut the airfoil aerodynamic centre. The pitch moment distribution is obtained using Equation 3.28.

Load Case	$C_{L_{\alpha_{duct_{POff}}}}$	$C_{L_{duct_{POff}}}$	$C_{L_{\alpha_{duct_{POn}}}}$	$C_{L_{duct_{POn}}}$	$C_{D_{duct_{POff}}}$	$C_{D_{duct_{POn}}}$	$C_{m_{duct}}$
Take-off	4.9706	0.6940	5.7186	0.7985	0.0376	0.0498	0.00265
Cruise	5.2778	0.2303	5.4194	0.2365	0.0053	0.0055	-0.00202
Dive	5.3284	-0.7439	5.7815	-0.8072	0.0466	0.0542	-0.00408

Table 4.3: Aerodynamic coefficient for different load cases.
Where:$POff$ = Power Off , POn = Power On

Figure 4.1 illustrates the loading at cruise conditions on the carbon-fibre-reinforced polymer duct where the lift force is pointing in positive z direction and the weight is aligned with gravity vector, or negative z direction. The drag contribution is present in negative x direction, which gives a small angle of the lift force.

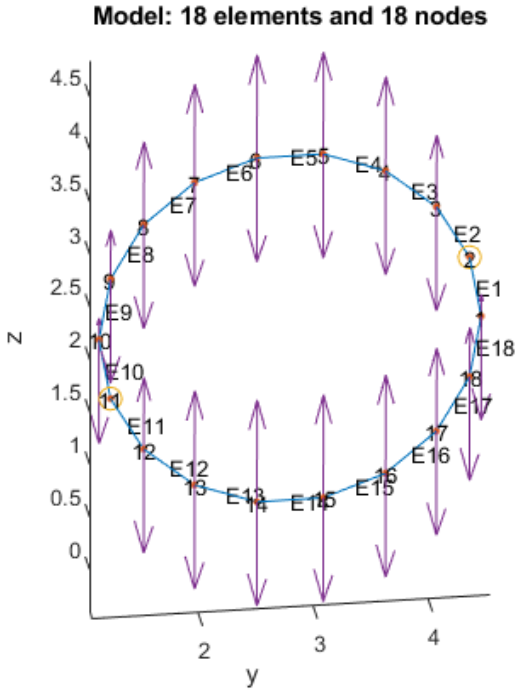

Figure 4.1: Duct FEM loading in cruise conditions.

Consequently, Figures 4.2 and 4.3 present the resulting deformations, for the CFRP and aluminium duct solutions. It can be seen that, as the aerodynamic loading is higher than the structural one, the deformations are also in the positive z direction and the clamped locations are clearly visible as the beams related to those have not changed their end locations. Please note that the deformations presentation are exaggerated for clearer visualisation.

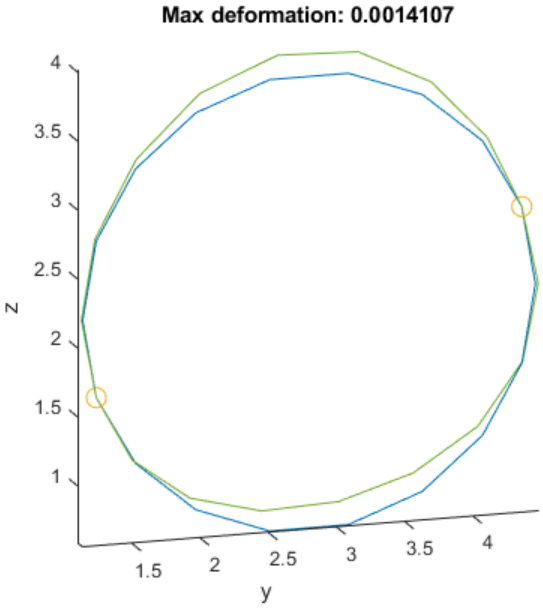

Figure 4.2: CFRP duct deformations in cruise conditions.

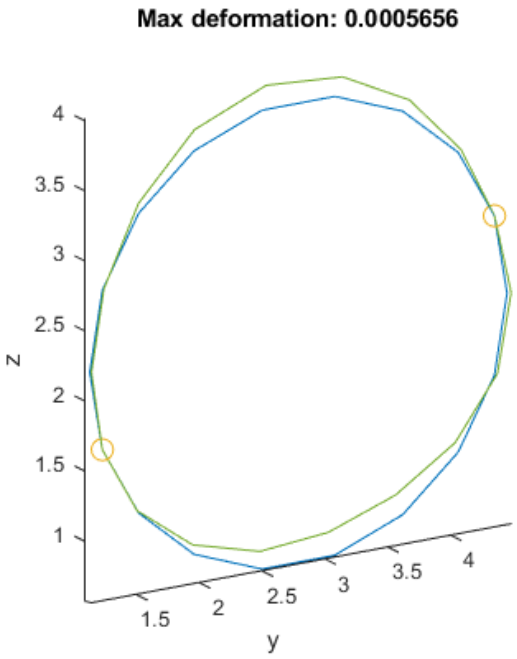

Figure 4.3: Aluminium duct deformations in cruise conditions.

Following is the analysis of take-off conditions with Figure 4.4 presenting the loading on the duct where the lift force is again pointing in positive z direction and the weight is aligned with gravity vector. I can be observed that naturally, the lift on the duct is higher due to the higher engine thrust required. The drag contribution is again present in negative x direction, which gives a small angle of the lift force. Figures 4.5 and 4.6 then presents the resulting deformations for the carbon-fibre-reinforced polymer and aluminium duct respectively, both of which are higher than the ones in cruise conditions, due to the higher aerodynamic loading.

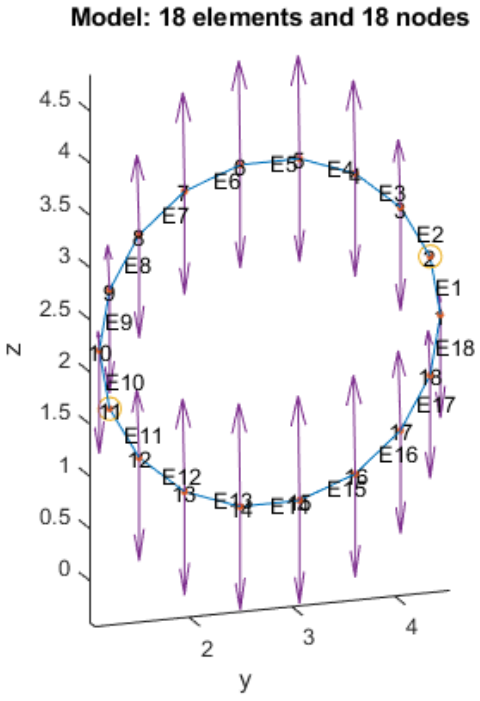

Figure 4.4: Duct FEM loading in take-off conditions.

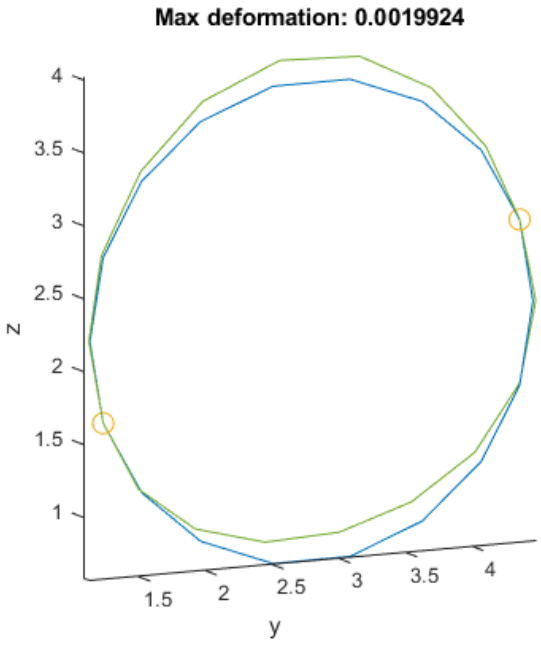

Figure 4.5: CFRP duct deformations in take-off conditions.

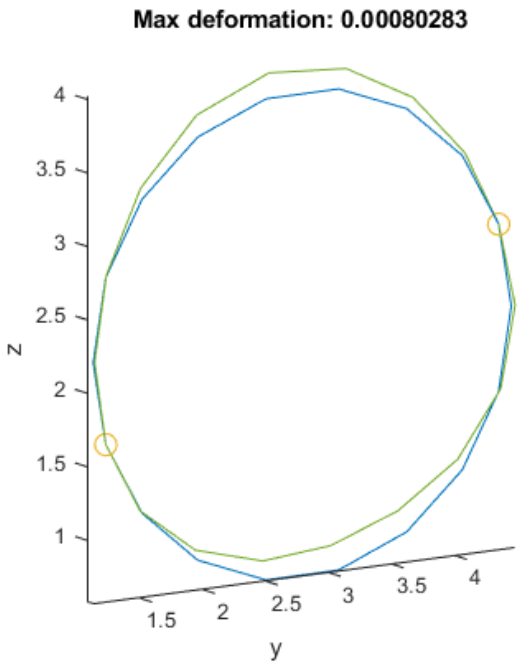

Figure 4.6: Aluminium duct deformations in take-off conditions.

Last is the analysis in dive conditions, where maximum dynamic pressure is present on the structure. This naturally result in highest aerodynamic loading, which in dive conditions is aligned with the weight vector, see Figure 4.7, and thus results in highest structural load. Figures 4.8 and 4.9 then present the resulting deformations that contrary to the above mentioned ones are in the negative z-direction and are highest from the three conditions.

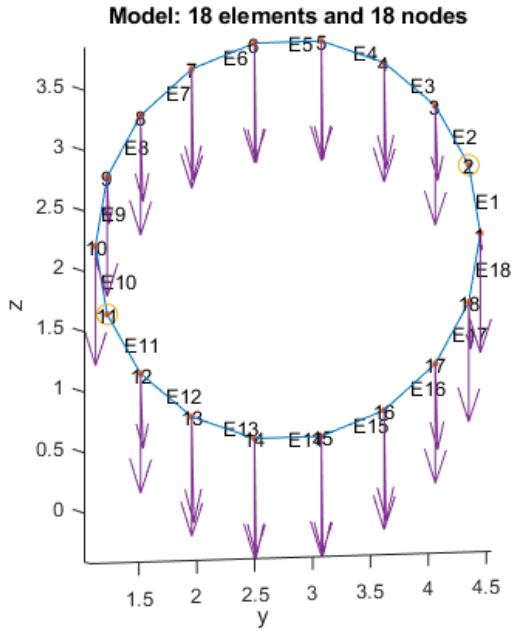

Figure 4.7: Duct FEM loading in dive conditions.

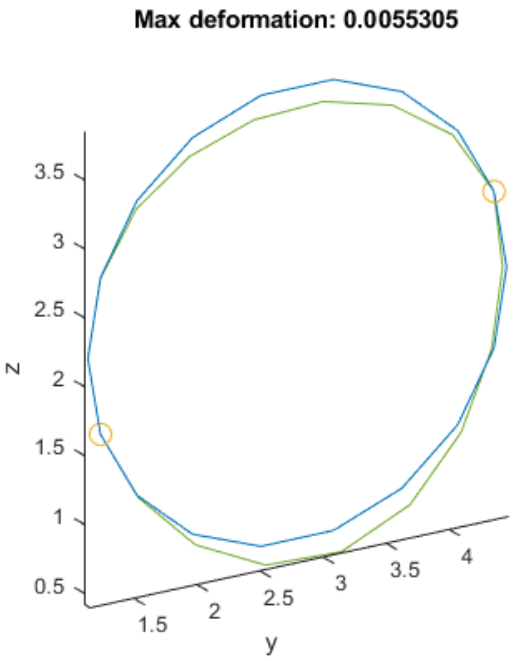

Figure 4.8: CFRP duct deformations in dive conditions.

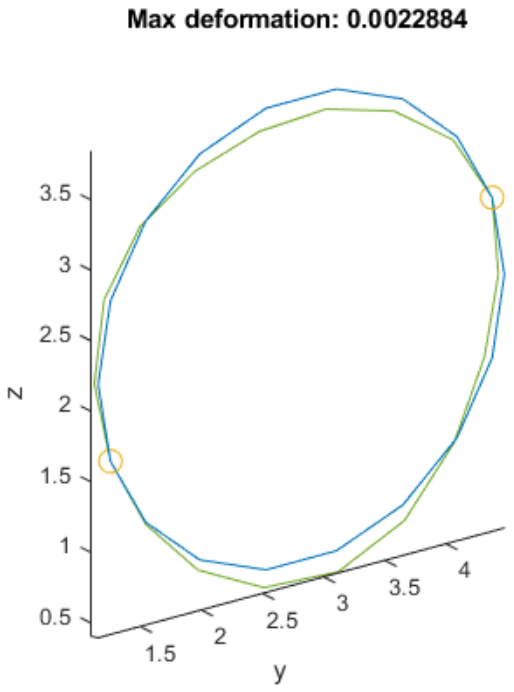

Figure 4.9: Aluminium duct deformations in dive conditions.

4.1.2. VALIDATION

Having defined a new simplified model, a verification of its performance needs to be carried out. For this purposed, a CAT part was created, see Figure 3.3, and input in Abaqus[66] with structural and aerodynamic forces included. Figure 4.10 presents the corresponding mesh with number of elements limited to <1000, due to the use of the student edition Abaqus. Figure 4.11 then shows the fixed nodes, which are in alignment with the Matlab FEM model presented in Figure 3.4. The gravitational and aerodynamic loading application in seen in Figures 4.12 and 4.13. It should be noted that uniform aerodynamic load is used for the verification in both Matlab and Abaqus.

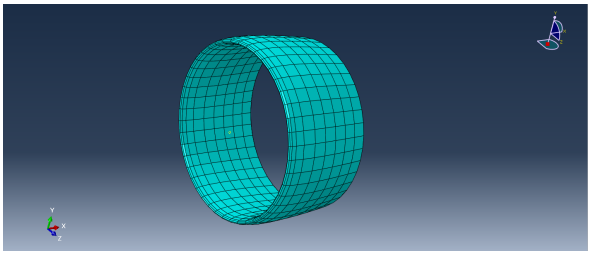

Figure 4.10: Duct Abaqus mesh.

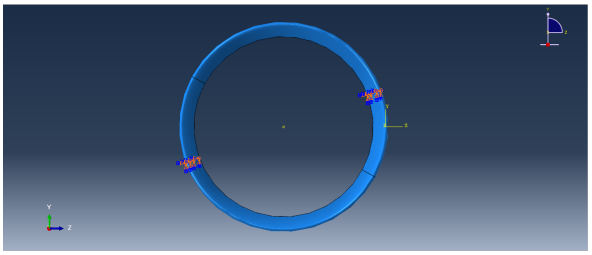

Figure 4.11: Duct Abaqus fixed nodes.

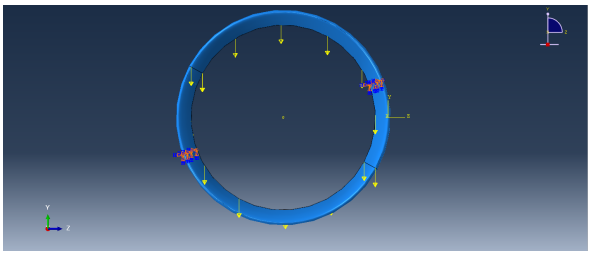

Figure 4.12: Duct Abaqus gravity load.

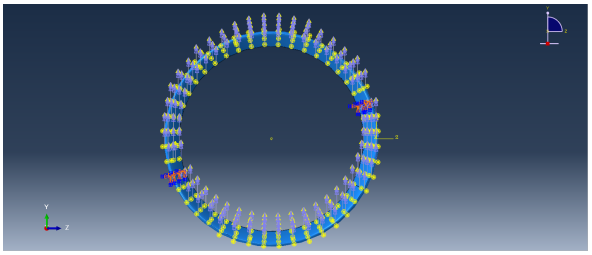

Figure 4.13: Duct Abaqus aerodynamic load.

Figures 4.14 and 4.15 give the deformations obtained under the specified loading with Abaqus and Matlab

respectively. It can be seen that the two behave in very similar way with the structure deforming in the direction of the weight vector. This is different from previous cases, as in Figures **??** and **??**, because the applied lift force is much smaller than the one in previous runs, but the structure cannot be lighter due to the material thickness limitation of 1mm applied. Thus this results in higher structural than aerodynamic loading. The order of magnitude of the two displacements is also similar with Matlab giving 3.85E-2mm and Abaqus results of 9.99E-3≈ 1E-2mm. The differences are attributed to the different discretization techniques in the two models with Abaqus having the a number of elements spanwise, when the Matlab model represents it as a single skin, which allows for deformation variation spanwise. Roughly at the highest airfoil thickness is the highest displacement observed. Furthermore, in order to simplify the analysis, the moment of inertia in the Matlab model, as represented in Figure 3.6, is not an exact airfoil, but is considered close approximation.

Figures 4.16 and 4.17 then show the two models loaded with the aerodynamic forces only, which naturally changes the deformations to align with the positive z direction. Here again the orders of magnitudes are very close with Abaqus giving deformation of 5.695E-3mm and Matlab showing 6.495E-2mm. It can be seen that the model overpredicts the deformation due to the aerodynamic loading which is attributed to the lower moment of inertia. The results in the verification are in good agreement and therefore the model is considered consistent.

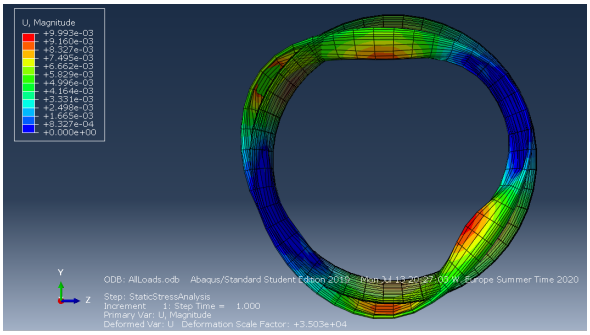

Figure 4.14: Duct deformations in Abaqus with aerodynamic and gravity forces applied for verification.

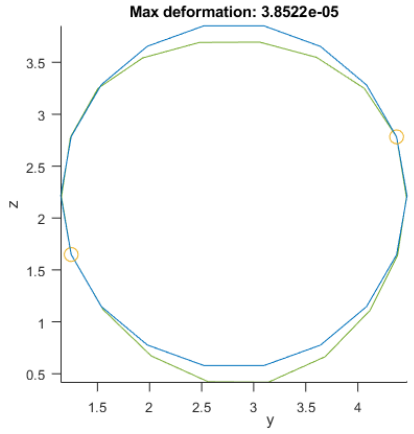

Figure 4.15: Duct Matlab FEM deformations with aerodynamic and gravity forces applied for verification.

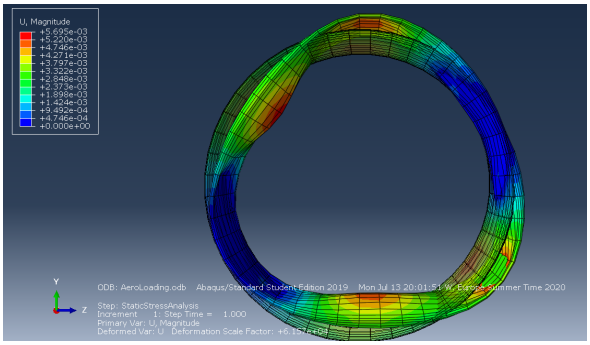

Figure 4.16: Duct deformations in Abaqus with only aerodynamic loads applied for verification.

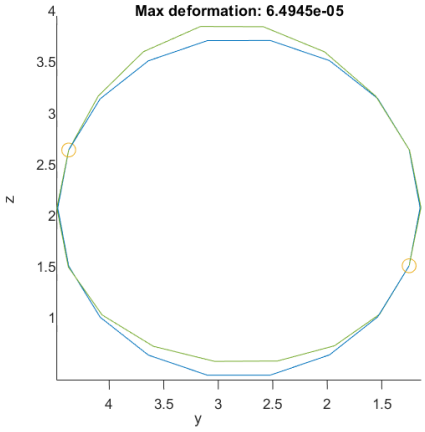

Figure 4.17: Duct Matlab FEM deformations with only aerodynamic loads applied for verification.

4.1.3. DESIGN SENSITIVITY

Next to being more accurate than the Class 2 wight sizing methods, another requirement on the method is to be design-sensitive such that, if design and/or load changes are made, the method will be able to predict the structural weight, see the objective in Section 1.2.

Firstly, it should be noted that loading of any type, discrete or distributed, can be added to the method. This might be necessary if a control surface redesign is opt for, where the surfaces are actually integrated in the duct surface. Naturally, this will change the beam moment of inertia, by shortening the duct chord, and will impose certain forces and moments. In order to incorporate those, their effect at the duct airfoil aerodynamic centre needs to be identified and modelled. If correctly implemented, th structural response and thus weight change will be visible. This check, however, is challenging to carry out without example loads thus no further elaboration will be proposed.

To monitor the robustness and flexibility of the method to design changes, 10 times higher aerodynamic loading is applied and the analysis is run again. The resulting loading for the two very different loading, namely cruise and dive, are observed on Figures 4.18 and 4.19 respectively. By means of vectors it is illustrated how the structural load is much smaller than the aerodynamic one now and the different beams have different weight vector, positioned at the corresponding nodes, which is proportional to the load they carry.

Figures 4.20 and 4.21 then show the deformations obtained at 10 times cruise condition loading. Having higher toughness, the carbon-fibre-reinforced polymer is capable to sustain higher deflections than the aluminium one, which is also observed in the deflections at dive conditions shown in Figures 4.22 and 4.23.

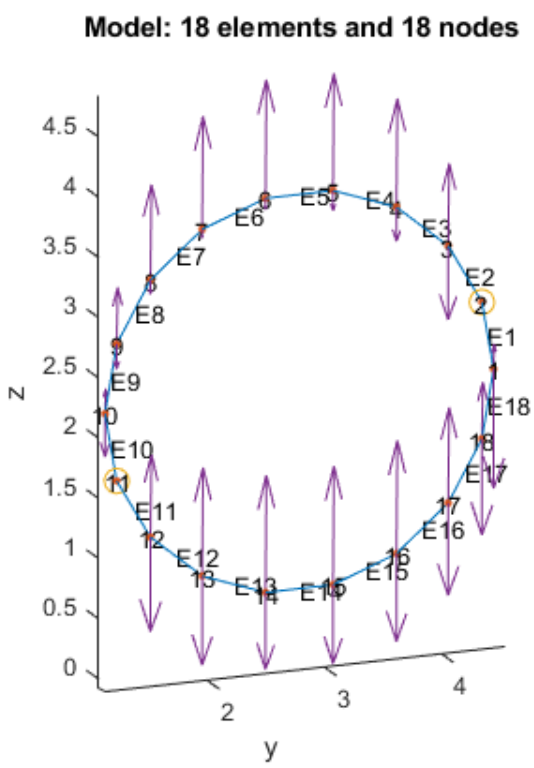

Figure 4.18: Duct FEM loading in cruise conditions with 10 times the design aerodynamic load applied.

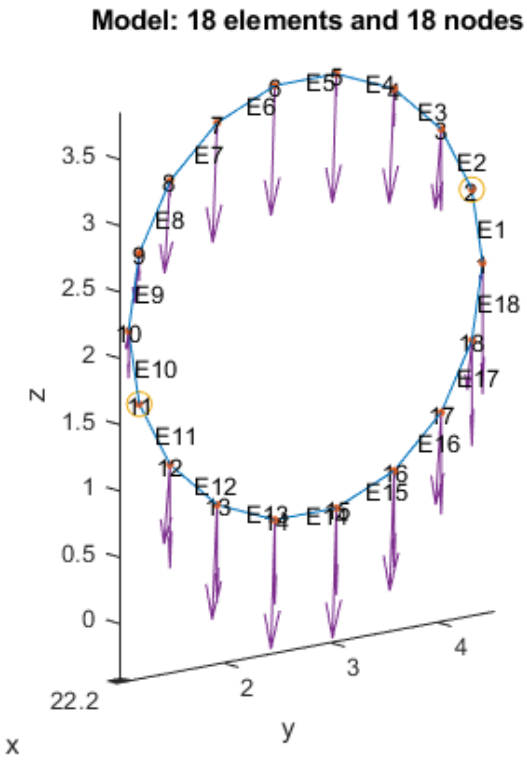

Figure 4.19: Duct FEM loading in dive conditions with 10 times the design aerodynamic load applied.

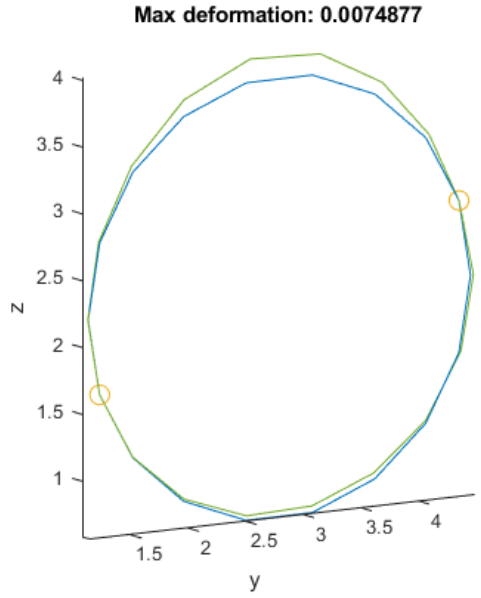

Figure 4.20: CFRP duct deformations in cruise conditions with 10 times the design aerodynamic load applied.

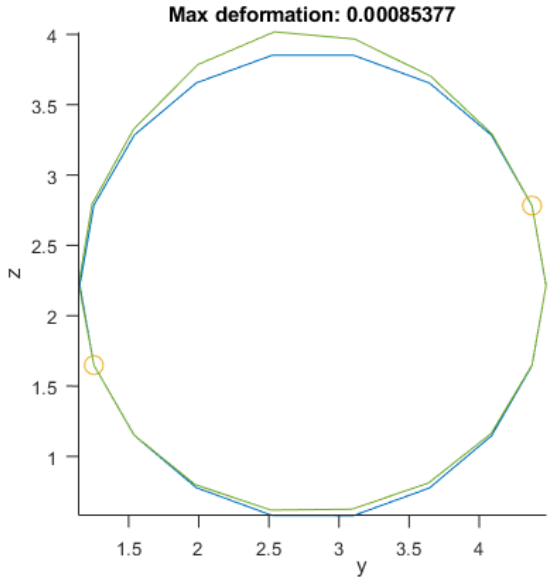

Figure 4.21: Aluminium duct deformations in cruise conditions with 10 times the design aerodynamic load applied.

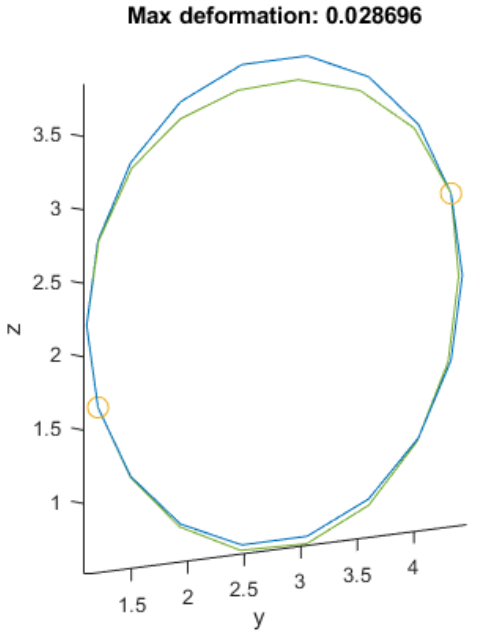

Figure 4.22: CFRP duct deformations in dive conditions with 10 times the design aerodynamic load applied.

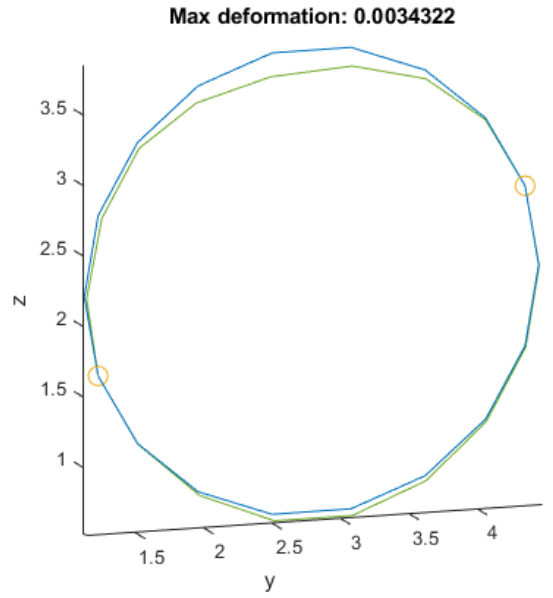

Figure 4.23: Aluminium duct deformations in dive conditions with 10 times the design aerodynamic load applied.

The two solutions also show big difference in the corresponding weights with CFRP duct being 345.2kg and the aluminium solution resulting in almost 5 times heavier structure. This extreme difference in weight is explained by the fact that aluminium cannot carry as high load as CFRP for the same thickness. At the same time, aluminium has higher density that CFRP, thus more material results in much higher mass, which also has to be carried by the structure. When this weight is also aligned with the aerodynamic loading, like in the sizing dive case, the impact on the structure is even bigger.

Iteration	Mass [kg]	Deviations
1	60.7	14
2	79.1	20
3	122.5	37
4	345.2	0

Table 4.4: Mass and number of reserve factors <1 for CFRP duct with 10 times the design aerodynamic load applied.

Iteration	Mass [kg]	Deviations
1	105.6	38
2	370.4	51
3	1400.6	10
4	1712.9	0

Table 4.5: Mass and number of reserve factors <1 for aluminium duct with 10 times the design aerodynamic load applied.

In such cases, the natural design choice would be the CFRP duct. However, if the aerodynamic performance is compromised too much, additional weight needs to be added to decrease structural deformations. It is however difficult to make those decisions on conceptual design level and thus for the time being it is shown that the method is capable of handling material changes as well, giving greater design freedom.

4.2. PYLON

This section presents the sizing analysis of the pylon. Firstly, the static loading sizing will be discussed in Section 4.2.1 followed by vibration analysis in Section 4.2.2.

4.2.1. STATIC SIZING RESULTS

This section presents the results obtained from the pylon structural sizing module for the four critical load cases defined in Section 3.4.1. As mentioned before, the aerodynamic loads are obtained by inputting the geometry and operational conditions, such as Mach number, calculated using the relevant airspeed and atmospheric conditions as listed in Table 4.1, and airfoil lift coefficients in AVL[64]. Figure 4.24 shows the input geometry with the main wing, pylon and equivalent duct surface modelled. The corresponding aerodynamic coefficients are given in Table 4.6. It should be noted that take-off, landing impact and blade loss have been analysed in maximum take-off wight pull up conditions, which is considered to be the most severe way to represent the loading with highest aerodynamic forces needed.

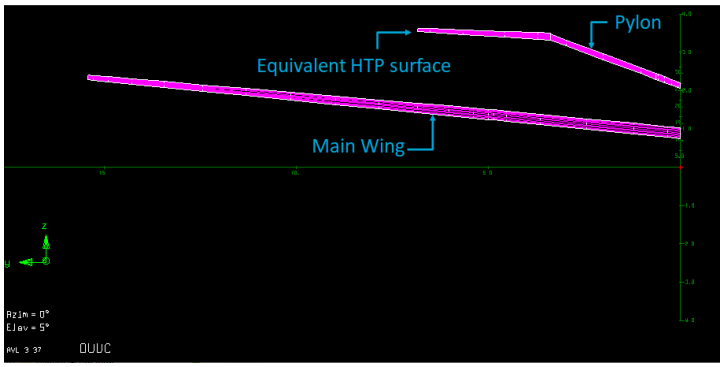

Figure 4.24: Input geometry for pylon AVL analysis.

Load type	C_L	C_D	C_m
MTOW pull-up	0.0158	0.0016	-0.0566
Dive	-0.0505	0.00608	0.1795

Table 4.6: Aerodynamic coefficients obtained using AVL and used for loading the pylon in different load cases during for sizing.

Figure 4.25 shows the loading on the pylon in take-off conditions with the aerodynamic loading represented by the lift aligned with the $+z$ direction. The weight and drag contribution are represented by the vectors pointing in $-x-z$ direction. Two vectors in the $+z$ direction are also visible which represent the aerodynamic forces of the duct with its weight being subtracted.

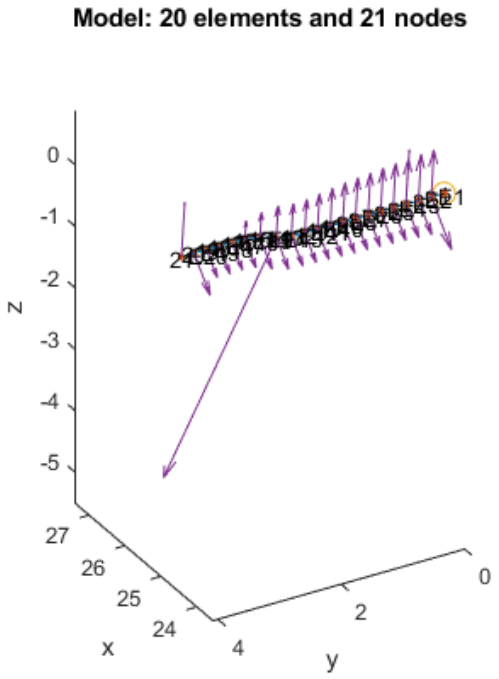

Figure 4.25: Pylon FEM loading in take-off conditions.

As it can be seen on Figure 4.26, high deformations of 0.3m are present in the flow direction caused by the high engine thrust force. Furthermore, deformations in $-z$ direction gradually increase spanwise due to the higher structural load from engine and duct mass reaching -0.2m at the pylon's tip. Next to it the pylon response to the loading if it were made out of aluminium is represented in Figure 4.27, where the deformations are much smaller and result in maximum of 9.3cm. This difference is explained by the fact that the carbon-fibre-reinforced polymer has much higher strength and can thus sustain much higher deflections. This has been also observed in transport aviation recently, where composite wings show much higher deflections than aluminium ones. It is not expected that the duct nor pylon aerodynamic performance will be influenced by this deflection, but if this is the case, aluminium structure is recommended or a CFRP one with higher thickness. Both solutions will have a weight penalty in order to decrease the resulting deflections.

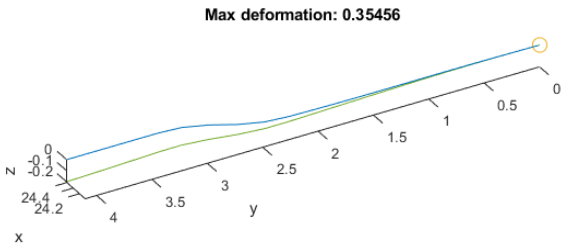

Figure 4.26: CFRP Pylon deformations in take-off conditions.

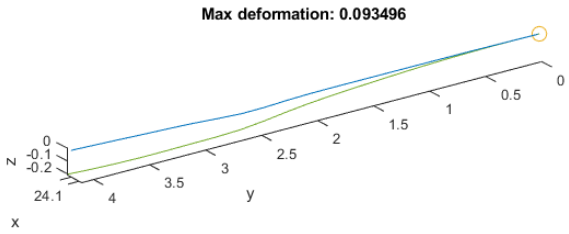

Figure 4.27: Aluminium pylon deformations in take-off conditions.

Similar behaviour is observed in hard-landing conditions with loading presented in Figures 4.28 and corresponding deformations in Figure 4.29 and 4.30. Engine thrust again causes high dislocations in the flow direction and heavy landing loads lead to tip deflections. Those however are not excessively higher than the ones observed at take-off conditions, which would have been expected if the pylon and duct aerodynamic forces were not considered. Neither of those however cause problems with ground clearance and thus are considered safe solutions.

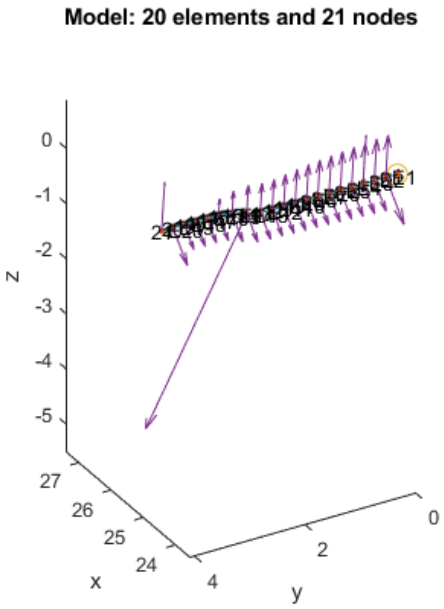

Figure 4.28: Pylon FEM loading in hard landing conditions.

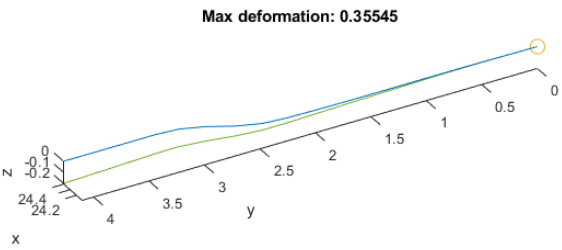

Figure 4.29: CFRP pylon FEM deformations in hard landing conditions.

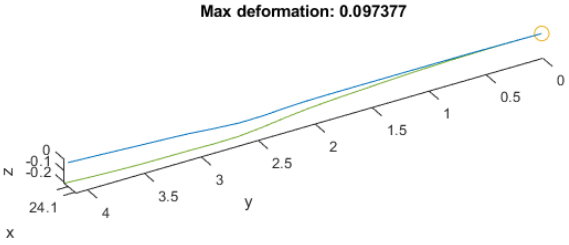

Figure 4.30: Aluminium pylon deformations in hard landing conditions.

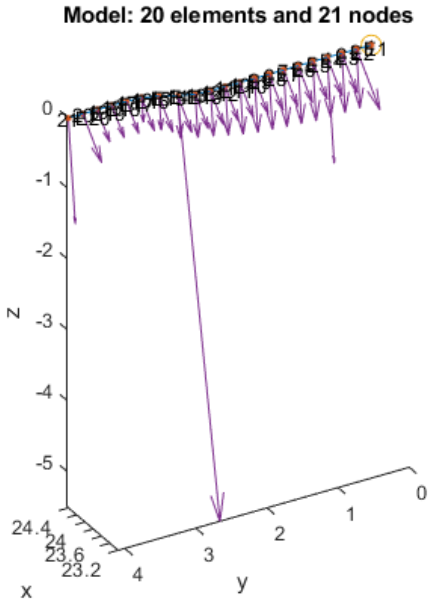

Figure 4.31: Pylon FEM loading in dive conditions.

Following is the analysis in dive conditions, which lead to the loading represented in Figure 4.31. Highest dynamic pressure and all forces directed in $-z$ direction naturally lead to highest deformations with the difference between the CFRP and aluminium solutions being very high.

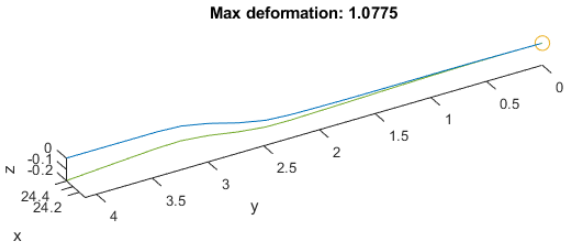

Figure 4.32: CFRP pylon FEM deformations in dive conditions.

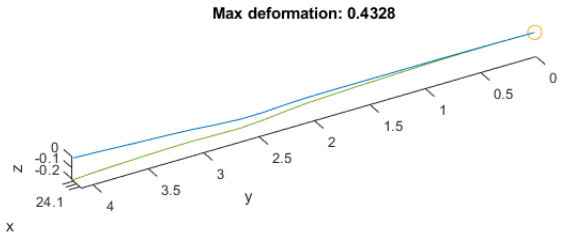

Figure 4.33: Aluminium pylon deformations in dive conditions.

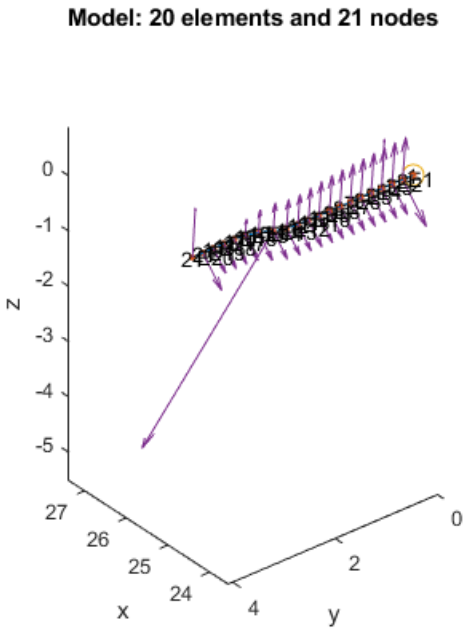

Figure 4.34: Pylon FEM loading in blade loss conditions.

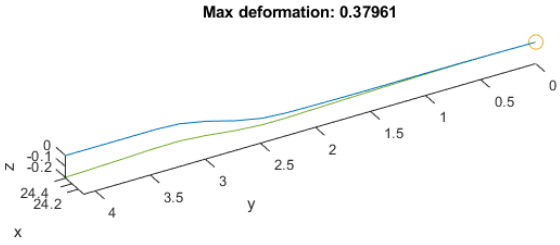

Figure 4.35: CFRP pylon FEM deformations in blade loss conditions.

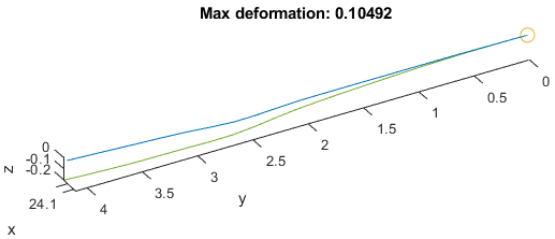

Figure 4.36: Aluminium pylon deformations in blade loss conditions.

Lastly, the static response in blade loss conditions was evaluated. The forces and moments are estimated using Equation 2.21, where the time was set to 0, to simulate initial load, and the rotational speed was considered to be 5% of take-off weight, to simulate windmilling. This is also the limit that can be sustained when aluminium is applied. Making the pylon out of CFRP results in almost half the weight and can sustain up to 60% of take-off RPM.

4.2.2. VIBRATION ANALYSIS

The results of the vibration analysis runs as described in Section 3.4.4 will be discussed. Figures 4.37 and 4.38 show respectively the fixed and loaded nodes on the pylon. As discussed in Section 3.1 also here the pylon is 'clamped' to the fuselage, which is represented by the encastre nodes. The blade loss load is applied at the nodes where the engine centre location is estimated to be.

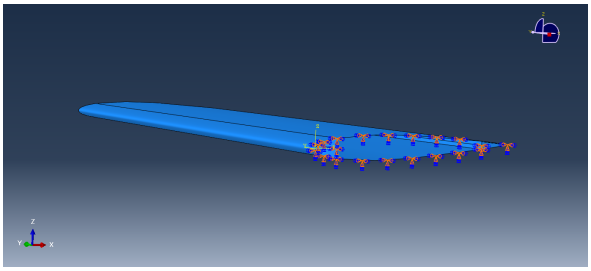

Figure 4.37: Pylon modelling for vibration analysis - fixed nodes.

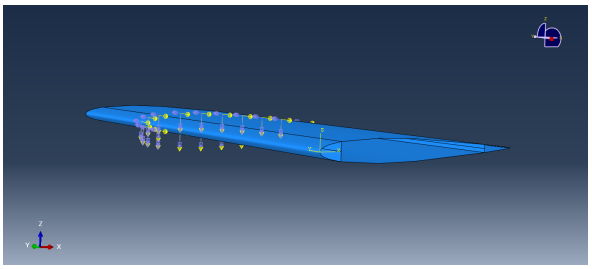

Figure 4.38: Pylon modelling for vibration analysis - loaded nodes.

Firstly, the five most damaging modes have been identified by running a frequency analysis with no load applied. The aluminium pylon results are illustrated in Figures 4.39 - 4.43. Those give an indication to what range of frequency the analysis should cover. Keeping in mind the loading as illustrated in Figure 4.38, for both configurations it is expected that modes 2, 3 and 5 will be most critical.

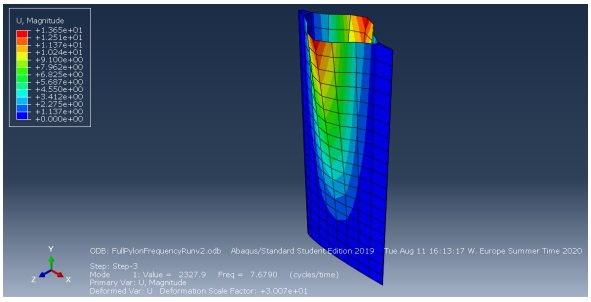

Figure 4.39: Aluminium pylon frequency mode 1 $f = 7.67[Hz]$.

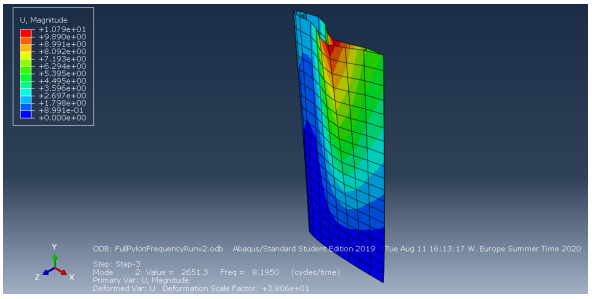

Figure 4.40: Aluminium pylon frequency mode 2 $f = 8.19[Hz]$.

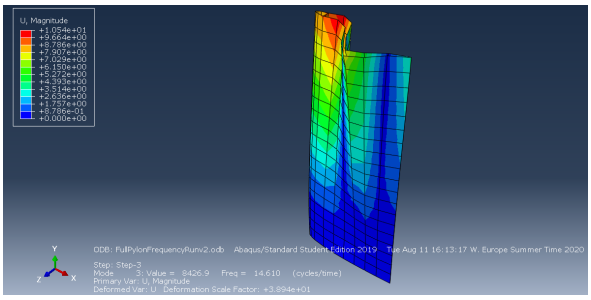

Figure 4.41: Aluminium pylon frequency mode 3 $f = 14.6[Hz]$.

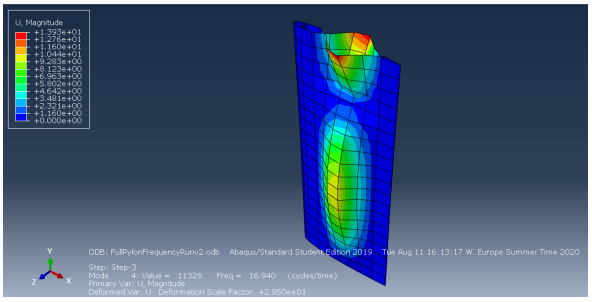

Figure 4.42: Aluminium pylon frequency mode 4 $f = 16.9[Hz]$.

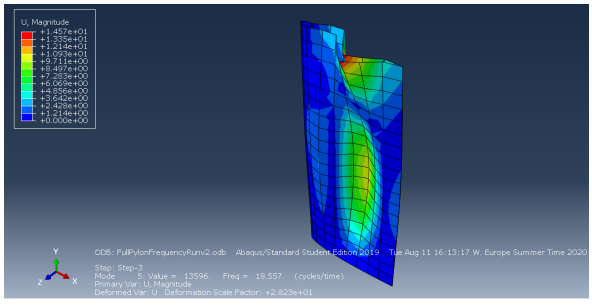

Figure 4.43: Aluminium pylon frequency mode 5 $f = 18.6[Hz]$.

When carbon-fibre-reinforced polymer is used, the modes shapes are identical, but they occur in different higher frequencies and show higher displacements, see Figures 4.44 - 4.48.

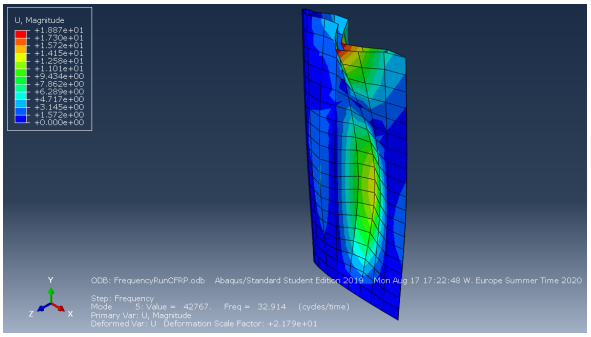

Figure 4.44: CFRP pylon frequency analysis mode 1 $f = 13.6[Hz]$.

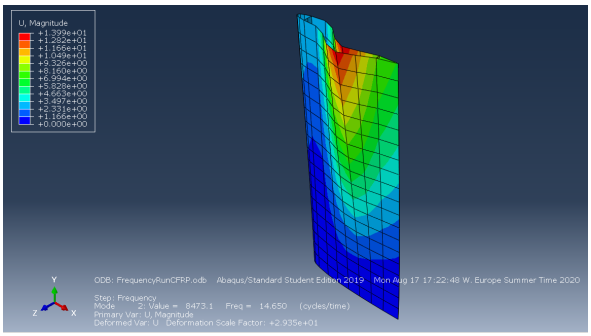

Figure 4.45: CFRP pylon frequency analysis mode 2 $f = 14.7[Hz]$.

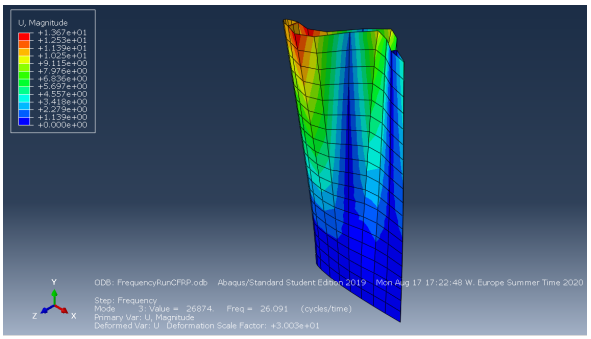

Figure 4.46: CFRP pylon frequency analysis mode 3 $f = 26.1[Hz]$.

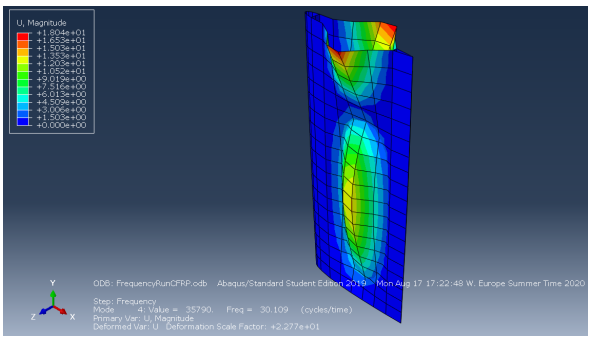

Figure 4.47: CFRP pylon frequency analysis mode 4 $f = 30.1[Hz]$.

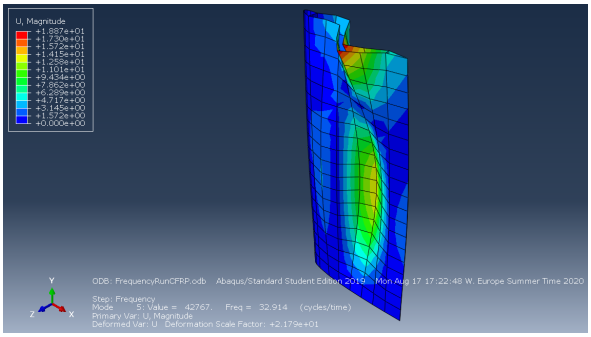

Figure 4.48: CFRP pylon frequency analysis mode 5 $f = 32.9[Hz]$.

Thereafter the load has been applied and a steady state analysis is run. As previously discussed, the applied force and moment are calculated using Equation 2.21, where F_c is the centrifugal force caused by the imbalance of the engine. Assuming that all the remaining blades are intact and balanced prior to the failure, the force is expressed by the mass and acceleration of one blade. To simulate critical conditions, complete blade loss is considered. This results in the $F_c = 2.9483e+05[N]$ and $M_{oop} = 2.6156e+05[Nm]$ at take-off conditions.

Consequently, the frequency to displacement has been illustrated in Figure4.49. It can be identified that the two most damaging frequencies are at $f \approx 8[hz]$ and $f \approx 14.8[hz]$ for the aluminium and $f \approx 14.7[hz]$ and $f \approx 26[hz]$ for the CFRP pylon, which correspond to the corresponding modes 2 and 3. This is in alignment with the previous expectations.

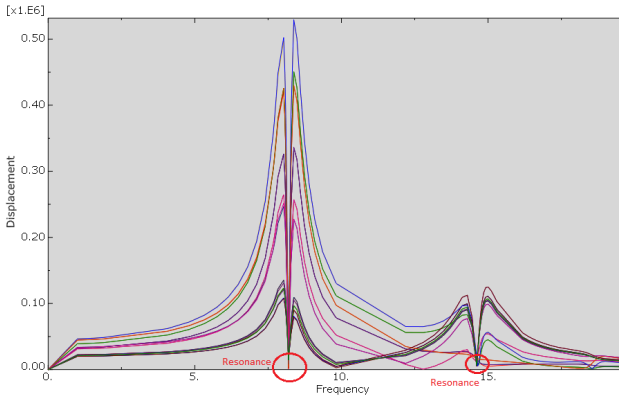

Figure 4.49: Frequency plot of all nodes with resonance frequency indicated to be around 8[Hz] for aluminium pylon.

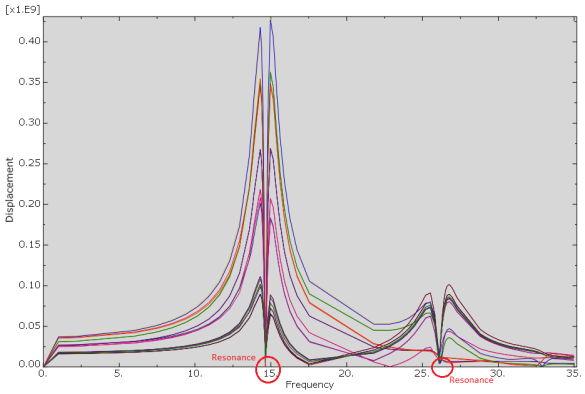

Figure 4.50: Frequency plot of all nodes with resonance frequency indicated to be around 14.5[Hz] for CFRP pylon.

Furthermore, it can be observed that excessively large maximum deflections are present. Figures 4.51 - 4.54 present the structural response of the aluminium pylon.

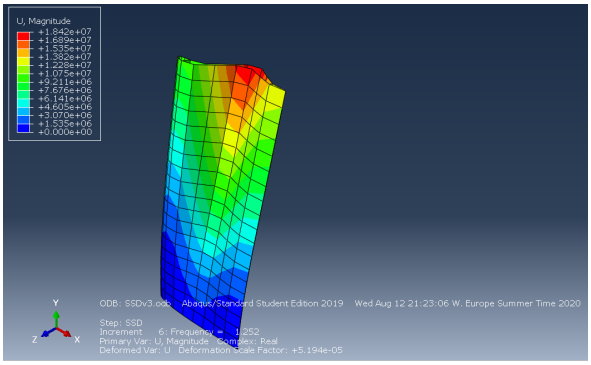

Figure 4.51: Aluminium pylon deformations at $f = 1.2[Hz]$, steady state analysis at blade loss conditions.

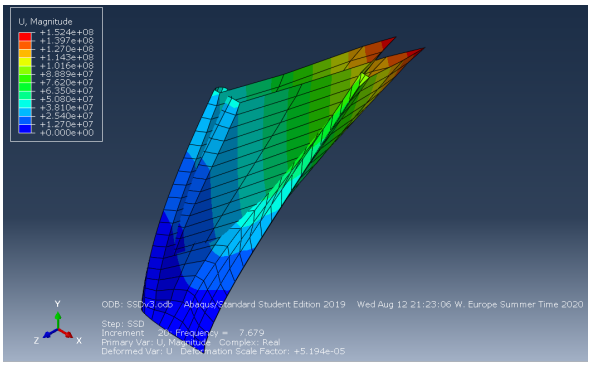

Figure 4.52: Aluminium pylon deformations at $f = 7.7[Hz]$, steady state analysis at blade loss conditions.

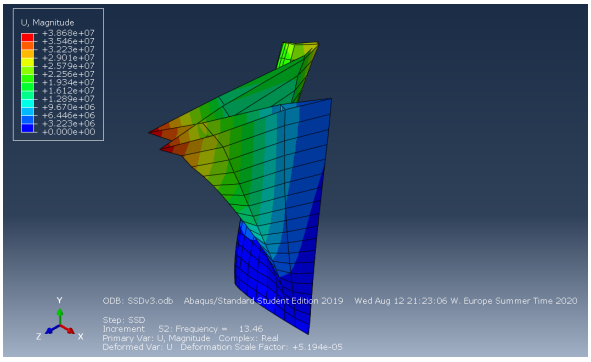

Figure 4.53: Aluminium pylon deformations at $f = 13.5[Hz]$, steady state analysis at blade loss conditions.

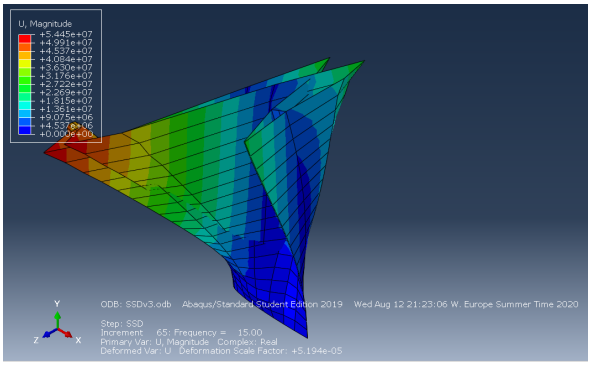

Figure 4.54: Aluminium pylon deformations at $f = 15.0[Hz]$, steady state analysis at blade loss conditions.

The CFRP response is similar with deformations shown in Figures 4.55 - 4.58.

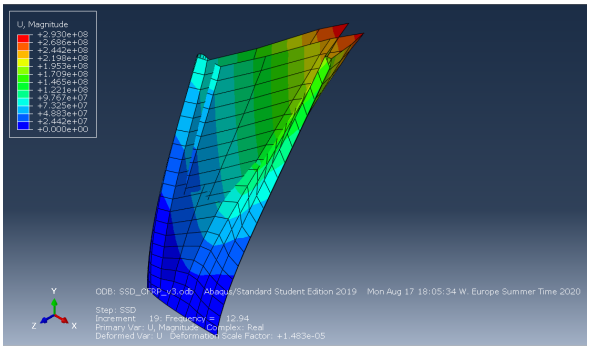

Figure 4.55: CFRP pylon deformations at $f = 12.9[Hz]$, steady state analysis at blade loss conditions.

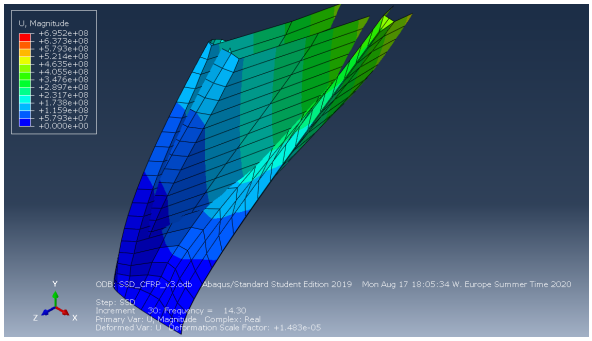

Figure 4.56: CFRP pylon deformations at $f = 14.3[Hz]$, steady state analysis at blade loss conditions.

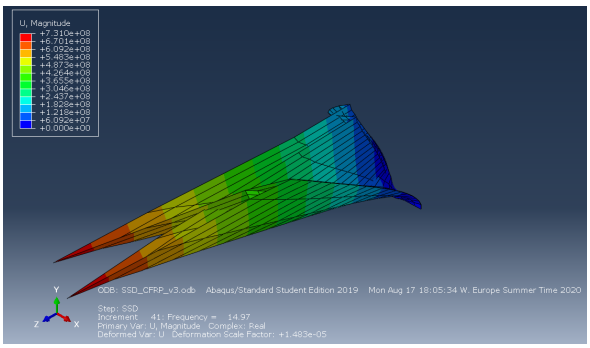

Figure 4.57: CFRP pylon deformations at $f = 14.9[Hz]$, steady state analysis at blade loss conditions.

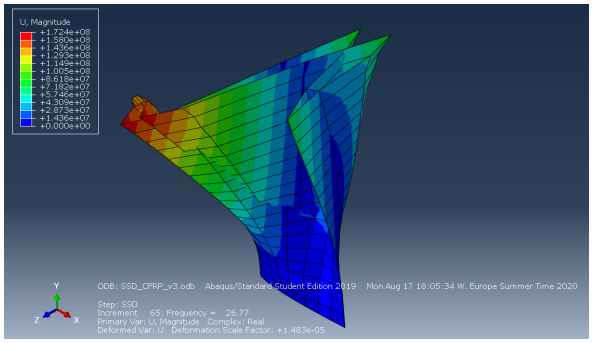

Figure 4.58: CFRP pylon deformations at $f = 26.7[Hz]$, steady state analysis at blade loss conditions.

It can be concluded that in the current layout, the pylon is not capable of supporting blade loss vibrations. More detailed analysis and thus design is recommended to be done in a later stage when the real engine settings, propeller design and operational procedures are known.

5

DUUC PERFORMANCE EVALUATION

Having defined a new sizing method for the propulsive empennage, it is important to see if the expectations that DUUC's performance is indeed improved are met. For this four different configurations will be compared: the original DUUC with empirically estimated propulsive empennage weight, and three configurations with the new FEM model implemented where both the pylon and the duct are made out of aluminium, one where the duct is CFRP and one that both the components are from CFRP. Firstly, the propulsion system mass will be discussed in Section 5.1. The impact on the the overall performance indicators is then presented in Section 5.2. Some typical missions performance will be presented in Section 5.3. Finally, top-level performance of the DUUC will be compared to the reference conventional configuration represented by ATR72-600.

Please note that for the performance evaluation, a number of parameters are take from the reference ATR aircraft, such as cruise altitude of 7000[m], payload mass of 7500[kg] and range of 1530[km].

5.1. PROPULSION SYSTEM MASS

The final mass results for the duct, pylon and total engine are given in Table 5.1. It can be seen that implementing the analysis decreases the duct weight to more than half what it is estimated with the empirical relations but the pylon on the other hand is underestimated. Nevertheless, more accurate analysis reduces the engine weight with 10%. This result is also clearly visible when comparing Figure 5.1 with Figure 5.2, where the nacelle contribution to the total engine weight is reduced from the initial 25% to 18%.

Using a lighter material, such as the CFRP, for the duct structure drastically impacts its weight and reduces it with almost 40%. As the duct mass is used for sizing the pylon, its mass is also slightly decreased. However, from Section 3.4 it was also observed that the duct mass is not the main contributor to pylon's sizing, where engine thrust loading is actually the highest and most severe loading present and therefore the impact on pylon's weight is not significant. Total engine weight is then reduced by 14% and the nacelle's contribution to total engine weight is now only 15%, equal to the one of the propeller.

Best mass results are obtained when the complete nacelle group is made out of CFRP, which is due to its high strength to density ratio, which allows for the structure to carry the same load with lower components thickness and thus structural weight. The duct mass is now only 26% of the original and total engine's mass is reduced by 20%. Furthermore, it is seen that, as the different components sizing are interrelated, complete engine size reduction is achieved. As this is one of the heaviest components, the impact on structural weight is significant. Lower structural weight for the same payload and range leads to lower overall weight and therefore smaller engines are feasible. In return this leads to lower structural weight and so forth. This is the so-called snow ball effect.

Part	Original empennage	Aluminium empennage	Duct CFRP Pylon Aluminium	CFRP empennage
Duct mass [kg]	236.1	101.2	62.1	60.9
Pylon mass [kg]	90.4	115.4	110.0	43.1
Total engine mass [kg]	1315	1187	1132	1045

Table 5.1: Duct, pylon and engine mass for different configurations.

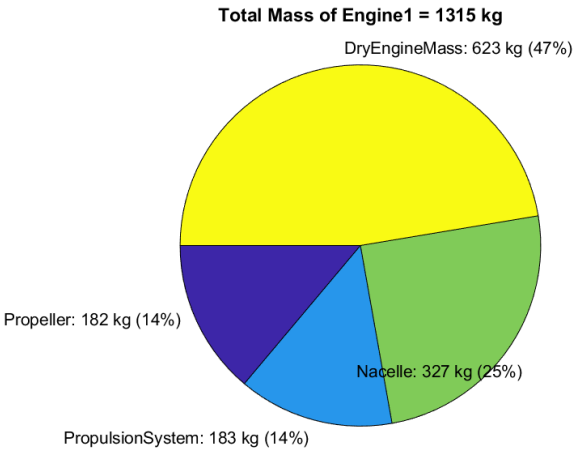

Figure 5.1: Original propulsion system with empirical relations used for weight estimation.

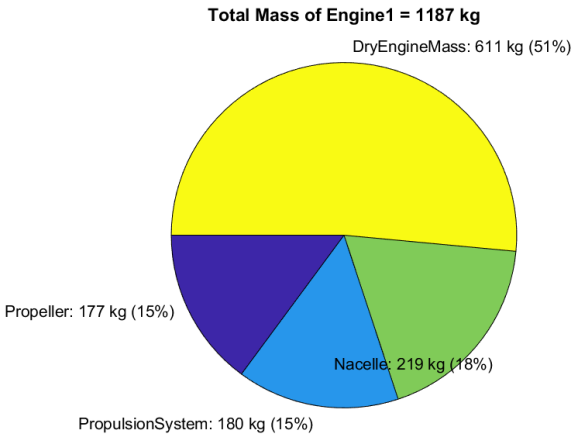

Figure 5.2: Propulsion system mass with analysis integrated and aluminium nacelle structure.

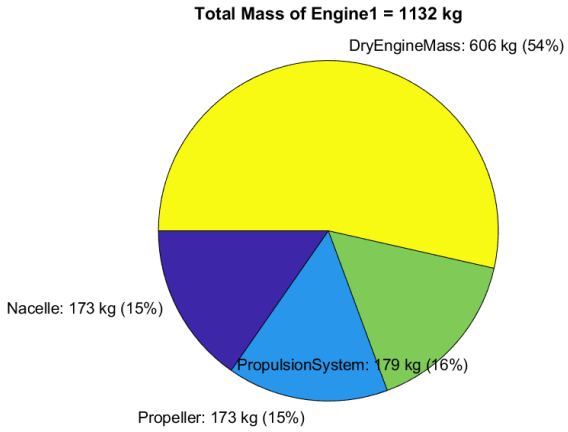

Figure 5.3: Propulsion system mass with analysis integrated and aluminium pylon and CFRP duct structure.

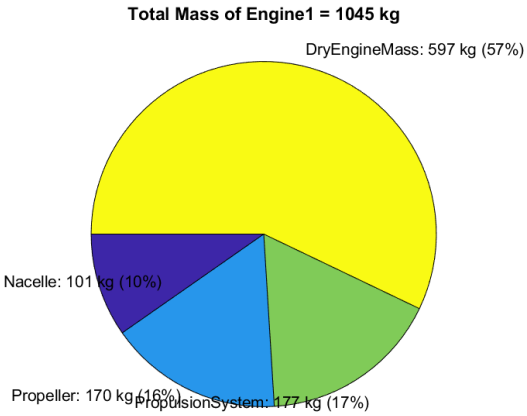

Figure 5.4: Propulsion system mass with analysis integrated and CFRP nacelle structure.

5.2. GENERAL PERFORMANCE INDICATORS

Reducing the mass of one of the major aircraft components naturally affects the overall structural weight, but also fuel weight required for the harmonic (or design) mission and payload requirement and therefore maximum take-off weight. This is also observed in Table 5.2, where the decrease in maximum take-off mass (MTOM) with a tonne, which is reflected in the operational empty mass as well, is presented. Furthermore, decreasing the propulsive empennage's weight effects the structural centre of gravity location, which has moved with almost 2%$L_{fuselage}$ and allows for a more forward position of the wing. Those two contribute to lower shift of complete aircraft's centre of gravity location, see Figures 5.5 and 5.6. This ultimately leads to reduced cruise drag as can be seen in Figures 5.7 and 5.8, where the original to the lightest solutions are compared.

Configuration Unit	MTOM [t]	OEM [t]	FM [t]	Wing Location [%$L_{fuselage}$]	Structure CG [%$L_{fuselage}$]	CG Shift [%MAC]
Original empennage	25.6	15.8	2.3	45.9	53.2	41.1
Al empennage	25.2	15.4	2.2	45.2	52.3	40.7
Duct CFRP Pylon Al	24.9	15.2	2.2	44.9	51.9	40.9
CFRP empennage	24.6	14.9	2.2	44.4	51.3	40.2

Table 5.2: Performance indicators for the different configurations.

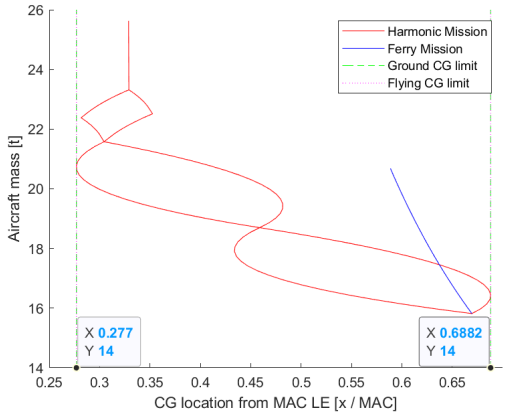

Figure 5.5: Centre of gravity shift during loading for the original configuration.

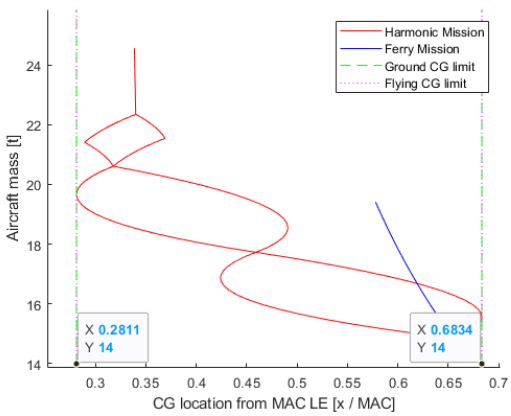

Figure 5.6: Centre of gravity shift during loading for DUUC with analysis integrated and CFRP nacelle structure.

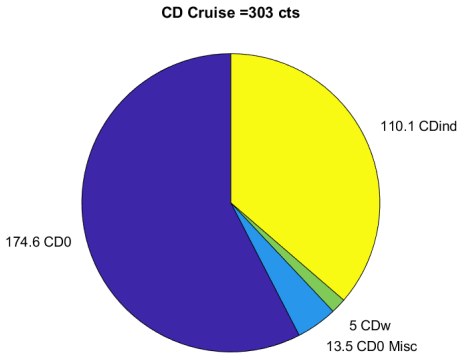

Figure 5.7: Original total cruise drag breakdown.

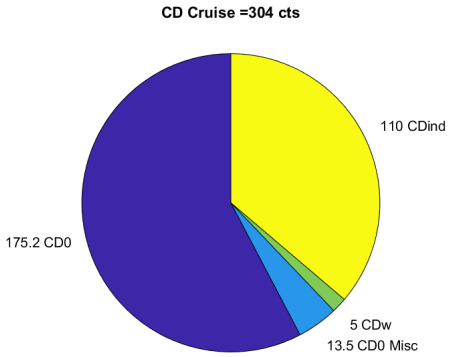

Figure 5.8: Total cruise drag breakdown with analysis integrated and CFRP nacelle structure.

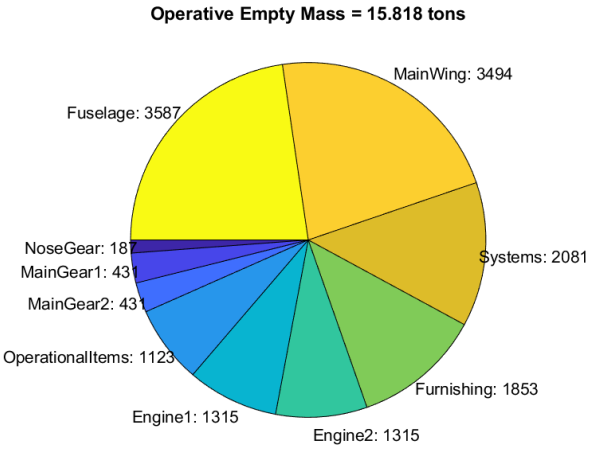

Figure 5.9: Original operational empty mass breakdown.

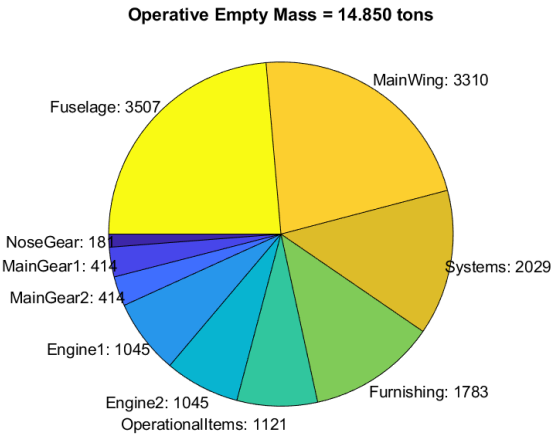

Figure 5.10: Operational empty mass breakdown with analysis integrated and CFRP nacelle structure.

Figures 5.9 and 5.10 show the operational empty mass breakdown for the two configurations. It first illustrates the great contribution to overall structural weight the engine has as well as illustrate the snow-ball effect

discussed above: due to the decrease in weight of one substantial system, other systems can be also smaller. In this case, a 226[kg] decrease in nacelle weight allows for 6[kg] lighter nose landing gear, the main gears is lighter with 17[kg] each and the wing change is of -184[kg]. All those contribute to a tonne of overall structural weight decrease.

5.3. MISSIONS PERFORMANCE

Figures 5.11 and 5.12 show the harmonic missions of the original configuration and the one with lowest duct and pylon weight - the configuration with CFRP. It can be seen that, even though the structural weight of the latter is decreased with respect to the original, the CFRP configuration achieves the same range. This is attributed to the fact that the Initiator uses the range and payload masses as performance requirements, thus kept constant. However, if the MTOM was kept constant and having a lower structural weight two options would be present, the aircraft can either carry higher payload mass or cover larger range. which is sufficient to achieve the specific range at harmonic mission.

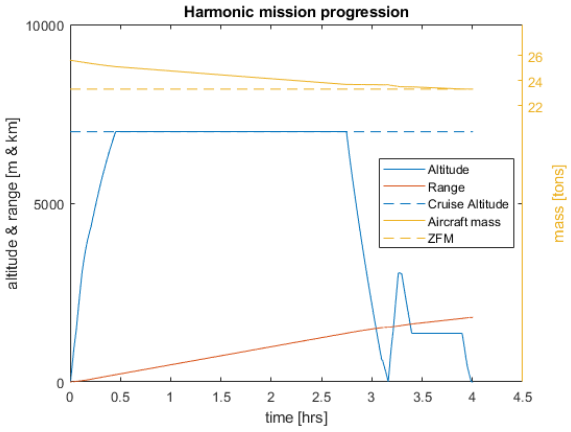

Figure 5.11: Original harmonic mission.

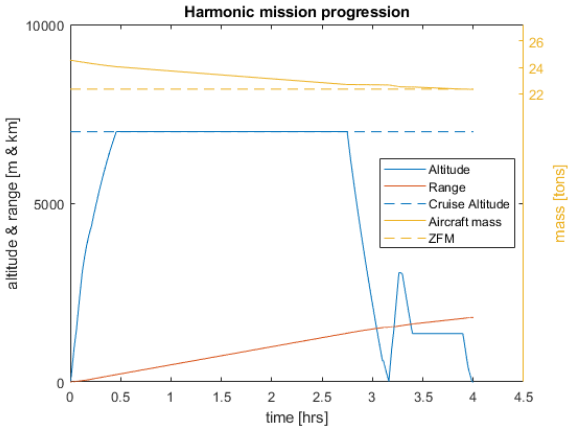

Figure 5.12: Harmonic mission with analysis integrated and CFRP nacelle structure.

Figures 5.13 and 5.14 represent the aircraft mission when maximum fuel capacity is considered. It can be seen that the updated configuration can climb to a slightly higher altitudes in shorter time, which is explained by the lower MTOM with the same engine capabilities. This is also observed in Figures 5.15 and 5.16, where the two ferry missions have been presented.

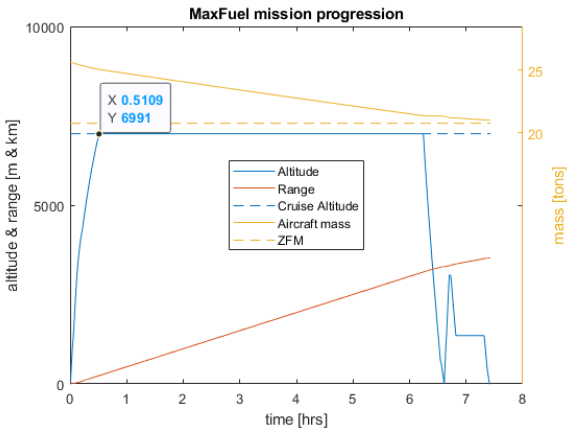

Figure 5.13: Original max fuel mission.

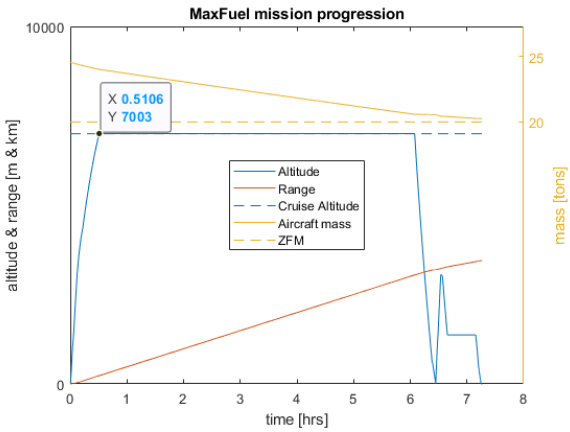

Figure 5.14: Max fuel mission with analysis integrated and CFRP nacelle structure.

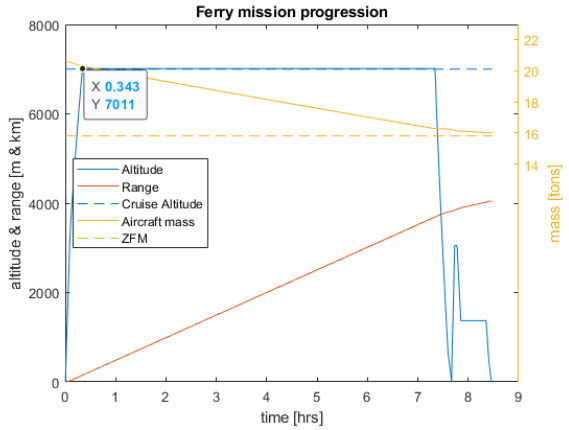

Figure 5.15: Original ferry mission.

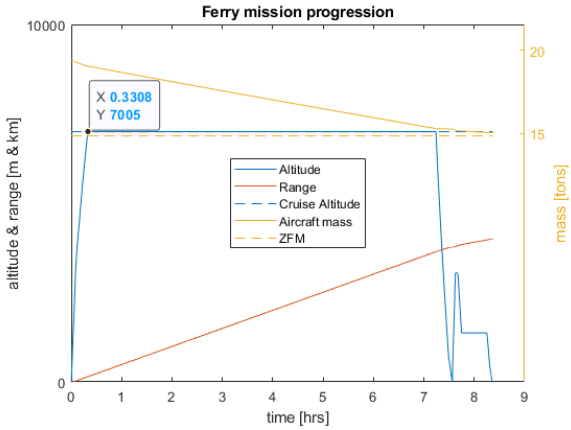

Figure 5.16: Ferry mission with analysis integrated and CFRP nacelle structure.

5.4. PERFORMANCE COMPARISON WITH REFERENCE AIRCRAFT

This section presents a to-level comparison of the DUUC with the method implemented and a CFRP empennage to the reference ATR 72-600 aircraft. Firstly, the key performance indicators will be compared in Table 5.3. Please note that for this comparison the stability module has not ben incorporated and therefore the wing position is constant for each concept throughout the analysis.

Configuration Unit	MTOM [t]	OEM [t]	FM [t]	Structure CG [$\%L_{fuselage}$]	CG Shift [$\%MAC$]
ATR	23.9	14.0	2.4	44.5	32.0
DUUC	24.7	15.0	2.2	54.7	40.4

Table 5.3: Performance indicators comparison of DUUC to ATR.

The analysis shows that for the same range and payload requirement, the conventional configuration has lower maximum take-off mass. This is largely contributed to the lower structural weight as well as less required fuel. Here again great differences in the structural centre of gravity and overall CG shift during flight has been observed.

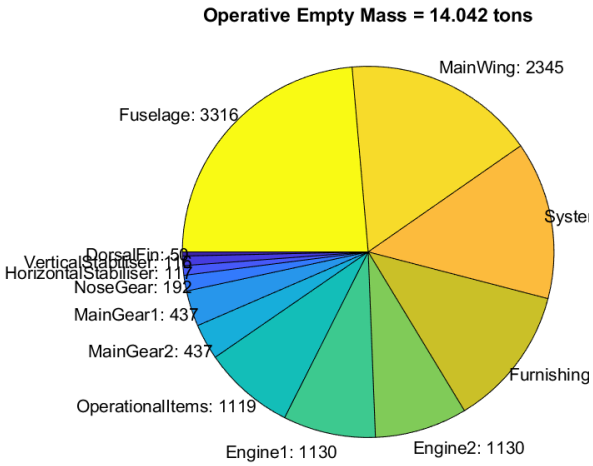

Figure 5.17: Original operational empty mass breakdown.

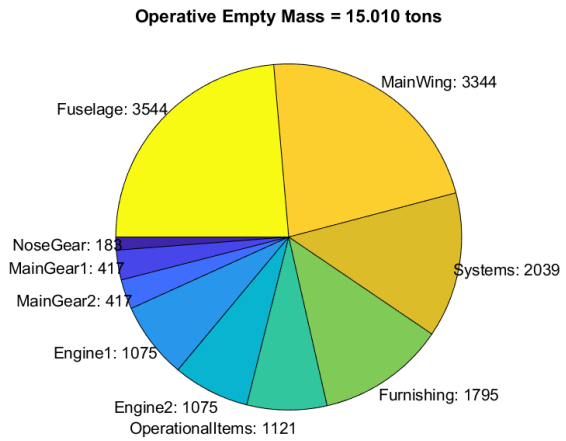

Figure 5.18: Operational empty mass breakdown with analysis integrated and CFRP nacelle structure.

From Figures 5.17 and 5.18 it can seen that the engines contribution to the overall weight is actually higher for ATR than for the DUUC. This therefore leads to the conclusion that indeed the position of the propulsive system and therefore centre of gravity location have much higher impact than the system weight.

Figures 5.19 and 5.20 then show the propulsive system weight breakdown, where it can be seen that the ATR engine mass is higher with the largest difference being at the nacelle group, which is still sized by Class 2 weight estimation methods and is believed to be over-predicted.

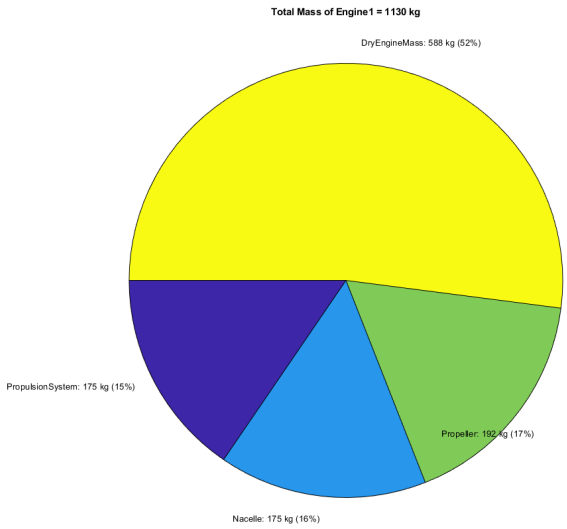

Figure 5.19: ATR propulsion system mass break down.

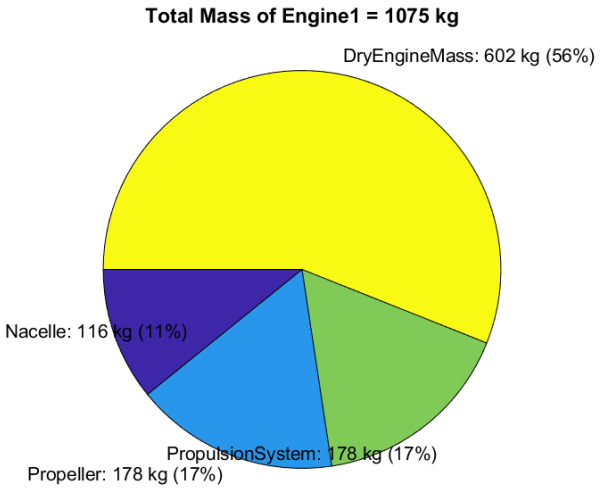

Figure 5.20: DUUC propulsion system mass break down.

Last but not least, the maximum fuel mission performance of the two configurations has been compared, see Figures 5.21 and 5.22. It can be observed that, as expected, the heavier configuration, namely the DUUC, takes longer time to climb to cruise altitude. It also shows 200$[km]$ lower range capabilities when compared to the conventional configuration.

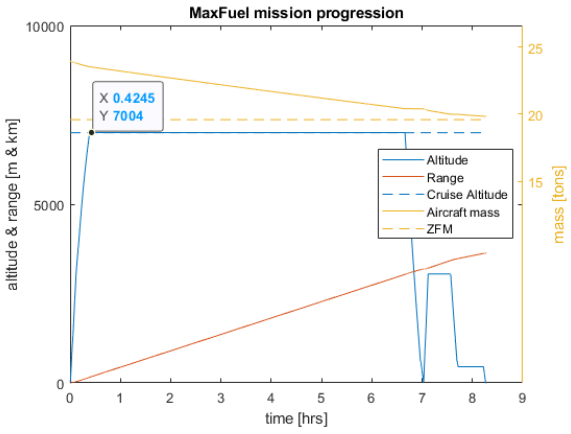

Figure 5.21: ATR ferry mission.

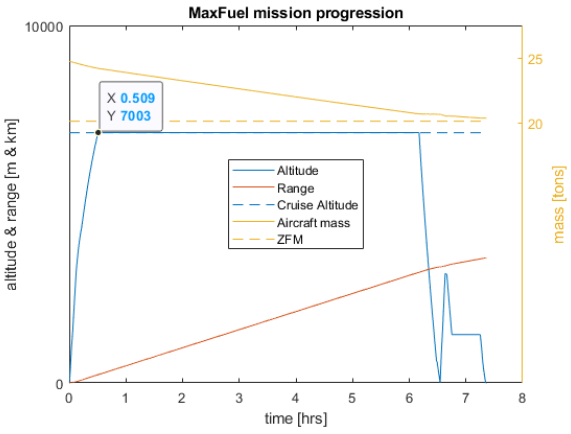

Figure 5.22: DUUC ferry mission.

It can be thus concluded that, even with ore accurate and design-sensitive propulsive empennage weight estimation, the DUUC cannot achieve the same performance as the conventional configuration. However, please note that a number of modules need to be improved in the Initiator, such as horizontal stability which defines the wing position. Furthermore, it is believed that an dedicated propeller design would drastically improve the figures above by giving a better power and size estimation as well as allowing for shape optimisation of the duct.

6

Conclusions and Recommendations

This chapter will provide the closing of this study by first giving the general conclusions in Section 6.1. Lastly, recommendations to future work will be given in Section 6.2.

6.1. Conclusions

The Delft University Unconventional Concept, which features ducted propellers positioned furthest aft on the fuselage in order to also act as vertical and horizontal stabilisers, has been subject to thorough studies in the Aerospace Engineering Faculty of TU Delft. One of the main challenges has proven to be the aft centre of gravity location and its excursion during flight, due to positioning the heavy propulsive empennage on the tail cone, that results in higher trim drag. Furthermore, higher operational empty and maximum take-off mass when compared to a conventional wing-mounted or tail-mounted propeller configurations have been observed, which consequently leads to lower range for the same payload. It has been realised, however, that the ducts' and pylons' weight, which impacts severely the overall performance, has not been estimated in sufficient detail. Therefore, a more accurate and design-sensitive method that is based on physical analysis, rather than empirical, is required in order to be able to make a more accurate aircraft performance prediction.

The focus of this study was to develop such a design-sensitive physics-based method which will determine the propulsive empennage's mass. It was concluded that Class 2.5 weight estimation method that uses a simplified Finite Element Method (FEM) will be used for the design when considering static loading. This was seen to allow for sufficiently high detail analysis for a conceptual design stage without having to pay the cost of excessive computational power required for Class 3 and higher weight estimation methods.

The research at hand was initiated by identifying the critical sizing conditions for the multifunctional innovative structure. Three critical design conditions were identified for the duct: take-off, when the engine is at full power and therefore creates high aerodynamic load on the surface; cruise, which is the larger portion of the flight and is the typical condition nacelles are sized for; and dive, when highest speed and therefore dynamic pressure is experienced by the structure and when the stabilisers need to provide uncompromised stability forces.

The structure was represented by a number of beams, with their cross sectional areas and moments of inertia. Those were then used for the definition of a stiffness matrix and by solving the equilibrium equations the beams deformations were obtained. The shear flow and normal stress on the cross-section were determined, based on which the total stresses on the skins were obtained.In case any of those surpasses the maximum allowable stress, which depends on the material, the thickness is increased proportional to the lacking strength and the analysis is carried out again. This iteration is repeated until every skin reserve factor is higher than 1.

It was observed that when keeping the original aluminium material, the duct's mass is less than half of what was initially predicted by the empirical relations. Further reduction can be achieved by changing the material to CFRP when a mass reduction of more than 70% of the duct weight is observed. Last but not least, a protective kevlar layer has been designed such that any pieces of blade in case of a failure can be contained.

Next to this the pylon was also analysed by a Class 2.5 weight estimation method. The structure was again discretised in beams, with their cross sectional areas and moments of inertia, and nodes. The distributed

loads from the aerodynamic forces on the pylon were applied as well as the updated duct weight and the aerodynamic forces it has been estimated that the ring wing with the propeller working provides. The engine and duct masses as well as engine thrust were also introduced as point loads. The method actually identified that, if the material is kept to original aluminium, there is a need for higher pylon mass, which is contributed to the high loading coming from the engine thrust. A drastic reduction to less than half the original weight however can be achieved if the material is changed to CFRP.

Already in the initial literature review it has been identified that the critical loading on engine mount systems is typically in blade loss conditions, when the imbalance of the engine propeller system causes severe vibrations on the pylon. One of the prime requirements on the engine mount system was discovered to be cancelling the excessive vibration loads before reaching the airframe. As this analysis is seen too detailed for the conceptual design phase, the proposed method does not implement a dynamic FEM model. However, a static stress analysis of the load in the initial blade loss phase showed that the aluminium pylon can carry the load of 5% of the take-off engine RPM. If CFRP is used, up to 60% of the RPM can be accommodated by the pylon with a small structural weight penalty. Furthermore, the structure was inputted in a off-the-shelf FEM software called Abaqus and the relevant loads were applied. Unfortunately it was observed that with the current set-up the system cannot meat the excessive structural loads and therefore a specific design campaign needs to focus on those performance requirements. Please note that dynamic analysis is not typical at conceptual design phase, when a lot of variables such as engine design and operation conditions are still unknown and thus no further elaboration on the matter was proposed.

This method was also integrated in the overall analysis, which allowed to observe if the more accurate weight estimation has beneficial effect on the performance assessment of the concept. As expected, a reduction in operational empty weight, which naturally lead to lower maximum take off weight, was achieved. Highest improvements were achieved by integrating a CFRP empennage reducing the mass by 1 tonne. A small decrease in fuel weight was also observed. Based on the procedures given in the Initiator, however, those did not have a signifiant impact on the DUUC's mission performance, which can be best qualified by the additional 100[km] range in maximum fuel mission. The effect on the ferry mission identified in the better climb performance due to the lower structural and therefore overall weight.

If the maximum take-off weights are compared, clear performance improvements are observed which also allow for better wing position and shorter centre of gravity excursion. Another way to look at it is, in case the MTOM is kept constant, the weight freed by the lower structural weight can be used for more fuel and therefore, with the same engine characteristics, higher range capabilities with the same payload. On the other hand, if the range is still kept constant, the aircraft can carry higher payload over the same distance.

Lastly, a performance comparison to conventional configuration was carried out. It was concluded that, even with the more accurate empennage weight estimation, the DUUC is not capable of delivering the same performance as the reference ATR72-600. Please note that many modules in the Initiator have been in continuous revision, like for example the one that chooses the best wing and other major systems position, which is believed to have influenced the results.

6.2. RECOMMENDATIONS

A number of recommendation for future DUUC research work can be made.

Firstly, it is important that a thorough and design-sensitive propeller design is carried out. Throughout the whole DUUC analysis main focus has been put on the ducts as ring wings. However, the benefits to static thrust and therefore improved propeller performance have not been explored and integrated in the concept's performance study. Moreover, when real performance parameters and therefore inputs to the duct aerodynamic analysis are present, it is expected that more beneficial, less damaging to the structure, external loads will be obtained, which could allow for further weight reduction and thus larger benefits.

Having defined the propeller design, and if required, after a control surface redesign, the duct shape expressed by the aspect ratio should be optimised. As discussed before, various researches have shown that AR or 2 is a good design choice that allows for both improvements to engine thrust and good ring wing aerodynamic performance that provides lift without the cost of excessive drag. However, an optimisation campaign that considers the two could contribute to even better design solutions.

In later design stages, it is recommended that a real lift distribution over the duct circumference in different

angles of attack is defined. For this, a thorough CFD analysis is recommended.

It was difficult to evaluate the DUUC performance improvement using the Initiator with the main issue being that the wing positioning module, which depends on the stability analysis, has not been very reliable. This is also the reason the performance comparison to the reference ATR aircraft has been challenging. It is expected that if more reliable wing positioning is obtained, the benefits to the concept performance will be more clear.

A

CS25 Design Requirements

This appendix lists the most relevant CS23 regulations as stated by EASA[67]. Section A.1 lists the general sizing considerations. The tail design is discussed in Section A.2 and Section A.3 lists the relevant requirements to the propulsion system.

A.1. General

CS 25.301 Loads:

Strength requirements are specified in terms of limit loads (the maximum loads to be expected in service) and ultimate loads (limit loads multiplied by prescribed factors of safety). Unless otherwise provided, prescribed loads are limit loads.

CS 25.303 Factor of Safety

Unless otherwise specified, a factor of safety of 1.5 must be applied to the prescribed limit load which are considered external loads on the structure. When loading condition is prescribed in terms of ultimate loads, a factor of safety need not be applied unless otherwise specified.

CS 25.305 Strength and Deformation

(a) *The structure must be able to support limit loads without detrimental permanent deformation. At any load up to limit loads, the deformation may not interfere with safe operation.*

(e) *The aeroplane must be designed to withstand any vibration and buffeting that might occur in any likely operating condition up to V_D/M_D, including stall and probable inadvertent excursions beyond the boundaries of the buffet onset envelope. This must be shown by analysis, flight tests, or other tests found necessary by the Agency.*

(f) *Unless shown to be extremely improbable, the aeroplane must be designed to withstand any forced structural vibration resulting from any failure, malfunction or adverse condition in the flight control system. These loads must be treated in accordance with the requirements of CS 25.302*

CS 25.321 Flight Loads - General

(a) *Flight load factors represent the ratio of the aerodynamic force component (acting normal to the assumed longitudinal axis of the aeroplane) to the weight of the aeroplane. A positive load factor is one in which the aerodynamic force acts upward with respect to the aeroplane.*

CS 25.335 Design Airspeeds

(b) *Design dive speed, V_D. V_D must be selected so that V_C/M_C is not greater than 0.8 V_D/M_D, or so that the minimum speed margin between V_C/M_C and V_D/M_D is the greater of the following values.*

CS 25.561 Emergency Landing Conditions - General

(a) *The aeroplane, although it may be damaged in emergency landing conditions on land or water, must be designed as prescribed in this paragraph to protect each occupant under those conditions.*

(c) *For equipment, cargo in the passenger compartments and any other large masses, the following apply.*

(2) *When such positioning is not practical (e.g. fuselage mounted engines or auxiliary power units) each such item of mass must be restrained under all loads up to those specified in sub-paragraph (b)(3) of this paragraph. The local attachments for these items should be designed to withstand 1·33 times the specified loads if these items are subject to severe wear and tear through frequent removal (e.g. quick change interior items).*

A.2. TAIL DESIGN

CS 25.331 Symmetric Manoeuvring Conditions

(c) Manoeuvring pitching conditions. The following conditions must be investigated:

(1) *Maximum pitch control displacement at V_A. The aeroplane is assumed to be flying in steady level flight (point A_1, CS 25.333 (b)) and the cockpit pitch control is suddenly moved to obtain extreme nose up pitching acceleration. In defining the tail load, the response of the aeroplane must be taken into account. Aeroplane loads which occur subsequent to the time when normal acceleration at the c.g. exceeds the positive limit manoeuvring load factor (at point A_2 in CS.333(b)), or the resulting tailplane normal load reaches its maximum, whichever occurs first, need not be considered.*

CS 25.351 Yaw Manoeuvre Conditions

The aeroplane must be designed for loads resulting from the yaw manoeuvre conditions specified in sub-paragraphs (a) through (d) of this paragraph at speeds from V_{MC} to V_D. Unbalanced aerodynamic moments about the centre of gravity must be reacted in a rational or conservative manner considering the aeroplane inertia forces. In computing the tail loads the yawing velocity may be assumed to be zero.

A.3. ENGINE SYSTEMS

CS 25.361 Engine and Auxiliary Power Unit Torque

(a) For engine installations:

(1) *Each engine mount, pylon and adjacent supporting airframe structures must be designed for the effects of:*

(i) *a limit engine torque corresponding to take-off power/thrust and, if applicable, corresponding propeller speed, acting simultaneously with 75 % of the limit loads from flight condition A of CS 25.333 (b)*

(ii) *a limit engine torque corresponding to the maximum continuous power/thrust and, if applicable, corresponding propeller speed, acting simultaneously with the limit loads from flight condition A of CS 25.333 (b*

(iii) *for turbo-propeller installations only, in addition to the conditions specified in sub-paragraphs (a) (1) (i) and (ii) , a limit engine torque corresponding to take-off power and propeller speed, multiplied by a factor accounting for propeller control system malfunction, including quick feathering, acting simultaneously with 1 g level flight loads. In the absence of a rational analysis, a factor of 1.6 must be used.*

(2) *The limit engine torque to be considered under sub-paragraph (1) must be obtained by:*

(i) *for turbo-propeller installations, multiplying mean engine torque for the specified power/thrust and speed by a factor of 1.25*

(3) *The engine mounts, pylons, and adjacent supporting airframe structure must be designed to withstand 1 g level flight loads acting simultaneously with the limit engine torque loads imposed by each of the following conditions to be considered separately:*

(i) *sudden maximum engine deceleration due to malfunction or abnormal condition*

(ii) *the maximum acceleration of engine*

CS 25.362 Engine Failure Loads.

(a) *For engine mounts, pylons and adjacent supporting airframe structure, an ultimate loading condition must be considered that combines 1g flight loads with the most critical transient dynamic loads and vibrations, as determined by dynamic analysis, resulting from failure of a blade, shaft, bearing or bearing support, or bird strike event. Any permanent deformation from these ultimate load conditions should not prevent continued safe flight and landing.*

(b) *The ultimate loads developed from the conditions specified in paragraph (a) are to be:*

(1) *multiplied by a factor of 1.0 when applied to engine mounts and pylons;*

(2) *multiplied by a factor of 1.25 when applied to adjacent supporting airframe structure.*

CS 25.1193 Cowling and nacelle skin.

(a) *Each cowling must be constructed and supported so that it can resist any vibration, inertia, and air load to which it may be subjected in operation.*

(e) *Each aeroplane must:*

(1) *Be designed and constructed so that no fire originating in any fire zone can enter, either through openings or by burning through external skin, any other zone or region where it would create additional hazards;*

(3) *Have cowlings and nacelles skins, in areas subject to flame if a fire starts in an engine fire zone, complying with the following:*

(i) *For in-flight operations, cowlings and nacelles skins must be fireproof in the complete concerned areas, and*

(ii) *For ground operations, cowlings and nacelles skins must be:*

(a) *Fireproof in the portions of the concerned areas where a skin burn through would affect critical areas of the aeroplane*

BIBLIOGRAPHY

[1] EASA, EEA, EUROCONTROL, *European Aviation Environmental Report 2019*, Tech. Rep. ISBN:978-92-9210-214-2 (EASA, EEA, EUROCONTROL, 2019).

[2] R. Vos and M. Hoogreef, *System-Level Assessment of Tail-Mounted Propellers for Regional Aircraft,* 31^{st} Congress of the International Council of the Aeronautical Science (2018).

[3] N. van Arnhem, *DUUC Aircraft with the Innovative 'Propulsive Empennage' Concept,* https://www.youtube.com/watch?v=VDbJBkcQBPI (2016).

[4] K. J. M. Hameeteman, *Unconventional Propulsive Empennage - Future or Fiction? Stability & Control Analysis and the Effect of Scaling of the DUUC*, Master Thesis (Delft University of Technology, Delft, the Netherlands, 2017).

[5] Fokker , *Fokker 50 Regional Turbo Prop,* http://www.flyfokker.com/Fokker_50.

[6] ATR, *Products - First Generation,* http://www.atraircraft.com/products/list.html.

[7] N.H.M. van den Dungen, *Synthesis of an Aircraft Featuring a Ducted-Fan Propulsive Empennage*, Master Thesis (Delft University of Technology, Delft, the Netherlands, 2017).

[8] V. N. Harinarain, *Aerodynamic Performance Study on a Ducted Propeller System for Propulsion and Control & Stability Applications*, Master Thesis (Delft University of Technology, Delft, the Netherlands, 2017).

[9] R. Elmendorp, R. Vos, and G. La Rocca, *A conceptual design and analysis method for conventional and unconventional airplanes,* 29th Congress of the International Council of the Aeronautical Sciences, ICAS 2014 , 1 (2014).

[10] Q. R. Wald, *The Aerodynamics of Propellers,* Progress in Aerospace Sciences **42(2)**, 85–128 (2006).

[11] L.Veldhuis, *Propeller Wing Aerodynamic Interference* , Doctoral dissertation (Delft University of Technology, Delft, the Netherlands, 2005).

[12] E. Torenbeek & Wittenberg, H., *Flight Physics : Essentials of Aeronautical Disciplines and Technology, with Historical Notes* (Springer, Dordrecht, 2009).

[13] D. E. V. Zante, *Progress in Open Rotor Research,* Proceedings of ASME Turbo Expo 2015: Turbine Technical Conference and Exposition , 1 (2015).

[14] L.Prandtl and O.G.Tietjens, *Applied Hydro- and Aeromechanics* (McGraw-Hill Book Company, Inc., New York and London, 1934).

[15] A. Maqsood and T. H. Go, *Aerodynamic Estimation of Annular Wings Based on Leading-Edge Suction Analogy,* AIAA Journal **51**, 529 (2013).

[16] L. W. Traub, *Experimental Investigation of Annular Wing Aerodynamics,* Journal of Aircraft **46**, 988 (2009).

[17] C.D. Cone, Jr, *The Theory of Induced Lift and Minimum Induced Drag of Nonplanar Lifting Systems*, Technical Report R-139 (National Aeronautics and Space Administration (NASA), Langley Research Center, Langley Station, Hampton, Va., 1963).

[18] J. Weissinger, *On the Aerodynamics of Ring Wings, 1. The Pressure Distribution on a Thin, Almost Axially Symmetric Wing in Subsonic Flow*, Technical Report (David Taylor Model Basin, 1957).

[19] W.B.Morgan, E.B.Caster , *Prediction of the Aerodynamic Characteristics of Annular Airfoils*, Research and Development Report 1830 (Clearinghouse for Federal Scientific and Technical Information, 1965).

[20] A. Kanoria and M. Damodaran, *Computational Prediction of Annular Wing Aerodynamic Characteristics,* Journal of Aircraft **54**, 815 (2017).

[21] M. J. Werle, *Aerodynamic Loads and Moments on Axisymmetric Ring-Wing Ducts,* AIAA Journal **52**, 2359 (2014).

[22] L.Stipa, *Stipa Monoplane With Venturi Fuselage*, Technical Memorandums 753 (National Advisory Committee for Aeronautics (NACA), Washington, 1934) translated by Dwight M. Miner.

[23] A. H. Sacks and J. A. Burnell, *Progress in Aerospace Sciences*, Tech. Rep. (1962).

[24] D.M.Black, H.S. Wainauski, C.Rohrbach, *Shrouded Propellers - A Comprehensive Performance Study,* AIAA 5^{th} Annual Meeting and Technical Display (1968), 10.2514/6.1968-994.

[25] R. D. Hager, *Advanced Turboprop Project*, Technical Report NASA SP-495 (National Aeronautics and Space Administration (NASA), NASA Lewis Research Center; Cleveland, OH, United States, 1988).

[26] J. H. Dittmar, *An Estimate of the Noise Shielding on the Fuselage Resulting from Installing a Short Duct Around an Advanced Propeller*, Technical Memorandum NASA-TM-100262 (National Aeronautics and Space Administration (NASA), NASA Lewis Research Center; Cleveland, OH, United States, 1988).

[27] R. D.Oleson and H.Patrick, *Small Aircraft Propeller Noise with Ducted Propeller,* 4^{th} AIAA/CEAS Aeroacoustics Conference , 464 (1998).

[28] A. M. Malgoezar, A. Vieira, M. Snellen, D. G. Simons, and L. L. Veldhuis, *Experimental Characterization of Noise Radiation from a Ducted Propeller of an Unmanned Aerial Vehicle,* International Journal of Aeroacoustics (2019), 10.1177/1475472X19852952.

[29] H. F. Mourão Bento, *Aerodynamic Interaction Effects of Circular and Square Ducted Propellers*, Master Thesis (Delft University of Technology, Delft, the Netherlands, 2019).

[30] E. Torenbeek, *Synthesis of Subsonic Airplane Design : An Introduction To The Preliminary Design Of Subsonic General Aviation And Transport Aircraft, With Emphasis On Layout, Aerodynamic Design, Propulsion And Performance* (Kluwer Academic, Dordrecht, 1982).

[31] D. Raymer & American Institute of Aeronautics and Astronautics, *Aircraft Design : A Conceptual Approach* (American Institute of Aeronautics and Astronautics, Reston, VA, 2012).

[32] J. Roskam, *Airplane Design pt. 5: Component Weight Estimation* (Roskam Aviation and Engineering, Ottawa, Kansas, 1985).

[33] European Aviation Safety Agency (EASA), *Type-Certificate Data Sheet for Engine PW100 series*, Tech. Rep. IM.E.041 (2018).

[34] R. Worobel and M. Mayo, *Advanced General Aviation Propeller Study*, Contractor Report 114399 (National Aeronautics and Space Administration (NASA), Springfield, 1972).

[35] P. Lolis, *Development of a Preliminary Weight Estimation Method for Advanced Turbofan Engines* , Ph.D Thesis (Cranfield University School Of Engineering, 2014).

[36] A. Elham, G. La Rocca, and M. J. van Tooren, *Development and Implementation of an Advanced, Design-Sensitive Method for Wing Weight Estimation,* Aerospace Science and Technology **29**, 100 (2013).

[37] J. Roskam, *Airplane Design pt. 1: Preliminary Sizing of Airplanes* (Roskam Aviation and Engineering, Ottawa, Kansas, 1985).

[38] M. E. Burt, *Royal Aircraft Establishment, RAE*, Tech. Rep. (Royal Aircraft Establishment RAE, 1955).

[39] E.Torenbeek, *Development and Application of a Comprehensive, Design-Sensitive Weight Prediction Method for Wing Structures of Transport Category Aircraft*, Technical Report LR-693 (Faculty of Aerospace Engineering, Delft University of Technology, Delft, 1992).

[40] R. Elmendorp, R. Vos, and G. La Rocca, *Comparative Design & Sensitivity Studies on Box-Wing Airplanes,* 29^{th} Congress of the International Council of the Aeronautical Sciences, ICAS 2014 , 1 (2014).

[41] R.D.Cook, D.S.Malkis, M.E.Plesha, R.J.Witt , *Concepts and Applications of Finite Element Analysis, 4^{th} Edition* (John Wiley & Sons, Inc., University of Wisconsin - Madison, 2002).

[42] T.H.G. Megson, *Aircraft Structures for Engineering Students (Fourth Edition)* (Elsevier Ltd., Oxford, United Kingdom, 2007).

[43] S. K. Sinha and S. Dorbala, *Dynamic Loads in the Fan Containment Structure of a Turbofan Engine,* Journal of Aerospace Engineering **22**, 260 (2009).

[44] European Union Aviation Safety Agency (EASA), *Certification Specifications for Engines CS-E - AMC E 810 - Compressor and Turbine Blade Failure,* https://www.easa.europa.eu/sites/default/files/dfu/CS-E%20Amdt%201.pdf (2007), Retrieved on October 25^{th} 2019.

[45] Federal Aviation Administration (FAA), *Code of Federal Regulations - § 33.94 Blade Containment and Rotor Unbalance Tests.* https://www.govinfo.gov/app/details/CFR-2002-title14-vol1/CFR-2002-title14-vol1-sec33-94/summary (2002), Retrieved on October 25^{th} 2019.

[46] Flight Safety Foundation, *In-flight Separation of Propeller Blade Results in Uncontrolled Descent and Fatal Accident to Twin-turboprop Commuter Aircraft.* https://flightsafety.org/ap/ap_feb97.pdf (1997), .

[47] Aviation Safety Network, Flight Safety Foundation, *Engine problem* , https://aviation-safety.net/database/record.php?id=20131025-0 (2013), Retrieved on October 25^{th} 2019.

[48] S. Bretschneider, F. Rothe, M. G. Rose, and S. Staudacher, *Compressor Casing Preliminary Design Based on Features,* Proceedings of the ASME Turbo Expo **5**, 1 (2008).

[49] I. Armendáriz, J. Olarrea, and J. García-Martínez, *Parametric Analysis of a Highly Dynamical Phenomena Caused by a Propeller Blade Loss,* Engineering Failure Analysis **57**, 528 (2015).

[50] I. Armendáriz, J. López, J. Olarrea, M. Oliver, and H. Climent, *Case Study: Analysis of the Response of an Aircraft Structure Caused by a Propeller Blade Loss,* Engineering Failure Analysis **37**, 12 (2014).

[51] I. Armendáriz, J. Olarrea, and J. García-Martínez, *Engine to Wing Structural Design Under Critical Loads Caused by a Propeller Blade Loss,* Engineering Structures **158**, 155 (2018).

[52] D. Howe, *Aircraft Loading and Structural Layout* (Professional Engineering Publishing, UK, London, 2004).

[53] Dr. S. Shroff, *Linear Modelling (incl.FEM),* (Lecture) Notes (Delft University of technology, 2017) contributions and edits by: Wim Westbroek and Peixuan Zhou.

[54] T. Nicholas, *Critical issues in high cycle fatigue,* International Journal of Fatigue **21**, 221 (1999).

[55] Unified Teaching Staff of Massachusetts Institute of Technology, *Area and Bending Inertia of Airfoil Sections,* https://ocw.mit.edu/courses/aeronautics-and-astronautics/16-01-unified-engineering-i-ii-iii-iv-fall-2005-spring-2006/systems-labs-06/spl10b.pdf (2006), retrieved on June 26^{th} 2020.

[56] M. Drela and H. Youngren, *XROTOR,* http://web.mit.edu/drela/Public/web/xrotor/ (2009).

[57] H. Youngren, M. Drela and S.Sanders, *Ducted Fan Design Code (DFDC),* http://web.mit.edu/drela/Public/web/dfdc/ (2007).

[58] D. H. Wood, V. L. Okulov, and D. Bhattacharjee, *Direct calculation of wind turbine tip loss,* Renewable Energy **95**, 269 (2016).

[59] T. WAN and H. SARAVIA, *Aerodynamic Calculation of an Elliptic Ring Wing,* (1991), 10.2514/6.1991-68.

[60] Beth Ashby, *A fierce little beast!* https://www.modelflying.co.uk/news/article/a-fierce-little-beast/25296/.

[61] Unknown, *CFD,* http://www.melmoth2.com/texts/CFD.htm.

[62] M. H. Sadraey, *Aircraft Design : A Systems Engineering Approach* (John Wiley & Sons, 2012).

[63] J. D. Anderson, *Fundamentals of aerodynamics.* (Mc Graw Hill, University of Maryland, 1984).

[64] M. Drela and H. Youngren, *Athena Vortex Lattice (AVL) v3.36,* http://web.mit.edu/drela/Public/web/avl/ (2017).

[65] Unknown, *ATR72 Flight Crew Operating Manual,* http://www.737ng.co.uk/atr72fcom.pdf (1999), student version used.

[66] ASSAULT SYSTÈMES, *ABAQUS,* https://www.3ds.com/products-services/simulia/products/abaqus/ (2020), student version used.

[67] European Union Aviation Safety Agency, *Certification Specifications and Acceptable Means of Compliance for Large Aeroplanes CS-25*, Regulations Annex I to ED Decision 2019/013/R Amendment (EASA, 2019).